Doctoral Thesis

Determination of Rotational Structures with High-Resolution Mass-CRASY

Jong Chan Lee

Department of Chemistry

Ulsan National Institute of Science and Technology

2021

Determination of Rotational Structures with High-Resolution Mass-CRASY

Jong Chan Lee

Department of Chemistry

Ulsan National Institute of Science and Technology

Determination of Rotational Structures with High-Resolution Mass-CRASY

A thesis/dissertation submitted to
Ulsan National Institute of Science and Technology
in partial fulfillment of the
requirements for the degree of
Doctor of Philosophy

Jong Chan Lee

1/6/2021

Approved by

_____

Advisor
Thomas Schultz

Determination of Rotational Structures with High-Resolution Mass-CRASY

Jong Chan Lee

This certifies that the thesis/dissertation of Jong Chan Lee is approved.

1/6/2021

signature

_____

Thomas Schultz

signature

_____

Oh Hoon Kwon

signature

_____

Yung Sam Kim

signature

_____

Bum Suk Zhao

signature

_____

Chang Min Choi

ABSTRACT

Analysis of rotational spectra provides information about molecular structure and the rotational spectrum can also be used as a molecular fingerprint for molecule identification. Microwave spectroscopy is currently the most powerful tool to measure rotational spectra. High-resolution microwave spectroscopy can reach single kHz resolution and can get single Hz accuracy. Rotational Raman spectroscopy is a complementary method to microwave spectroscopy with different selection rules. But past Raman spectroscopy had a limited resolution, reaching only 100's of MHz resolution.

High-resolution mass-CRASY breaks this limitation with a new method for high-resolution measurements. Time-domain measurements produce high-resolution mass-correlated rotational Raman spectra, and we obtained a resolution below 1 MHz resolution and kHz accuracy. In addition to high-resolution spectra, our technique produces correlated spectroscopic data. With mass-correlated information, we can assign signals for multiple molecules in an impure sample without purification. Here, we use this capability to resolve isotopologue spectra from naturally heterogeneous samples.

Our technique is still a new spectroscopic tool, so we need to prove its reliability. In this thesis, I describe the characterization of numerous molecules which J characterized with high-resolution mass-CRASY during my thesis. The measured molecules are linear, symmetric tops, and asymmetric tops all of which are Raman active. I prove the reliability and accuracy of CRASY by comparison to literature data, where available. The development and application of this new high-resolution technique allowed to obtain precise spectroscopic information for a large range of molecules.

Key Word: Rotational spectroscopy, Mass spectrometry, Correlated spectroscopy, High-resolution spectroscopy, Molecular alignment

Contents

List of Figures

Chapter I

Chapter II

Chapter III

Chapter IV

Chapter V

List of Tables

Chapter I

Chapter III

Chapter IV

Chapter V

Supporting Information

Table S1. Assigned lines for the benzene-d6 and PGOHPER fit results with 200 ns sparse scan.

Table S2. Assigned lines for the pyridine and PGOHPER fit results with 20 ns continuous scan.

Table S3. Assigned lines for the pyridine and PGOHPER fit results with 100 ns sparse scan.

Table S4. Assigned lines for the pyridine and PGOHPER fit results with 500 ns sparse scan.

Table S5. Assigned lines for the most dominant fragmentation (53 u) of pyrazine and PGOHPER fit results with 100 ns sparse scan.

Table S6. Assigned lines for the main isotopologue (80 u) of pyrazine and PGOHPER fit results with 100 ns sparse scan.

Table S7. Assigned lines for the main isotopologue of furan and PGOHPER fit results with 100 ns sparse scan.

Table S8. Assigned lines for the main isotopologue of thiophene and PGOHPER fit results with 100 ns sparse scan.

Table S9. Assigned lines for the main isotopologue of butadiene and PGOHPER fit results with 100 ns sparse scan.

Chapter I. Introduction

1.1 Correlated Rotational Alignment Spectroscopy

Most recent advances in spectroscopy were driven by the development of new laser techniques. The chirped pulse amplification (CPA) technique allows the amplification of short laser pulses to very high intensities while preventing the damage of optics (see Figure 1.1). CPA was developed by Donna Strickland and Gerard Mourou in 1980 and for this work, they received the Nobel Prize in Physics in 2018.[1]

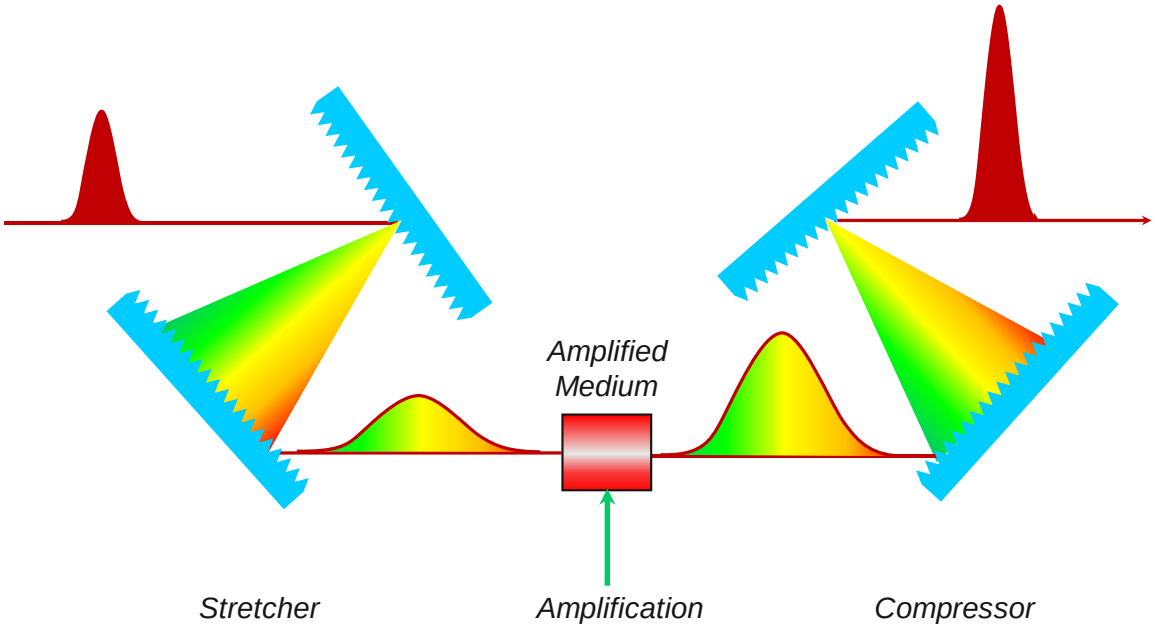

Figure 1.1 The chirped Pulse Amplification (CPA) scheme is based on three steps. (1) Stretcher: A pair of gratings disperse the laser pulse and the pulse is temporally stretched, which reduces the peak power. (2) Amplification: An amplifier medium (i.e. Ti: Sapphire) amplifies the stretched laser pulse. (3) Compressor: A grating pair with opposite dispersion of the stretcher compresses the pulse. Using optical dispersion, CPA helps to generate high-intensity laser pulses without damaging the amplifier medium or other optics.

The development of CPA provided the basis for the generation of ultrashort laser pulses. The short pulses facilitated time-domain spectroscopy with picosecond and femtosecond time resolution, also called femtochemistry. A.H. Zewail is one pioneer of femtochemistry and he was awarded the Nobel Prize in Chemistry in 1999.[2] The femtosecond pulse width made it possible to monitor molecular dynamics in real-time and helped observe many types of physical and chemical dynamics. Based on the

experimental tools of femtochemistry, many spectroscopists now perform research to unravel time-dependent molecular properties.

The investigation of molecular structure is important because the molecular structure is correlated with all other molecular properties. There are many established ways to determine the structure of a molecule A method of particular relevance for this thesis is the analysis of rotational spectra. Such spectra are commonly obtained by Fourier transform microwave spectroscopy (FTMW) or high-resolution IR spectroscopy.[3] Our group recently developed another tool for high-resolution mass-correlated rotational Raman spectroscopy[4], which can resolve accurate rotational Raman spectra for multiple isotopologues with a single measurement. This method is currently a unique analysis tool in the world. In this thesis, I describe 8 different molecules for which I measured high-resolution rotational Raman spectra and for which I could analyze rotational structure.

Correlated Rotational Alignment Spectroscopy (CRASY) is a novel type of spectroscopy to investigate several molecular properties in a single experiment. Since 2011, CRASY was developed by Schröter et al.[5] and characterized the rotational spectrum of CS_2. Figure 1.2 shows a two-dimensional spectrum of

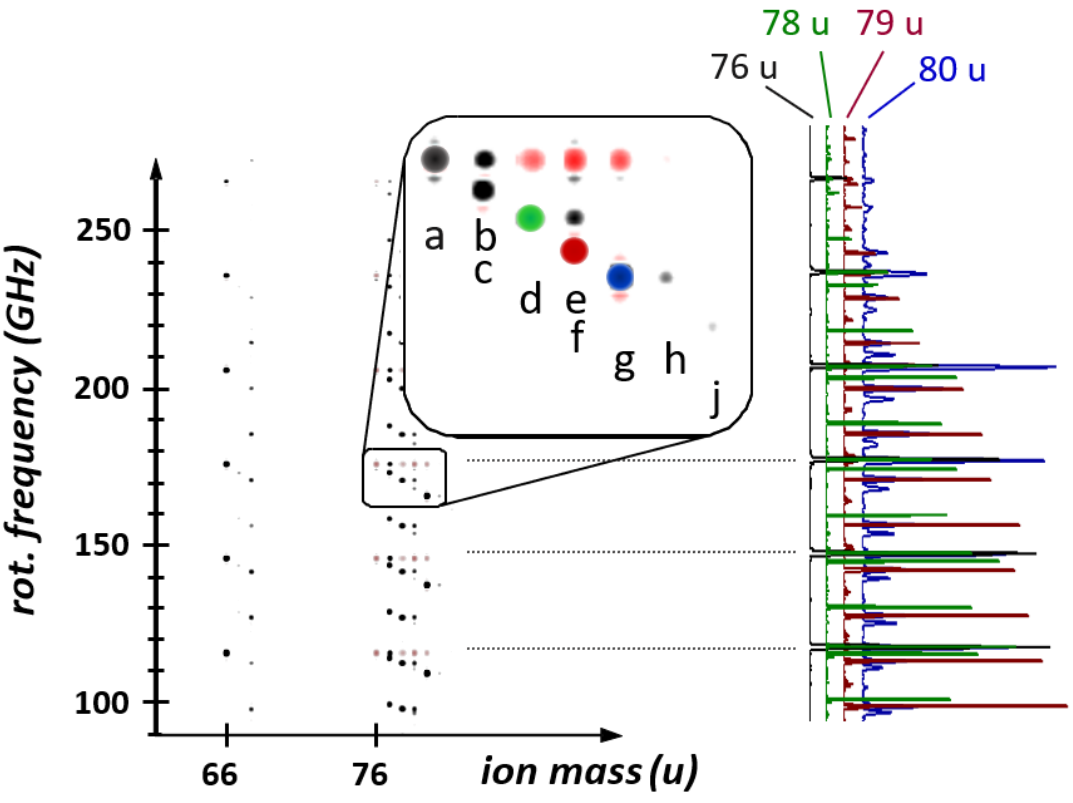

Figure 1.2. Mass-CRASY result for CS_2 and isotopologues. Illustration of the 2-dimensional correlation of rotational frequency and mass. The central inset highlights isotopologue-specific signals (J = 12-14 transition, rare isotopes in bold): (a) $^{32}S^{12}C^{32}S$, (b) $^{32}S^{13}C^{32}S$, (c) $^{32}S^{12}C^{33}S$, (d) $^{32}S^{12}C^{34}S$, (e) $^{32}S^{13}C^{34}S$, (f) $^{33}S^{12}C^{34}S$, (g) $^{34}S^{12}C^{34}S$, (h) $^{34}S^{13}C^{34}S$, (j) $^{34}S^{12}C^{36}S$.

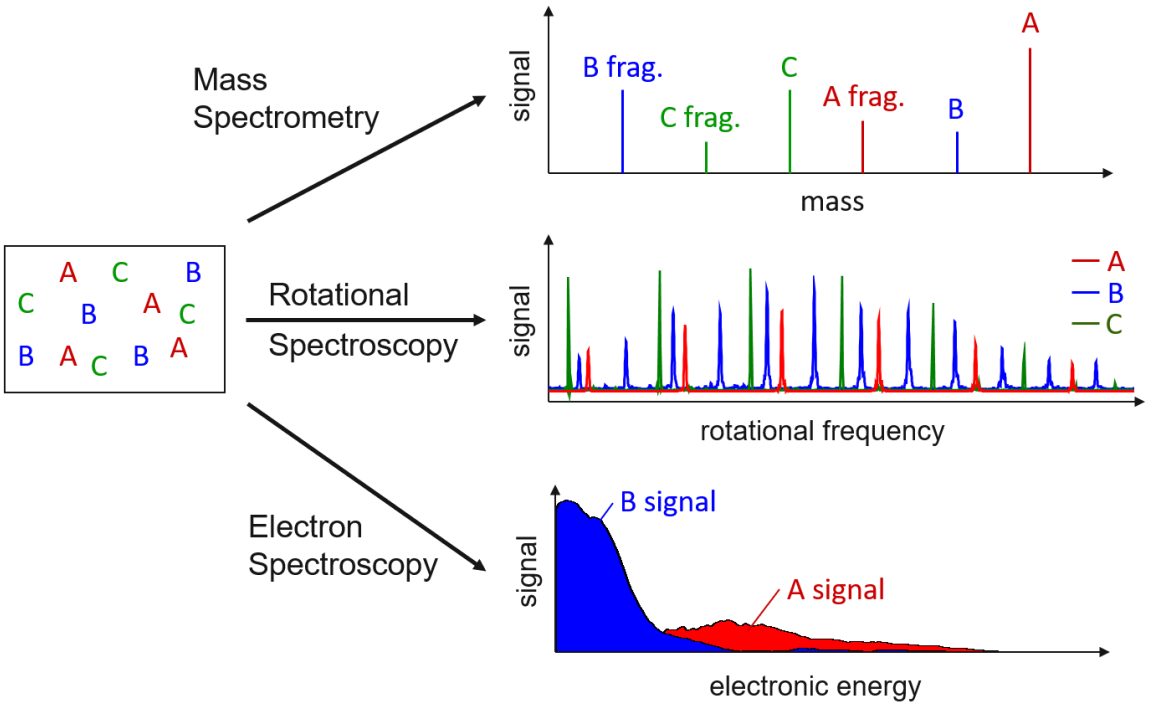

Figure 1.3. Multidimensional CRASY: rotational, mass, and electron spectra. The mass spectrum distinguishes molecular composition. The rotational spectrum resolves the structure of each molecule. The electron spectrum investigates the electron energy of the molecule. For a heterogeneous sample, this multidimensional data can classify multiple molecular properties with a single measurement.

CS_2 isotopologues. The correlated spectrum produced rotational spectra separated by mass. It characterized the rotational spectrum of multiple different isotopologues with a single measurement. Traditional spectroscopic measurements interrogate a single molecular property. CRASY breaks this conventional wisdom; the CRASY technique can correlate multiple pieces of spectroscopic information with a single measurement. CRASY's multidimensional data set can be used to disentangle molecular properties for multiple species in a heterogeneous sample.

The current implementation of CRASY can combine 4 types of spectroscopy: mass spectrometry, rotational spectroscopy, pump-probe spectroscopy, and photoelectron spectroscopy. The rotational spectrum gives us structure information and the mass spectrum can analyze the composition of the molecules. The correlated mass-rotation data shows rotational spectra for each mass channel and further, can resolve multiple spectra in the same mass channel. Ideally, mass-CRASY can identify and characterize all molecules in a molecular beam. The combined information of structure, mass, and other molecular properties allows to separate signals from different components in a heterogeneous sample, even if those components cannot be identified by a single spectroscopic property.

The CRASY measurements presented in this thesis only correlate mass spectra and rotational spectra,

but greatly expanded the number and type of investigated molecules. Future experiments aim to correlate further observables. Figure 1.3. illustrates the advantage of correlating mass, rotational and electron spectra. With electron-CRASY, we can correlate the electronic structure for each molecule to the corresponding mass and rotational spectrum. Pump-probe-CRASY can probe photochemical dynamics, which can be correlated with the rotational structure. Future measurements will add electron spectroscopy and pump probe dynamics to analyze 4 types of correlated measurements and investigate additional kinds of molecular properties (see Table 1.1).

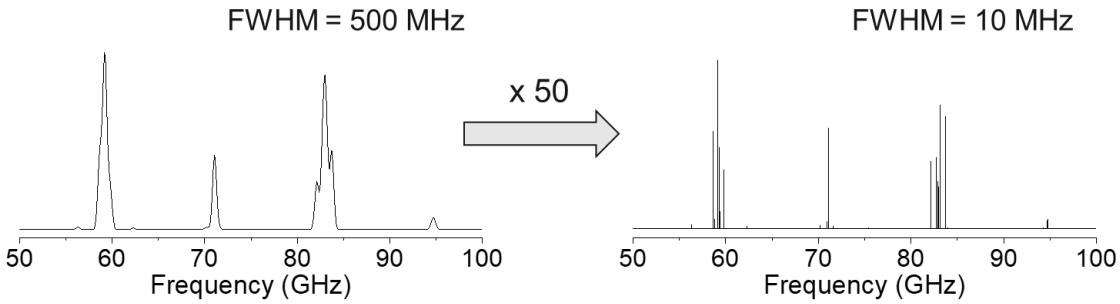

Figure 1.4. Comparison of rotational spectra for pyridine with 500 MHz and 10 MHz full-width-at-half-maximum resolution. In a 500 MHz spectrum, the peaks are broader and include several rotational states. The 10 MHz spectrum identifies each line and this contributes to the accurate rotational structure analysis of molecules.

Before attempting to collect such highly correlated data, we needed to improve the resolution for investigating complex rotational spectra. Figure 1.4 shows that the better resolution can reveal more rotational lines. I worked on establishing CRASY as a new high-resolution technique to get more precise structural information. The resolution of previous CRASY data was only 500 MHz, based on a 2 ns opto-mechanical delay stage. With our new high-resolution technique, we can reach a resolution below 1 MHz. This represents the highest resolution ever obtained in rotational Raman spectroscopy.[7] High-resolution CRASY provides broad-band, high resolution and absolute-frequency spectra and allows to determine highly accurate rotational constants.[8]

In this thesis, I present high-resolution rotational Raman spectra, obtained through mass-CRASY experiments. I describe the principle of CRASY and how we can obtain high-resolution data in detail. The new high-resolution technique can reveal complicated rotational spectra and determine more accurate rotational constants than any preceding type of rotational-Ramana spectroscopy.

Table 1.1. The character of typical spectroscopic tools. CRASY can collect all these types of information in a single measurement.

Type of Spectroscopy	*Investigated Property*	*Used to Learn About*
Mass spectrometry	Composition	Sample composition
Rotational spectroscopy	Nuclear structure	Structure determination
Electronic spectroscopy	Electronic structure	Electronic properties
Pump-probe spectroscopy	Reaction dynamics	Photochemistry
CRASY	All of the above	All of the above

1.2 References

1.Strickland, D.; Mourou, G., Compression of amplified chirped optical pulses. *Optics communications* **1985,** 56 (3), 219-221.

2. Zewail, A. H. Femtochemistry: Atomic-scale dynamics of the chemical bond using ultrafast lasers (Nobel Lecture). *Angewandte Chemie International Edition* **2000,** 39 (15), 2586-2631.

3. Weber, A. In Handbook of High-resolution Spectroscopy; Quack, M., Merkt, F., Eds.; John Wiley & Sons, Ltd: Chichester, UK, **2011**; Vol. 2; Chapter High-resolution Raman Spectroscopy of Gases, pp. 1153

4. Schröter, C.; Lee, J. C.; Schultz, T., Mass-correlated rotational Raman spectra with high resolution, broad bandwidth, and absolute frequency accuracy. *Proceedings of the National Academy of Sciences* **2018,** *115* (20), 5072-5076.

5. Schröter, C.; Kosma, K.; Schultz, T., CRASY: Mass- or Electron-Correlated Rotational Alignment Spectroscopy. *Science* **2011,** *333* (6045), 1011-1015.

6. Schröter, C.; Choi, C. M.; Schultz, T., CRASY: Correlated Rotational Alignment Spectroscopy Reveals Atomic Scrambling in Ionic States of Butadiene. *Journal of Physical Chemistry A* **2015,** *119* (8), 1309-1314.

7. Lee, J. C.; Lee, D. E.; Schultz, T., High-resolution rotational Raman spectroscopy of benzene. *Physical Chemistry Chemical Physics* **2019,** *21* (6), 2857-2860.

8.Özer, B. R.; Heo, I.; Lee, J. C.; Schröter, C.; Schultz, T., De novo structure determination of butadiene by isotope-resolved rotational Raman spectroscopy. *Physical Chemistry Chemical Physics* **2020,** *22* (16), 8933-8939.

Chapter II. Experiment

2.1 Experimental Background

Mass-CRASY measures mass-correlated rotational Raman spectra. Time of flight (TOF) mass spectrometry distinguishes molecular species in a sample according to their ion's mass to charge ratio. Rotational spectroscopy provides structural information of molecules through the molecular moments of inertia and it delivers a 'fingerprint' that can be used to identify molecules. CRASY is based on rotational Raman spectroscopy. Figure 2.1 illustrates the energy levels and rotational Raman transitions for a linear molecule. Raman spectroscopy only works for Raman active molecules which are anisotropically polarizable. This includes almost all molecules in the world. To correlate rotational and

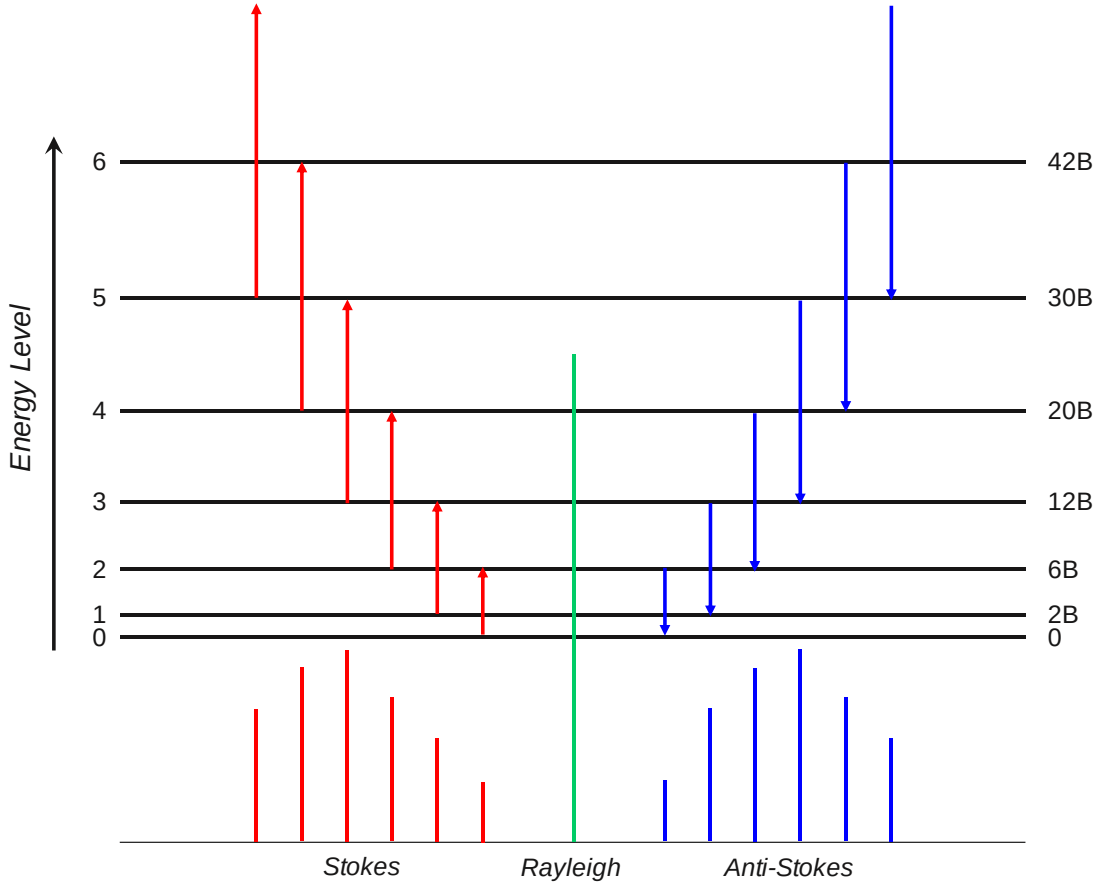

Figure 2.1. Rotational Raman spectroscopy energy level diagram for a linear molecule. Stokes scattering is observed when the final state is higher than the initial state (red lines) and Stokes lines appear at a longer wavelength as compared to the incident light. In Rayleigh scattering, there is no change between the initial state and final state (green line). In anti-Stokes scattering, the final state is lower than the initial state (blue lines) and anti-Stokes lines appear at a shorter wavelength.

mass spectroscopy, we observe rotational coherence, also known as nonadiabatic molecular alignment.[1] When a molecule is exposed to an electric field, the molecule is oriented or aligned by the anisotropic interaction between the field and the molecule. Nonadiabatic alignment can be observed after the electric field is turned off. We use a short intense laser pulse (femtoseconds or a few picoseconds) to create non-adiabatic alignment. The aligned state then evolves as a coherent superposition of rotational eigenstates. The analysis of the frequency components in this rotational wavepacket reveals the rotational structure of molecules.

Time-resolved mass spectrometry[2] is required to connect rotational Raman spectroscopy and mass spectrometry by nonadiabatic alignment. Time-resolved mass spectrometry allows us to measure the variation of ion signals inside the mass spectrometer, as a function of the time delay between two laser pulses. As illustrated in Figure 2.2, an alignment pulse generates a rotational wave packet via non-adiabatic alignment. This occurs because the alignment laser pulse excites molecules via a Raman process from the ground state into rotationally excited states. An ionization laser pulse ionizes the

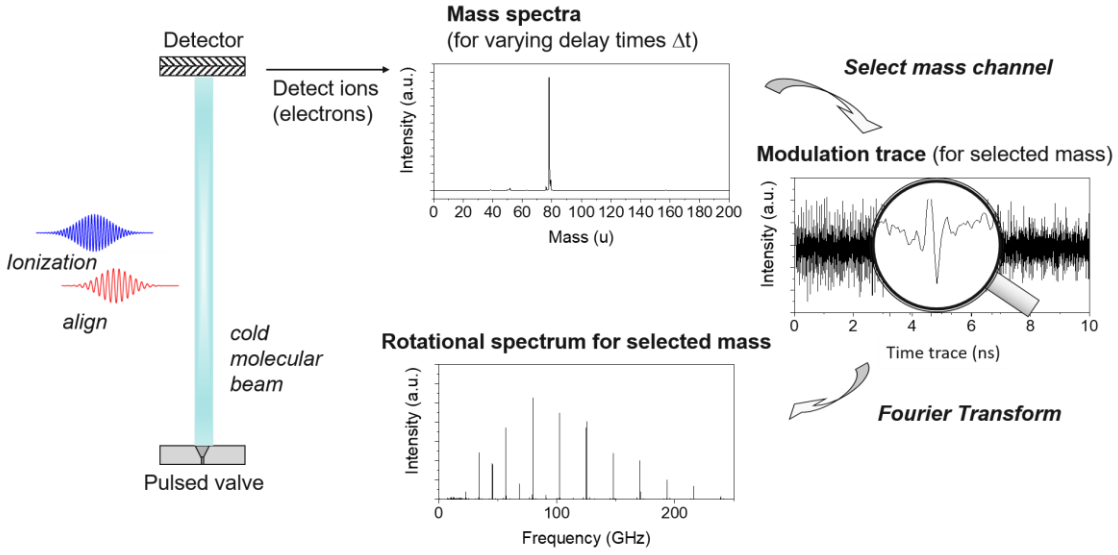

Figure 2.2. CRASY measurement process. The alignment pulse excites rotational coherence in molecules. The ionization pulse ionizes the molecules that have a transition dipole parallel to the polarization of the light field. The ionized molecules are detected by a mass spectrometer. The signal amplitude in a selected mass signal can be plotted in a modulation trace, as function of the alignment-ionization delay. Fourier transformation of the modulation trace generates a rotational Raman spectrum.

molecules, and the ions are detected in the mass spectrometer. The ionization probability depends on the molecular alignment and is modulated with the rotational transition frequencies excited by the alignment pulse. CRASY monitors the modulation of the signal intensity as function of the time delay

between the alignment pulse and the excitation-ionization pulses. In the experiments discussed in this thesis, the excitation and ionization are driven by a single ultraviolet pulse.

A cold molecular beam is needed to observe the rotational revivals in the aligned molecular ensemble. Molecular beams provide a collision-free environment with a long coherence time for the rotational wavepacket. The cold environment also reduces the number of quantum states that must be resolved. In our experiment, an Even-Lavie pulsed valve generated a cold molecular beam with a temperature below 10 K. We estimated this beam temperature with a comparison between the measured and simulated.

2.2 Principle of CRASY

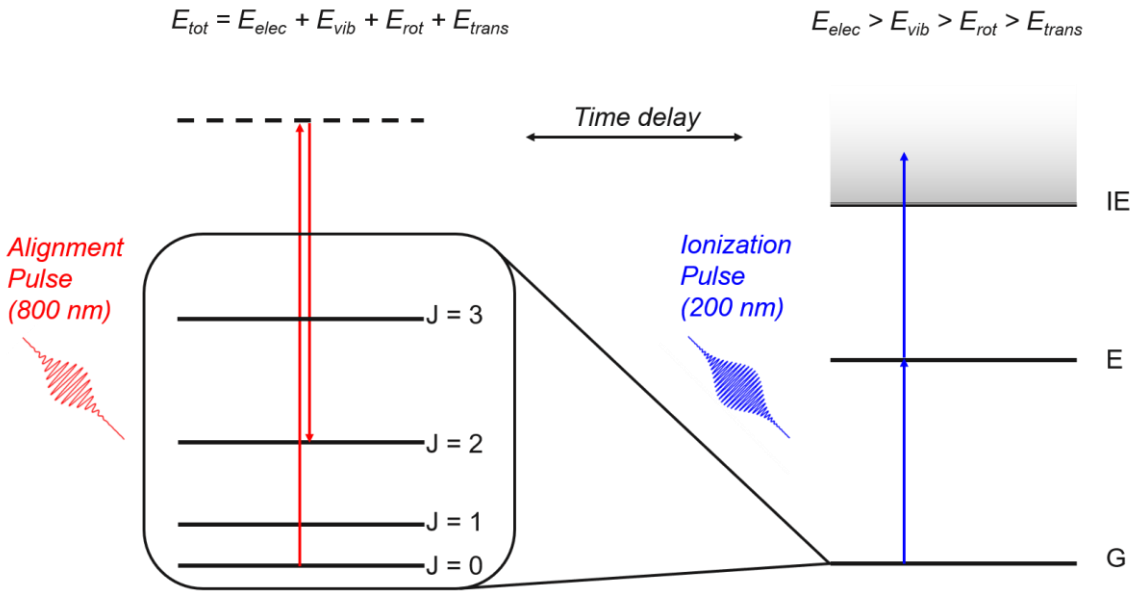

Figure 2.3. Energy diagram for CRASY experiments. Left: Alignment pulses excite molecules via a virtual state into a different rotational state (Raman excitation). The arrows depict a Stokes shift with a higher, final J state than the initial J state. Right: An ionization pulse ionizes the molecules and captures the rotational dynamics at different time delays after the alignment process. Note that the alignment process only affects the rotational energy level of the molecule.

CRASY follows the typical method for time-resolved mass spectrometry but exploits nonadiabatic alignment phenomena.[1,2] Freely rotating molecules in a molecular beam are aligned when exposed to a linearly polarized alignment laser pulse. (Usually, a picosecond pulse is used to avoid high-order processes that might be driven by an intense femtoseconds pulse.) Molecules are affected in their rotational motion through their anisotropy of polarizability. As illustrated in Figure. 2.3, this first alignment step corresponds to a rotational Raman excitation. After the pulse, the molecules rotate coherently with new angular momentum. For tracking the molecular rotation, CRASY ionizes

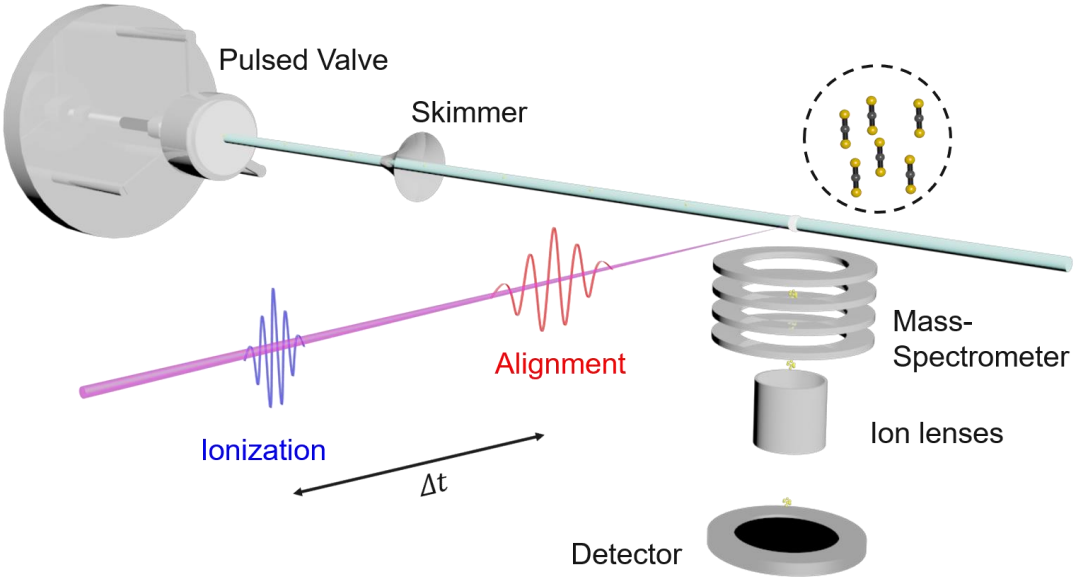

Figure 2.4. The experimental scheme of the CRASY experiment. The pulsed valve creates a molecular beam with a supersonic expansion and gives us under 10 K beam temperature. The molecular beam passes through the skimmer and the skimmer collimates the beam. The ensemble in the molecular beam is exposed to the alignment pulse and the ionization pulse ionizes the molecules with a controlled time delay. The ionized molecules are accelerated in a time-of-flight mass spectrometer and fly to a microchannel plate detector.

molecules with another linearly polarized laser pulse ("ionization pulse" in Figure 2.3). The coherent rotational motion is scanned by varying the time delay between the alignment pulse and ionization pulse.[3] The ionization signal intensity is modulated with the time delay due to the coherent rotation of the molecules. This modulation of the signal is detected in TOF mass spectra.[4]

The time-dependent trace for each ion mass reveals the revival signals for the rotating ground state molecules. Depending on the structural complexity of the molecule, the rotational transition energies may be evenly spaced, leading to a clear revival signal, or the transition energies may be unevenly spaced and a clear rotational revival signal may not be observed. But Fourier transformation of the time dependent trace will nevertheless reveal all frequency components for the rotational transitions excited by the alignment pulse and a rotational spectrum is produced for every mass channel.

2.3 Experiment Apparatus

The environmental condition of the laboratory was controlled to offer a stable temperature (20 ± 0.5 °C) and humidity (45 ± 10 %). The regular failure of this climate control system seriously affected the available measurement time and occasionally led to the need for a complete restoration of laser alignment, beamline alignment and experimental set-up. The oscillator of our laser system is a Coherent Vitara-T with 800 nm output at 80 MHz repetition rate. Two regenerative amplifiers (Coherent, Libra USP-1K-HE-200, 1 kHz repetition rate) share the same oscillator. The two amplifiers are synchronized by two SDG Elite delay generators and one SRS DG535 delay generator. The oscillator repetition rate is referenced against a GPS clock (Leo Bodnar, Precision GPS Reference clock (GPSDO)) using a frequency counter (AIM-TTI-INSTRUMENTS, TF930). The output of the amplifiers is ~1.8 W (Ionization line) and ~2.1 W (Alignment line). The alignment beam is split and attenuated by an optical attenuator to typical values of 100-300 mW. In the ionization beam line, we split off several beam lines for UV generation. The 200 nm beam, generated by fourth harmonic generation, yields about 1 μJ pulses and the 266 nm beam yields about 5-10 μJ after third harmonic generation. The alignment beam line passes through an opto-mechanical delay stage (Physik Instrumente, MD-531, 306 mm range). 16 mirrors fold the beamline across the stage to achieve a total range of 4.8 m, corresponding to 16 ns time delay. Delay stage encoder positions were calibrated against a temperature-insensitive optical encoder (Sony Laserscale BL57-RE, thermal expansion coefficient of $0.7 \cdot 10^{-6}$ m/(m·K)). A concave mirror (f = 37.5 cm) is positioned in front of the spectrometer window to focus the laser light onto the molecular beam.

CRASY is a type of gas phase spectroscopy and we perform the measurements in high vacuum chambers. The vacuum chambers are evacuated by three turbo pumps (two Pfeiffer TMH 1601 P, and one Pfeiffer TPU 240) and one rough vacuum pump (initially an Edward scroll pump, XDS35i, later a Kashiyama Neo dry 30E). Our vacuum system is divided into two regions. the source region and the spectrometer region. As shown in Figure 2.4, a pulsed valve (Even-Lavie pulsed valve, E.L.-7-4-2007-HRR) is attached to the source region and a skimmer separates the two regions. When the valve generates a molecular beam, the pressure of the source region increases up to $3 \cdot 10^{-5}$ mbar and the spectrometer part remains close to 10^{-7} mbar. The TOF mass-spectrometer is mounted perpendicular to the molecular beam. It includes a typical Wiley-McLaren time-of-flight (TOF) mass spectrometer[3] of approximately 1 m length. Ions are accelerated with a 700 V repeller voltage and an ion lens focuses the ions onto the detector, with an optimized voltage of +320 V. A microchannel plate (MCP) detector (2 plates in chevron geometry, initially a Tectra MCP in a home-built mount, later a pre-assembled Hamamatsu F4655-10 detector) is operated with ~2.2 kV. To synchronize pulsed valve, pulsed ion extraction and other elements of the measurement process, a diode detects stray light from the laser pulse of the ionization beamline. The diode connects to a delay box that distributes TTL signals to other

devices. The experiment operates at 500 Hz, which is half of the laser amplifier repetition rate. We usually collect the signal for 1,000 laser shots to generate a single mass spectrum.

2.4 Improvement of the Rotational Resolution

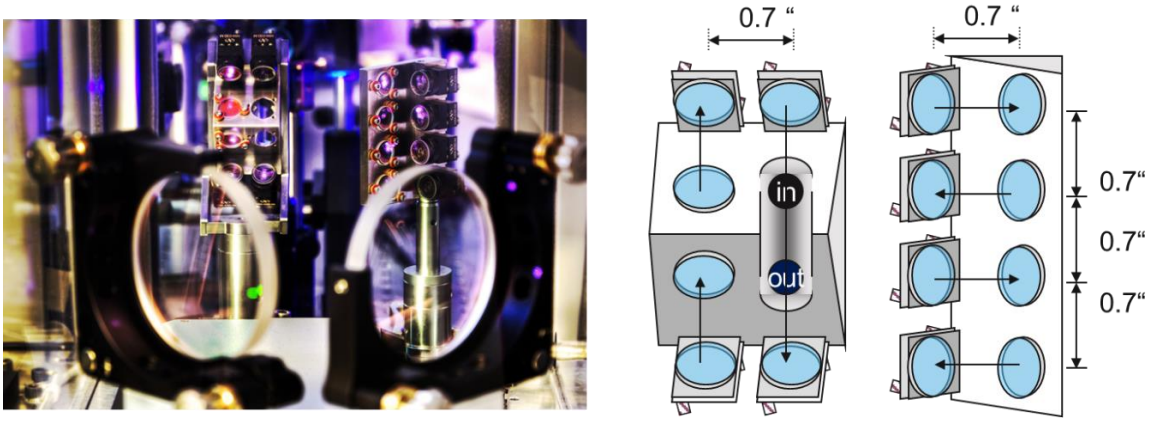

Figure 2.5. Inexpensive 16-fold extension of the opto-mechanical time delay range by folding of the beam path. Opposing half-inch mirrors reflect the beam across two three-inch optics, mounted on a mechanical delay stage with 0.3 m range.

CRASY generates rotational spectra through a type of Fourier transform spectroscopy. The spectroscopic resolution is proportional to the range of the time delays between the alignment and ionization pulse. The straightforward way to increase this range is to use a longer delay stage. But a normal lab space doesn’t allow to significantly increase this mechanical stage. Our group solved this problem by combining two types of delay, one mechanical and one electronic, to obtain an infinite interferometer.

2.4.1 Extended Delay Interferometer

Our laser system consists of an 80 MHz oscillator and two 1 kHz regenerative amplifiers. Those two amplifiers share the single oscillator and both are synchronized with electronic timing units. One of the amplifiers generates the alignment pulses that generate nonadiabatic alignment. This laser pulse passes through an optomechanical translation stage. The other amplifier delivers the probe pulses to ionize the molecules.

To control the time delay from single fs to 16 ns, we employ typical pump-probe methods with a mechanical stage. As shown in Figure 2.5, the alignment laser pulse enters this stage and is reflected 16 times across the 30 cm translation stage. Consequently, this stage offers a 4.8 m path, corresponding to a maximum 16 ns time delay.

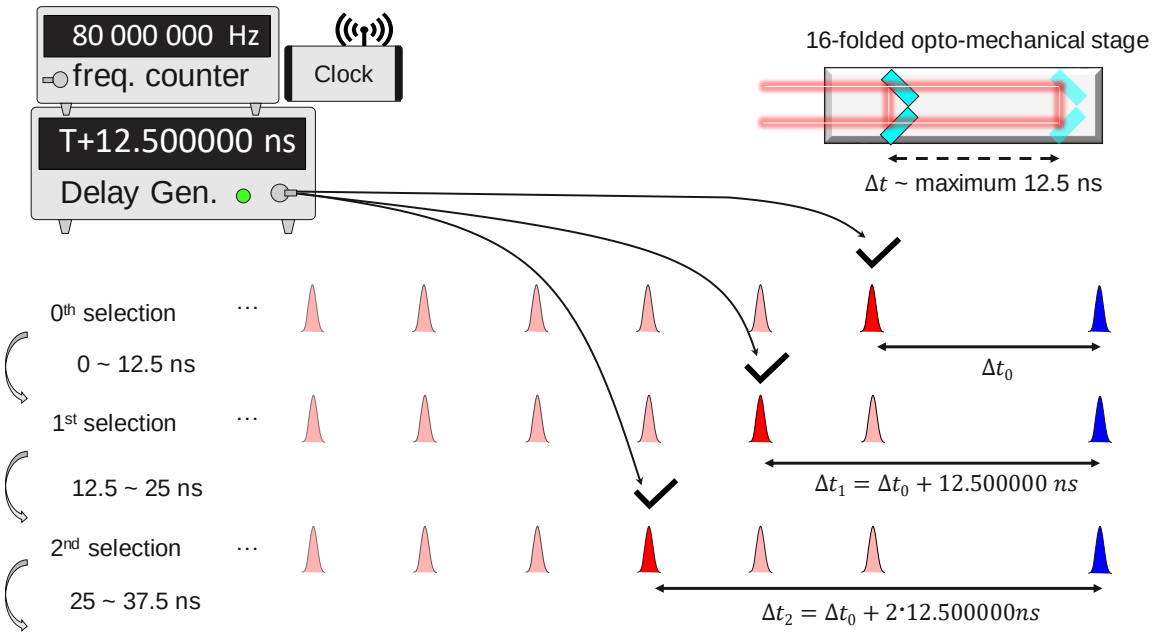

Figure 2.6. Scheme of the pulse selection technique based on two amplifiers with one shared oscillator. An electronic delay generator is connected between the amplifiers and this makes it possible to pick oscillator pulses for each amplifier. Our laser oscillator frequency is close to 80 MHz and the pulse repetition rate is 12.5 ns. A computer, which is connected to the delay generator, selects a pulse from the 12.5 ns pulse train. To reduce timing uncertainty, we check the real oscillator frequency which can drift due to environmental changes. This is done with a frequency counter which is synchronized with a GPS clock and measures the oscillator frequency with an accuracy of $\nu/\Delta\nu = 10^{10}$.

The oscillator generates pulses with 80 MHz repetition rate and the time between each pulse pair is 12.5 ns. This pulse is split into the two amplifiers to generate the alignment pulse and ionization pulse. The alignment amplifier picks one oscillator pulse every millisecond to amplify pulses with 1 kHz repetition rate. A Stanford Research Systems delay generator (SRS-DG535) controls the timing of the pulse amplified by the ionization pulse amplifier as depicted in Figure 2.6. By adding a 12.5 ns delay to the SRS-DG 535 timing, the ionization amplifier is forced to amplify a subsequent pulse, adding a precise 12.500000 ns delay:

$$\frac{1}{\text{Oscillator Frequency}} = \text{Pulse Repetition Rate} = 12.5 \text{ ns}$$

$$\Delta t' = \Delta t + 12.5 \cdot n \qquad \therefore n\text{: the number of pulse jumps}$$

However, the spectroscopic accuracy depends on a reliable calibration of these time delays. In the frequency domain, frequency comb spectroscopy locks an oscillator frequency to an atomic clock and this produces highly accurate frequencies.[5,6] Frequency comb spectroscopy had a significant impact in

the fields of atomic spectroscopy, molecular spectroscopy and metrology.[7]

We developed a time-domain equivalent to frequency comb spectroscopy using a relatively cheap external clock. Our timing errors are caused by the timing uncertainty of the oscillator pulses. The exact value of the oscillator repetition rate may drift around 80 MHz and the values slightly vary with the environmental conditions. This means that the time between two pulses is not exactly 12.5 ns. To correct this error source, a frequency counter records the oscillator repetition rate during the measurement against a GPS-stabilized clock with high accuracy. Drifts in the repetition rate are then easily corrected by adjusting the mechanical delay. Figure 2.7. shows the different results under identical experimental conditions but with or without the reference clock. Without the clock, the pulse-jump delay introduces a discrete error for every 12.5 ns delay increment. This generates a splitting of the spectroscopic lines with a spacing of peak positions by the oscillator repetition rate of 80 MHz. The measurement with the reference clock removes this splitting and locks the measured frequency to the reference clock frequency. Those devices help us to simultaneously increase the resolution and to determine accurate rotational constants.

An analysis of the Allan deviation between our laser oscillator and the GPS reference clock showed that the frequency deviation is $\Delta\nu/\nu << 10^{-8}$ for 1 s frequency measurements and reaches $\Delta\nu/\nu << 10^{-10}$

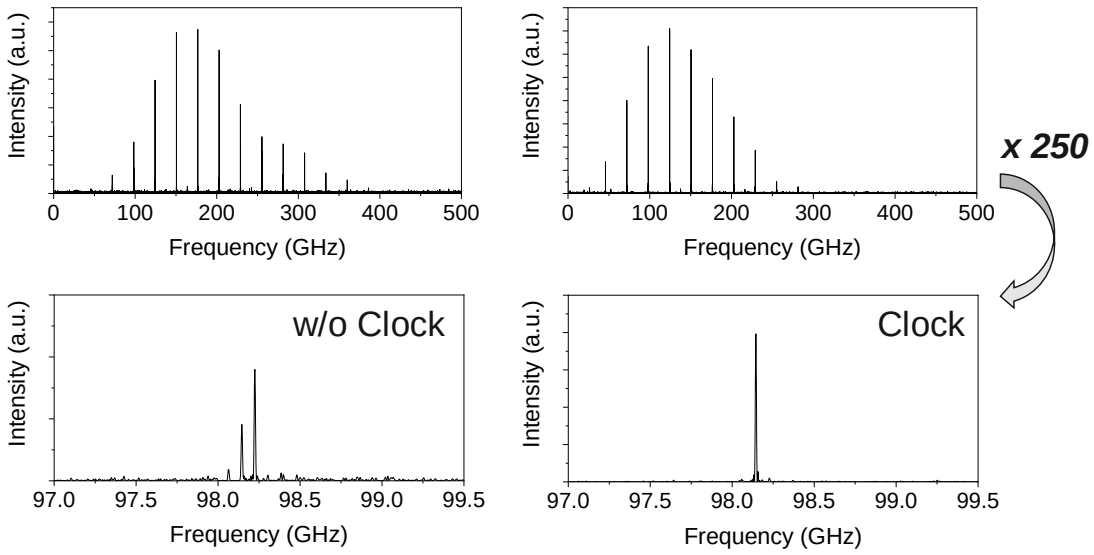

Figure 2.7. The rotational spectrum of CS_2 measured with and without reference clock. Both spectra have the same resolution. Left. The measurement without GPS-clock used the internal clock of the frequency counter with an error in the 10^{-6} range. The mismatch of mechanical and electronic delay calibration created 80 MHz sidebands. Right. With reference clock, the sidebands disappear and all time delays and, after Fourier transformation, spectroscopic frequencies are locked to the reference clock.

for 100 s measurement periods. Environmental variations in temperature, atmospheric pressure or humidity affect our opto-mechanical delay stage and lead to a relative uncertainty of $1 \cdot 10^{-6}$ for our linear delay stage. After the oscillator pulse jump, this uncertainty is reset, as we move to the beginning of the opto-mechanical delay line.

The combination of the extended delay stage and the pulse selection system makes it possible to extend the time delay to arbitrarily large values. For example, when we measure a 50 ns scan, the delay stage moves to measure up to a 12.5 ns delay. Next, the delay stage comes back to its original position and the delay generator adds an additional 12.5 ns with a relative uncertainty of $<< 10^{-8}$. We repeat this process 4 times to obtain a 50 ns scan. With this system, there is no limitation of the measurement time delay. Other experimental factors limit the actual delay range in our experiments and currently this limit is in the regime of few μs.

2.4.2 Sparse Sampling

When we measure longer delays, the measurement time increases proportionally. E.g., a 50 ns scan with 1 ps delay steps and 2 s measurement time for each mass spectrum would require ~28 hours of measurement time. The sparse sampling technique partially solves this problem. Sparse means “thinly distributed, or scattered” and when we use sparse sampling, we measure only a partial sub-set of the complete data set. We use random sparse sampling, i.e., measure spectra with random step size. For example, when we try to sample a 100 ns delay with 1 ps step-size, the measurement data set contains 100,000 mass spectra. But with 20 % sparse sampling, we only measure 20,000 spectra, a small a part of the total data set. The measurement time for a 20 ns continuous scan is the same as for a 100 ns, 20 % sparsely sampled scan. The latter probes 5 times longer delay, so the resolution of the spectrum is 5 times better: the 20 ns scan gives ~50 MHz resolution spectra but a 100 ns scan gives ~10 MHz resolution spectra.

Random sparse sampling is an economical method for data collection because we greatly reduce the measurement time and data quantity. In the field of multidimensional NMR spectroscopy, sparse sampling is already used and was found to degrade the signal-to-noise ratio at acceptable levels.[8,9]

Figure 2.8. compares a continuous scan and a sparse scan, acquired over the same 20 ns range of time delays. Traces in black correspond to a measurement of 20,000 delay points with continuous 1 ps-step size and red traces correspond to a sparse measurement with 10% sparse sampling, covering the same delay range with 2,000 delay points. The sparse measurement can be acquired 10 times faster. Because the total time delay is the same, both measurements produce Fourier transformed spectra with the same resolution, ~50 MHz. As presented later in this thesis, our group measured 1 microsecond scans with only 2 % sampling and obtained a resolution below 1 MHz.[10,11]

One great advantage of Fourier Transform spectroscopy is that discrete noise in the time-domain

becomes evenly distributed upon FT. Periodic noise will lead to localized noise peaks upon FT. Random sampling actually counteracts this effect by decoupling the data time axis from the measurement time axis. Noise of sparse sampling is inversely proportional to $\sqrt{N}$.[12] The decrease in the number of samples increases the signal-to-noise ratio. However, this is only the case when the sampling noise is a dominant factor. Other kinds of noise, e.g., caused by environmental changes, or digitizing noise, remain unaffected.

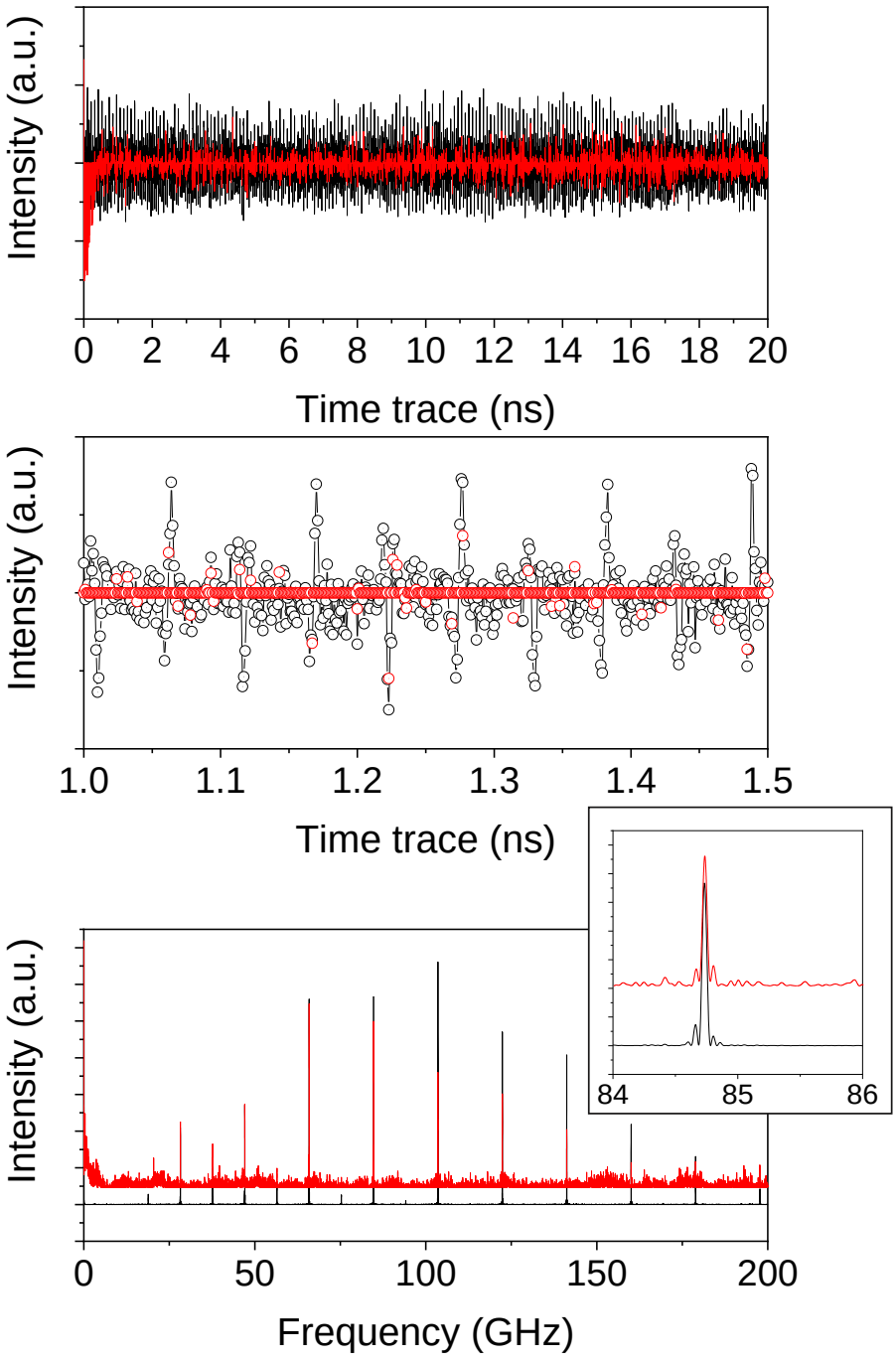

Figure 2.8. Comparison between a continuous scan (black, 20 ns, 1 ps step size, 20,000 data points) and a sparse scan (red, 20 ns, 10% sampling, 2,000 data points). The top trace shows the time-domain experimental data. The middle trace shows an enlarged section of the time domain trace: unsampled data points appear with zero amplitude. The bottom spectra show that both spectra have the same resolution (~50 MHz) but the sparsely sampled spectrum (plotted with a y-axis offset for easier viewing) has a worse signal-to-noise ratio.

2.5 Data Analysis

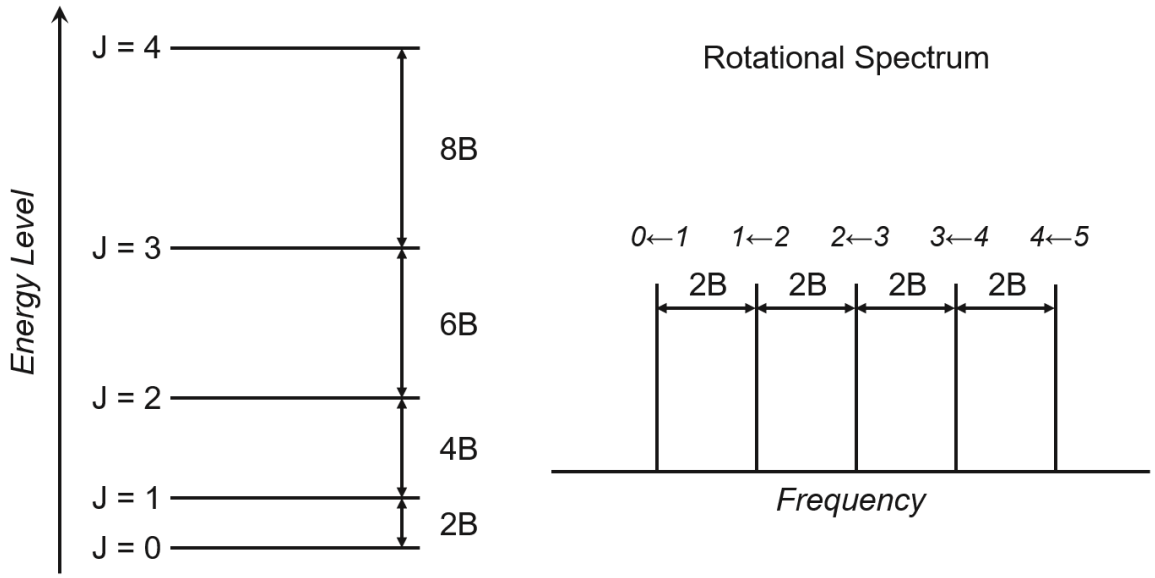

Figure 2.9. Rotational states for a rigid linear rotor and the corresponding rotational spectrum. (Left) The rotational states are quantized with quantum number J and energy differences between states grow quadratically. (Right) The rotational transition frequencies for allowed $J \rightarrow J+1$ transitions are evenly spaced by twice the rotational constant B.

The molecular rotational constants are related to the molecular moments of inertia. To determine rotational constants and distortion constants from experimental spectra, the band positions are fitted to transition frequencies $\Delta F = F_{final} - F_{initial}$. For a linear molecule with rotational constant B, distortion constant D, and rotational quantum number J, the rotational energy levels are $F(J) = B \cdot J(J+1) - D \cdot J^2(J+1)^2$. With this equation, we can readily fit experimentally determined band positions to calculate the rotational constant and distortion constant for a linear molecule.

However, symmetric top molecules and asymmetric top molecules have more complex rotational states than linear molecules. This makes it harder to assign their bands and to fit rotational constants and distortion constants. In this case, we use the PGOPHER program to simulate and fit the rotational spectra.[13] In my thesis, all rotational constants for non-linear molecules are determined with PGOPHER. I greatly appreciate the work of the developers of this program, which allow the free use of PGOPHER for scientific purposes.

2.7 References

1. Stapelfeldt, H.; Seideman, T., Colloquium: Aligning molecules with strong laser pulses. *Reviews of Modern Physics*, **2003,** *75*(2), 543.

2. Zhong, D.; Zewail, A. H., Femtosecond real-time probing of reactions. 23. Studies of temporal, velocity, angular, and state dynamics from transition states to final products by femtosecond-resolved mass spectrometry. *The Journal of Physical Chemistry A* **1998**, *102*(23), 4031-4058.

3. Wiley, W. C.; McLaren, I. H., Time-of-Flight Mass Spectrometer with Improved Resolution. *Review of Scientific Instruments* **1955,** *26* (12), 1150-1157.

4. Schroter, C.; Kosma, K.; Schultz, T., CRASY: Mass- or Electron-Correlated Rotational Alignment Spectroscopy. *Science* **2011,** *333* (6045), 1011-1015.

5. Hänsch, T. W., Nobel Lecture: Passion for precision. *Reviews of Modern Physics*, **2006**, *78*, 1297-1309.

6. Margolis, H. S., Spectroscopic applications of femtosecond optical frequency combs. *Chemical Society Reviews,* **2012***, 41*, 5174-5184.

7. Ahonen, T.; Alanko, S.; Horneman, V. M.; Koivusaari, M.; Paso, R.; Tolonen, A. M.; Anttila, R., A Long Path Cell for the Fourier Spectrometer Bruker IFS 120 HR: Application to the Weak $v_1 + v_2$ and $3v_2$ Bands of Carbon Disulfide. *Journal of Molecular Spectroscopy,* **1997***, 181*, 279-286.

8. Hoch, J. C.; Maciejewski, M. W.; Mobli, M.; Schuyler, A. D.; Stern, A. S., Nonuniform Sampling and Maximum Entropy Reconstruction in Multidimensional NMR. *Accounts of Chemical Research* **2014**, *47*, 708-717.

9. Pelczer, I.; Szalma, S., Multidimensional NMR and Data Processing. *Chemical Reviews,* **1991***, 91*, 1507-1524.

10. Schröter, C.; Lee, J. C.; Schultz, T., Mass-correlated rotational Raman spectra with high resolution, broad bandwidth, and absolute frequency accuracy. *Proceedings of the National Academy of Sciences* **2018,** *115* (20), 5072-5076.

11. Lee, J. C.; Lee, D. E.; Schultz, T., High-resolution rotational Raman spectroscopy of benzene. *Physical Chemistry Chemical Physics* **2019,** *21* (6), 2857-2860.

12. Sumner P. D.; Mark C. A.; James W. B., Fourier Transform Spectrometry, *Academic Press*; 1st edition, **2001**, 119

13. Western, C. M.; Billinghurst, B. E. Automatic assignment and fitting of spectra with PGOPHER. *Physical Chemistry Chemical Physics*, **2017**, *19(16)*, 10222-10226

Chapter III. Linear Molecule

3.1 Introduction

All linear molecules have anisotropic polarizability and are Raman active. However, many linear molecules have no permanent dipole moment, so microwave spectroscopy cannot be used to measure their spectra. Linear molecules have a simple rotational structure, and their spectrum is easy to analyze. There are many kinds of linear molecules, but here I only discuss carbon disulfide (CS_2).

The rotational constants of any molecule are labeled *A*, *B*, *C* and describe the inertial moment associated with the three molecular axes. In the linear molecule, motion around the axis parallel to the molecular bonds does not correspond to molecular rotation, and the other two axes have the same moment of inertia. Linear molecules therefore have only one distinct rotational constant, called *B,* and, if necessary, a corresponding distortion constant *D*. Because it is easy to analyze experimental results for linear molecules, many kinds of rotational spectroscopy were benchmarked with linear molecules. Raman transitions in linear molecules are only allowed for changes in the rotational quantum number $\Delta J = \pm 2$. In our experiment, we do not characterize the sign of ΔJ, so the selection rule can be described by $\Delta J = +2$. The rotational state energy *F*, linear transition energies ΔF_{linear} and Raman transition energies ΔF_{Raman} of a linear molecule, as function of the rotational quantum number J, the rotational constant *B* and the distortion constant *D* are given by the equation:

$$F(J) = B \cdot J(J+1) - D \cdot J^2(J+1)^2$$

$$\Delta F_{\text{linear}}(J) = 2B \cdot (J+1) - 4D \cdot (J+1)^3$$

$$\Delta F_{\text{Raman}}(J) = F(J+2) - F(J) = (4J+6) \cdot (B - 2D \cdot (J^2 + 3J + 3))$$

Winther et al. measured the IR spectrum of CS_2 in the ν_3 band region in 1987 and observed 24 bands of CS_2 isotopomers ($^{32}S_2{}^{12}C$, $^{34}S^{12}C^{32}S$, $^{33}S^{12}C^{32}S$, $^{34}S_2{}^{12}C$, $^{32}S_2{}^{13}C$, and $^{34}S^{13}C^{32}S$).[1] In 1997, Ahonen et al. measured accurate rotational constant of CS_2 with a Bruker IFS 120 HR spectrometer.[2] Horneman et al. measured bands of $^{13}CS_2$ with CO_2 lasers in 2005.[3]

Other CS_2 measurements were based on rotational coherence spectroscopy (RCS). Heritage et al. observed a rotational wave packet for CS_2 for the first time in 1975.[4] They observed short-duration birefringence in CS_2 vapor with Nd^{3+} laser pulses. Kummli et al. recorded RCS data using a 3300 ps optical delay with femtosecond degenerate four-wave mixing in 2006 and determined rotational constants of the ground and vibrationally excited states.[6] The highest resolution RCS experiments were performed with a 2 m range opto-mechanical delay stage and observed rotational wave packets up to 6 ns delay. Based on the Heisenberg energy uncertainty, the resolution limit is close to 100 MHz in this RCS experiment.

Schröter et al. resolved rotational Raman spectra for multiple isotopologues of CS_2 with mass-CRASY and determined their rotational structure with a 2 ns delay in 2011. Their two-dimensional spectra resolved rotational constants for 10 isotopologues with a single measurement. Below I show how we improved the resolution to ~ 3 MHz with a 300 ns scan to obtain more accurate rotational constants.

3.2 Experiment and Results

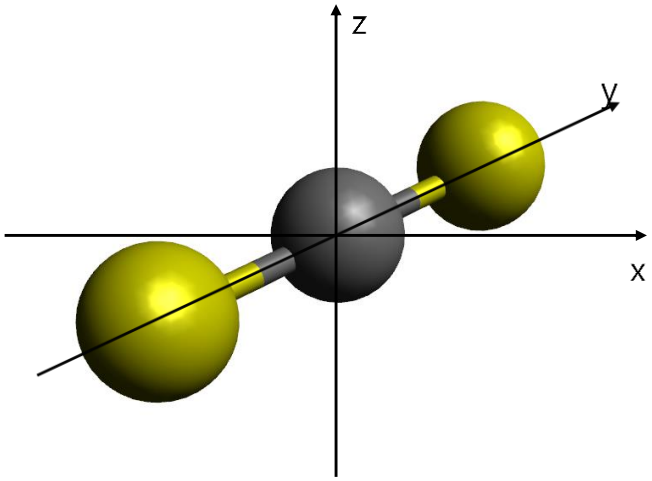

Figure 3.1. CS_2 molecular structure. Three main axes of CS_2 are labelled with x, y, and z. Rotation for the y-axis is irrelevant and the moment of inertia with respect to the x and z axes are the same.

Carbon disulfide (CS_2) is one of the easiest molecules to observe in a rotational alignment experiment. The molecular structure of CS_2 is shown in Figure 3.1. CS_2 is a linear molecule and its high vapor pressure (48 kPa) means that it is easily detected in a molecular beam. The simple rotational structure makes it easy to see the revival signal in the time domain and many types of alignment experiments were performed with CS_2. In our experiment, CS_2 was helpful to optimize and characterize the experimental set-up. To this point, it is a reference molecule for our experiment.

Figure 3.2 shows a measured mass spectrum and illustrates the many isotopologues and fragmentation channels of CS_2. We observe heavy isotope signals (77 u, 78 u, 79 u, and 80 u) and fragments in lower mass channels (32 u, 33 u, 34 u, 44 u, 45 u, 46 u, 64 u, 65 u, and 66 u).

Figure 3.3 shows the data analysis process to get the rotational spectrum of CS_2 from mass-CRASY data. In the mass spectrum, we observe multiple CS_2 isotopologues (mass channels 76 u, 77 u, 78 u, 79 u, and 80 u) and Table 3.1 shows all possible isotopologues with their natural abundance.[9] The alignment pulse generated a coherent wave packet in all isotopologues. Time-resolved mass spectrometry acquired the modulation of the signal in each mass channel. Fourier analysis produced a frequency spectrum from each mass channel.

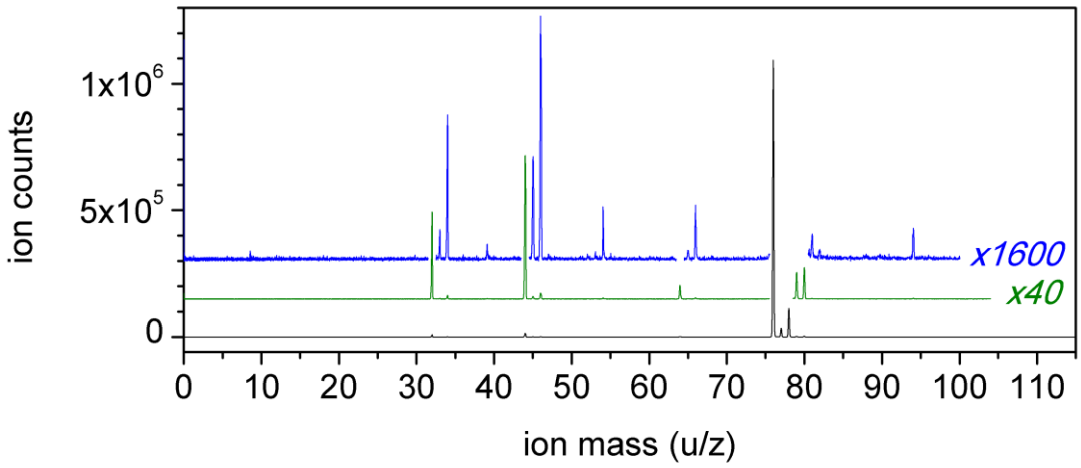

Figure 3.2. Mass spectrum of CS_2. This spectrum showed the parent ions (76 u) and heavy isotopologues. (77 u to 83 u). The spectrum also showed fragments of CS_2 (32 u, 33 u, 34 u, 44 u, 45 u, 46 u, 64 u, 65 u, and 66 u).

Table 3.1. All CS_2 isotopologues in natural abundance. The amplitudes in our mass spectra are approximately proportional to the reported abundance.[9]

Mass	Isotope	Abundance
76	$^{32}S^{12}C^{32}S$	0.893
77	$^{32}S^{13}C^{32}S$	0.00965
	$^{32}S^{12}C^{33}S$	0.0141
78	$^{32}S^{12}C^{34}S$	0.0799
	$^{32}C^{13}C^{33}S$	0.0001522
	$^{33}S^{12}C^{33}S$	0.0000556
79	$^{32}S^{13}C^{34}S$	0.000864
	$^{33}S^{12}C^{34}S$	0.000631
	$^{33}S^{13}C^{33}S$	0.000000602
80	$^{34}S^{12}C^{34}S$	0.00179
	$^{32}S^{12}C^{36}S$	0.000188
	$^{33}S^{13}C^{34}S$	0.000000682
81	$^{34}S^{13}C^{34}S$	0.0000193
	$^{32}S^{13}C^{36}S$	0.00000203
	$^{33}S^{12}C^{36}S$	0.00000148
82	$^{34}S^{12}C^{36}S$	0.00000833
	$^{33}S^{13}C^{36}S$	0.0000000165
83	$^{34}S^{13}C^{36}S$	00000000927
84	$^{36}S^{12}C^{36}S$	0.0000000396
85	$^{36}S^{13}C^{36}S$	0.0000000004

In the following paragraph, I describe the result from a CRASY measurement, which at the time of its measurement represented the highest resolution rotational Raman spectrum ever measured. A small step-size of 1 ps, translated into a spectral bandwidth of 500 GHz, which is enough range to observe the full spectrum in the cold molecular beam. The maximal measurement delay was 312.832 ns and we acquired 17,110 mass spectra (about 5.4%, sampling rate based on the 1 ps step size). The alignment trace was calculated from signal S(t), a reference signal R(t), and their respective averages S, R via: T(t) = S(t)/R(t) – average (S/R). The alignment trace was multiplied with a Kaiser window function. The resolution was 2.9 MHz, 150 times better than the first CRASY results (500 MHz).[7,8] Compared to a continuous scan, the sparse scan led to an increase of the noise: the noise floor is 30 times higher (see Figure 3.4). Differences in signal integration and ion count rate explained part of the noise difference: The continuous scan collected signal from 3000 laser shots for each mass spectrum with an ion count rate of ~ 3 ions per shot, whereas the sparse scan collected signal for 1000 laser shots per mass spectrum at an ion count rate of ~0.6 ions per shot. The shorter signal integration and lower ion count rate increased the noise in the sparse scan.

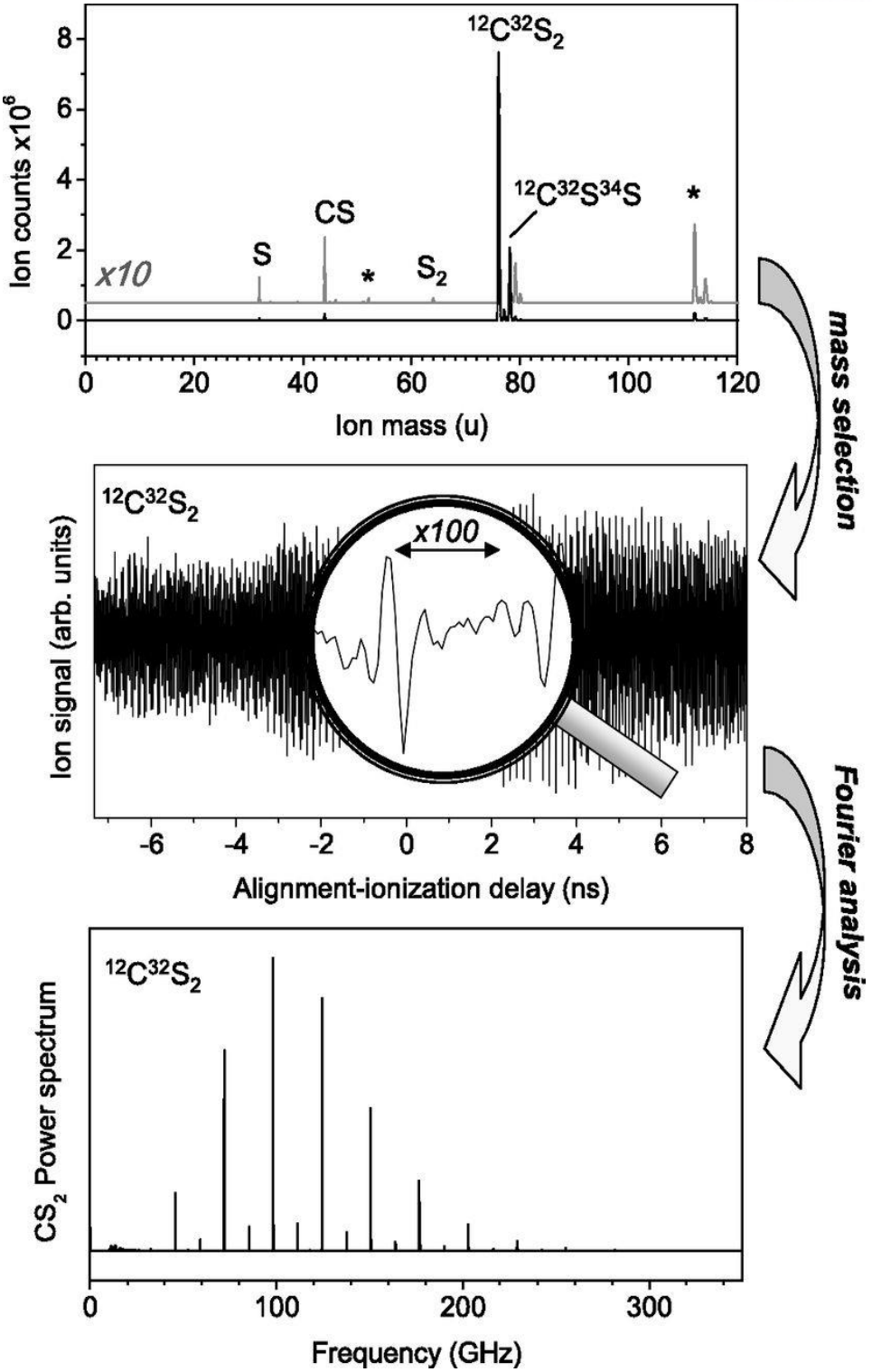

Figure 3.3. Analysis of CRASY data for CS_2. Top. The mass spectrum of CS_2 shows fragments and isotopologues at natural abundance. Stars mark signals from sample impurities. Middle. For the selected mass channel 76 u, the time-dependent signal shows clear rotational coherence, leading to signal modulation. An enlarged inset shows the wave packet for a 50 ps period. Bottom. Fourier transformation of the time trace reveals the mass selective rotational Raman spectrum.[8]

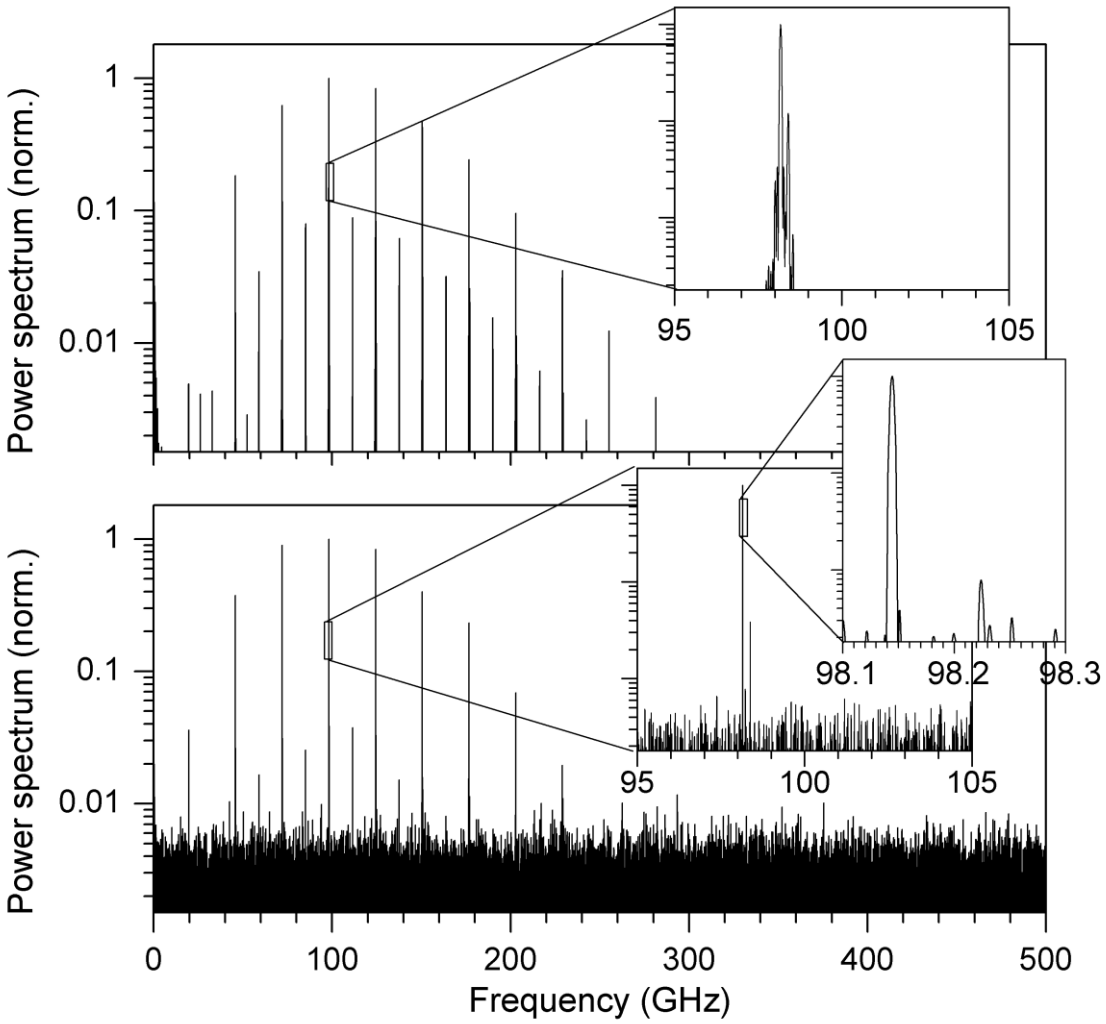

Figure 3.4. Comparison of CS_2 rotational Raman spectra. Top. Spectrum obtained from continuous 15.3 ns scan with 1 ps step-size. Bottom. Spectrum obtained by random sparse scanning of a 312.8 ns scan. The enlarged insets shows the difference in resolution between the spectra.[8]

The CS_2 sparse scan also gave spectra for many isotopologues and fragments. Table 3.2 summarizes the fitted rotational constants. Parent ion (mass 76 u) signal gave 9 lines for the vibrational ground state Σ_{1g} and I fitted its rotational constant B = 3271.5170(7) MHz and distortion constant D = 355(3) Hz. The distortion constant's low precision is explained by the fact that we have only assigned low rotational states.

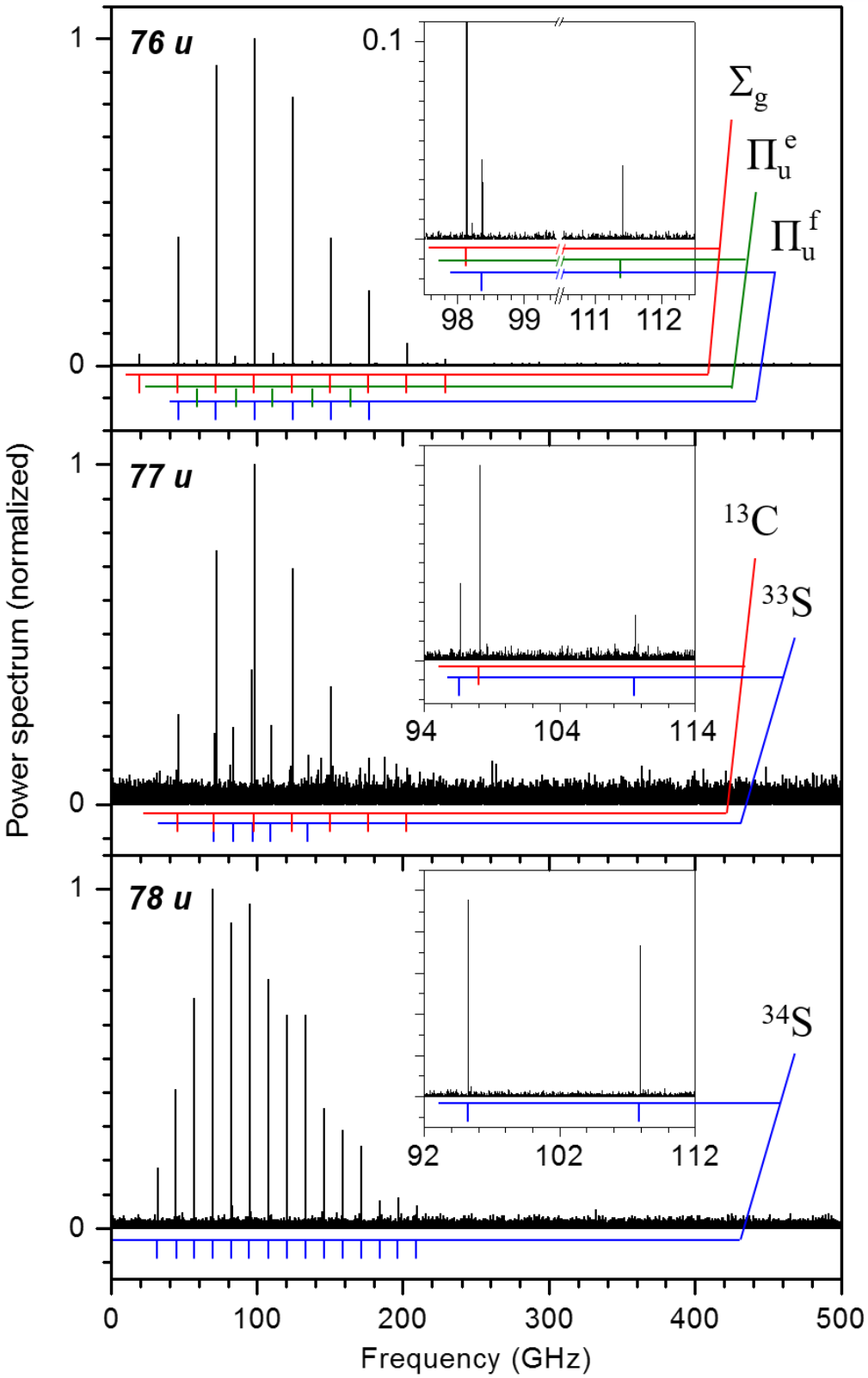

Figure 3.5. The isotopologue rotational spectra for 76 u, 77 u, and 78 u. **Top**. The spectrum for the parent ions signal shows progressions for one vibrational ground state and two vibrationally excited states. **Middle**. The spectrum for mass 77 u shows a mixed spectrum of $^{13}C^{32}S_2$ and $^{33}S^{12}C^{32}S$ isotopologues. **Bottom**. The 78 u spectrum is predominantly from the $^{34}S^{12}C^{32}S$ isotopologue.[8]

In Figure 3.5, I show the high-resolution rotational Raman spectra for several CS_2 isotopologues. In mass channel 76 u, we assigned three rotational spectra. The rotational spectrum in the vibrational ground state (Σ_g) is marked with red color. In addition to the ground state spectrum, the 76 u rotational spectrum also showed several peaks from a vibrationally excited state involving the doubly degenerate bending mode Π_u. This bending mode leads to rovibrational splitting (*l*-type splitting) of each rotational state with the term $q(J(J+1))$.[1] The *l*-type splitting can be described by an effective rotational constant $B_{eff} = B \pm 1/2 \cdot q$. Due to the molecular Fermi statistics, we can only observe odd J states of Π^e_u and even J states of Π^f_u symmetry. The fit gave an effective rotational constant for Π^e_u of B = 3276.738(9) MHz and a distortion constant D = 347(58) Hz. The effective rotational constant for Π^f_u was B = 3279.064(7) MHz and the distortion constant was D = 386(38) Hz. From these constants, we derived for the Π_u state, B = 3.277901(10) GHz and D = 367(68) Hz and an l-type splitting constant of q = 2.327(10) MHz.

Our CS_2 mass CRASY resolved various isotopologues at their natural abundances (^{13}C: 1.1%, ^{33}S: 0.75% and ^{34}S: 4%) in the corresponding isotopologue mass channels. For mass 77 u, we assigned 5 lines for $^{13}C^{32}S_2$ and 7 lines for $^{33}S^{12}C^{32}S$. The fitted rotational constants are 3271.6346(13) MHz, 346(7) Hz, and 3221.8494(26) MHz, 329(13) Hz, respectively. For the $^{34}S^{12}C^{32}S$ isotopologue in the mass channel 78 u, we assigned 15 lines and fitted constants of B = 3175.0204(12) MHz and D = 318(6) Hz. In mass channel 79 u, six lines for the $^{34}S^{13}C^{32}S$ isotopologue were assigned and in mass channel 80 u six lines emerged above the sampling noise for $^{34}S^{12}C^{34}S$. In 2020, I measured CS_2 spectra with saturated signals for the main isotopologue to increase the signal in mass channels 79 u and 80 u with a 200 ns scan. Figure 3.6 illustrates the saturated measurement spectra for 79 u and 80 u. The signal-to-noise

Table 3.2. All isotopologues with assigned rotational spectra in our mass-CRASY measurements. Rotational constants are given in kHz and distortion constants in Hz.

			Rotational Constant, *B*		Centrifugal Distortion, *D*	
Isotopologue	Mass	State	CRASY	Literature	CRASY	Literature
$^{32}S^{12}C^{32}S$	76	Σ_g	3,271,517.0(0.7)	3,271,516.5(1.5)[2]	355(3)	352.79(9)[2]
	76	Π^e_u	3,276,738(9)	3.276,759(12)[1]	347(58)	359.1(6)[1]
	76	Π^f_u	3,279,064(7)	3,279,077(11)[1]	386(38)	360.6(6)[1]
$^{32}S^{13}C^{32}S$	77	Σ_g	3,271,634.6(1.3)	3,271,637.8(0.3)[3]	346(7)	350.76(2)[3]
$^{32}S^{12}C^{33}S$	77	Σ_g	3,221,849.4(2.6)	3,221,843(11)[1]	329(13)	341.3(1.1)[1]
$^{32}S^{12}C^{34}S$	78	Σ_g	3,175,020.4(1.2)	3,175,024(8)[1]	318(6)	332.6(5)[1]
$^{32}S^{13}C^{34}S$	79	Σ_g	3,175,120(18)	3,175,115.1(1.3)[3]	318(95)	332.94(15)[3]
			3.175,132(7)†		394(22)†	
$^{34}S^{12}C^{34}S$	80	Σ_g	3,079,422(9)	3,079,377(27)[1]	339(48)	346(16)[10]
			3.079,427(7)†		305(22)†	

† Data from 2020, saturated measurement of a 200 ns sparse scan.

ratio is better than in earlier data and I assigned six lines for mass 79 u and 8 lines for mass 80 u. The rotational constants for corresponding isotopologues were determined with much better accuracy by this last measurement. All rotational constants are summarized in Table 3.2.

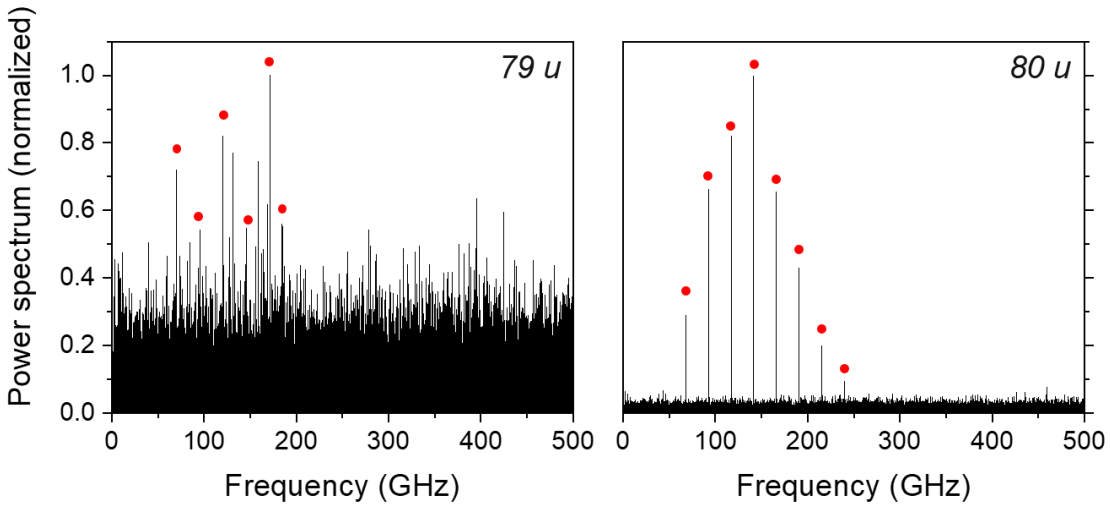

Figure 3.6. Isotopologue rotational spectra for mass channel 79 u and 80 u. We saturated the main isotopologue signal and this increased the signals of heavy isotopologues. This measurement scanned a 200 ns delay range in a 20 % sparse scan. Red dots mark the transition lines that were assigned and fitted.

3.3 Discussion

The spectroscopic resolution of traditional Raman spectroscopy was limited by the dispersing optics in grating or prism-based measurements. Dispersive spectrometers have generally low resolution as compared to FTWM or laser scanning experiments (see Table 2.1) and will not be further discussed here. The longest delay used in RCS experiments was in the range of a few nanoseconds with up to 2 m range translation stages. In this thesis, we describe the first CRASY experiments based on the electronic pulse selection technique. This experimental setup breaks the previous delay limitations with a lab-sized interferometer experiment. A 16-fold folded mechanical delay stage increased the range to 4.8 m, which is equivalent to a 16 ns delay. By using a delay generator to select oscillator pulses, we made it possible to increase the time delays to arbitrarily large values. A frequency counter measured the laser oscillator frequency against a highly accurate GPS clock and calibrated frequencies to improve the accuracy of our results. The highest-resolution measurement reported in this chapter scanned a delay exceeding 300 ns, thereby offering a spectroscopic resolution below 3 MHz.

Our CS_2 CRASY experiment resolved many isotopologue rotational spectra with a single measurement and without any isotopic enrichment. The accuracy of almost all isotopologue rotational constants was

improved as compared to literature values. For the most abundant isotopologue, the CS_2 rotational constant B was determined with < 1 kHz accuracy and for other isotopologues, we achieved few-kHz accuracies. A measurement with saturated signal in 2020 contributed precise rotational constants for rare isotopologues at mass 79 u and 80 u.

According to the Shannon-Nyquist theorem, the spectroscopic range of Fourier-transform spectra cannot exceed 1/(2 step size). Measurements reported in this chapter were performed with a 1 ps step size and we obtain 500 GHz broadband spectra. Each data set collected more than 15,000 mass spectra for signal and reference and each mass spectrum contained 150,000 points along the TOF mass axis.

Figure 3.7 shows the comparison of time traces for a continuous scan and a sparse scan. The sparse data collection reported in this chapter was the first trial of random sparse sampling for CRASY and demonstrated that we can greatly reduce the measurement time and data quantity. The benefit of sparse sampling is much larger than the trade-off demerit. The accuracy and resolution increase proportionally to the scan range. The signal-to-noise ratio decreases with sparse sampling but still allows the

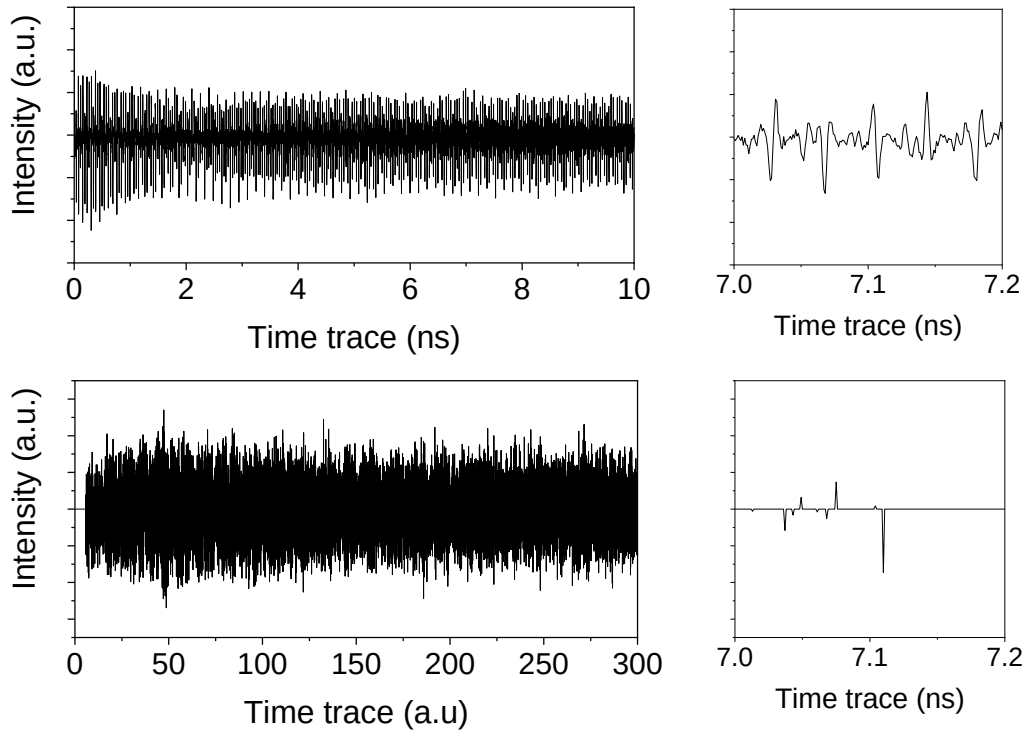

Figure 3.7. The comparison of continuous and sparse time traces. Top. Continuous scan with 1 ps step-size. Bottom. Sparse scan with 5.4 % sparse sampling. The enlarged trace shows the difference between sparse and continuous scan. Both traces show signal modulation for CS_2 and are based on a comparable number of acquired mass spectra. But the sparse scan allowed to determine the CS_2 rotational constant with order-of-magnitude better accuracy.

assignment of rotational bands. For CS_2, the sparse data allowed to fit rotational constants with order-of-magnitude better accuracy. The result convinced us that this method can be used for our future work.

Our GPS synchronized clock monitoring system creates a time-domain equivalent to frequency comb measurements. Of course, highest-accuracy frequency comb measurements against an atomic clock can have much higher accuracy than our commercial GPS clock can offer. However, the basic idea is the same: an external clock can measure highly accurate oscillator repetition rates. As opposed to frequency comb measurements, a phase-locked oscillator is not required for CRASY, but merely a stable oscillator frequency that allows frequency measurements with small errors. Our system calculates the pulse jump delay from the current oscillator frequency, and this corrects errors when the frequency drifts. Just like data from frequency comb spectroscopy, CRASY data is thereby calibrated against an external clock, locking measured spectroscopic frequencies against a precise reference. Hence, we can call our method a time-domain equivalent to frequency comb spectroscopy.

3.4 Conclusion

Our high-resolution method makes it possible to increase the resolution of interferometer experiments without large interferometers. Our application of the extended interferometer time delays overcame previous limitations for rotational Raman spectroscopy. With the resulting increase of resolution, we could resolve rotational transitions that remained unresolved before. The time delay of our experiment reached over 300 ns and the resolution reached 3 MHz. Our new type of time-delay system can, in principle, increase time delays to infinite values.

The correlation between mass and rotational information allowed us to analyze isotope effects in this experiment. All rotational constants for CS_2 isotopologues listed in Table 3.2 could be obtained with a single measurement. We used just a commercial CS_2 sample without any isotopic enrichment and this result proves that CRASY can resolve heterogeneous samples without any purification. We conclude that our method is an efficient and economical technique to analyze molecular properties in heterogeneous samples. Future experiments will try to analyze heterogeneities in biological tautomers, such as cytosine.

3.5 References

1. Winther, F.; Heyne, U.; Guarnieri, A., The Infrared Spectrum of CS_2 in the ν_3 Band Region. *Z. Naturforsch 43a*, 215-218.

2. Ahonen, T.; Alanko, S.; Horneman, V. M.; Koivusaari, M.; Paso, R., Tolonen, A. M., Anttila, R., A Long Path Cell for the Fourier Spectrometer Bruker IFS 120 HR: Application to the Weak $\nu_1 + \nu_2$ and $3\nu_2$ Bands of Carbon Disulfide. *Journal of Molecular Spectroscopy,* **1997**, 181, 279-286.

3. Horneman, V. M.; Anttila, R.; Alanko, S.; Pietilä, J. (2005). Transferring calibration from CO_2 laser lines to far infrared water lines with the aid of the ν_2 band of OCS and the ν_2, $\nu_1 - \nu_2$, and $\nu_1 + \nu_2$ bands of $^{13}CS_2$: Molecular constants of $^{13}CS_2$. *Journal of Molecular Spectroscopy*, **2005,** 234(2), 238-254.

4. Heritage, J. P.; Gustafson, T. K.; Lin, C. H. Observation of Coherent Transient Birefringence in C S_2 Vapor. *Physical Review Letters*, **1975,** 34(21), 1299.

6. Kummli, D. S.; Frey, H. M.; Leutwyler, S., Femtosecond degenerate four-wave mixing of carbon disulfide: High-accuracy rotational constants. *Journal of Chemical Physics,* **2006,** 124(14), 144307

7. Schröter, C.; Kosma, K.; Schultz, T., CRASY: mass-or electron-correlated rotational alignment spectroscopy. *Science* **2011,** *333* (6045), 1011-1015.

8. Schröter, C.; Lee, J. C.; Schultz, T., Mass-correlated rotational Raman spectra with high resolution, broad bandwidth, and absolute frequency accuracy. *Proceedings of the National Academy of Sciences* **2018,** *115* (20), 5072-5076.

9. D. R. Lide, *CRC Handbook of Chemistry and Physics*, 86th ed; CRC: Boca Raton, FL, **2005**

10. Cheng, C. L. C.; Hardwick, J. L.; Dyke, T. R. High-Resolution Vibration–Rotation Spectroscopy of $^{12}C^{34}S_2$ and $^{13}C^{34}S_2$ at 400 cm^{-1}. *Journal of Molecular Spectroscopy*, **1996,** 179(2), 205-218.

Chapter IV. Symmetric Top Molecules

4.1 Introduction

Symmetric top molecules, such as benzene and benzene-d6, have no permanent dipole moment and they cannot be observed by microwave spectroscopy. Therefore, the rotational constants for those molecules must be obtained by Raman spectroscopy or the observation of rotational structure in vibrational or electronic spectra. Table 4.1 compares the rotational constants of benzene obtained with experimental methods other than CRASY. The published values were obtained with numerous different experimental techniques.

We must consider two rotational quantum numbers, J and K, to describe the rotational transitions of symmetric top molecules. According to the Raman selection rules, ΔK must be zero and K only affects spectral line positions through the distortion constants. The K-splitting for ΔJ transitions is small but, with high-enough resolution, it should be possible to resolve this splitting. High-resolution microwave spectroscopy would have the resolution to resolve K-splitting but cannot observe symmetric top molecules, which are non-polar. Past rotational Raman spectroscopy had insufficient resolution to resolve K-splitting in symmetric tops, except for the case of ammonia where the rotational constant is exceptionally large.[1] In this chapter, I describe our attempt to resolve the K-structure of benzene with high-resolution CRASY.[2]

4.2 Experiment and Results

Symmetric top molecules have two equal moments of inertia for two principal molecular axes. We distinguish two types: (1) In a prolate top, the inertial moments are $I_A < I_B = I_C$ (rotational constants $A > B = C$) and (2) In a oblate top, the inertial moments are $I_A = I_B > I_C$ (rotational constants $A = B > C$). When analyzing the rotational spectrum of the symmetric top, we only consider two rotational constants and distortion constants.

Prolate Top:

$$F(J) = B \cdot J^2 + (A - B) \cdot K^2 - D_J \cdot J^2(J+1)^2 - D_{JK} \cdot J(J+1)K^2 - D_K \cdot K^4 + H_J \cdot J^3(J+1)^3 + H_{JK} \cdot J^2(J+1)^2K^2 + H_{KJ} \cdot J(J+1)K^4 + H_K \cdot K^6$$

Oblate Top:

$$F(J) = B \cdot J^2 + (B - C) \cdot K^2 - D_J \cdot J^2(J+1)^2 - D_{JK} \cdot J(J+1)K^2 - D_K \cdot K^4 + H_J \cdot J^3(J+1)^3 + H_{JK} \cdot J^2(J+1)^2K^2 + H_{KJ} \cdot J(J+1)K^4 + H_K \cdot K^6$$

Energy differences:

$$\Delta F = 2B \cdot (J+1) - 4D_J \cdot (J+1)^3 - 2D_{JK} \cdot (J+1)K^2 + H_J \cdot (J+1)^3[(J+2)^3 - J^3]$$

$$+ 4H_{JK} \cdot (J+1)^3 K^2 + 2H_{KJ} \cdot (J+1) K^4$$

The asymmetry parameter, κ, can be used to characterize a molecule as prolate top, oblate top, or asymmetric top.

$$\kappa = \frac{2B - A - C}{A - C}$$

When κ is -1, the molecule is a prolate top; when κ is 1, is the molecule is an oblate top; and all intermediate values characterize an asymmetric top.

In a symmetric top, we must consider the quantum number $J = 0, 1, \ldots$ and also the quantum number $K = J, J-1, \ldots, 0, \ldots, -J$. The Raman selection rule for the symmetric top is $\Delta K = 0$ and $\Delta J = 0, \pm 1, \pm 2$ (for $K = 0$, only $\Delta J = \pm 2$ is allowed). Due to the molecular symmetry, one of the rotational constants A or C cannot be measured.

4.2.1 Benzene

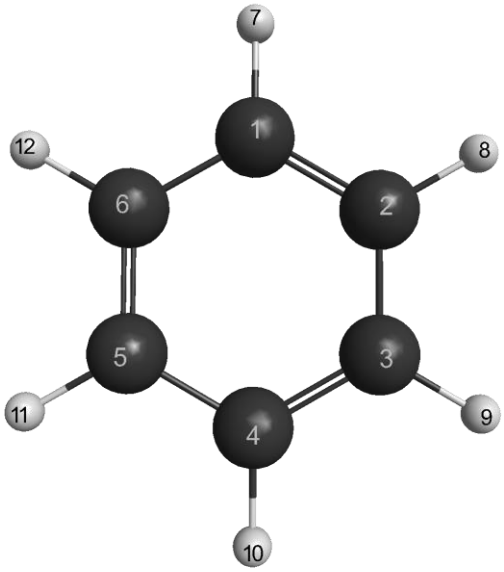

Figure 4.1. The molecular structure of benzene.

The benzene molecule is one representative symmetric top molecule (oblate top) and a simple aromatic molecule (see Figure 4.1). It cannot be observed with microwave spectroscopy because it has no permanent dipole moment. The only measurements capable to determine rotational constants for a

molecule like benzene is Raman scattering, rovibrational, or rovibronic spectroscopy. The first rotational Raman spectrum for benzene was measured by Stoicheff in 1953.[3] Their result had a resolution of only a few GHz, the obtained rotational constant *B* was 5684.1(1.5) MHz and the authors calculated bond lengths with sub-picometer accuracy based on their data. Riehn et al.[4] observed benzene with time-domain rotational coherence spectroscopy in 2001 and reported values for *B* between 5687.7 MHz and 5689.25 MHz. Their theoretical resolution limit was 153 MHz FWHM resolution based on their 4 ns scans.[5-6] Note that the authors analyzed their data in the time domain and did not specify the experimental resolution.

Vibrational and electronic spectroscopy also contributed to the structure determination of benzene. After 1954, rovibrational or rovibronic spectroscopy was used to measure the benzene rotational constant.[7] All experimental values are summarized in Table 4.1. The literature values are significantly different and often disagree by many multiples of the stated sigma errors.

Table 4.1. Comparison between literature values and CRASY results for ground-state rotational constants of benzene. GRR: Grating-based rotational Raman spectroscopy; GV: Grating-based rovibrational spectroscopy; GVR: Grating-based vibrational Raman spectroscopy; FV: Fourier-transform rovibrational spectroscopy; LV: Laser scanning rovibrational spectroscopy; LVC: Laser scanning rovibronic spectroscopy; RCR: Rotational coherence Raman spectroscopy.

B_0 (MHz)	D_J (Hz)	D_{JK} (Hz)	Method	Year	Citation
5684.1(1.5)	660(300)		GRR	1954	7
5685.3(3.0)	360		GV	1958	15
5688.6(1.0)			GV	1968	10
5692.40(39)	1619(6)		GV	1974	14
5688.59(75)	1260(180)	-3597(1798)	GVR	1979	11
5688.69(18)	1097(36)	-2068	FV	1980	19
5688.916(21)	1179(23)	-2069(72)	LV	1982	20
5689.248(45)	1191(11)	-2041(48)	LV	1988	12
5689.266(6)	1231(1)	-2065(3)	FV	1990	21
5689.2781(10)	1242(10)	-2059(22)	LV	1991	18
5689.241(13)	1477(88)	-2530(202)	LV	1991	17
5689.220(26)	960(7)	-1960(210)	LVC	1999	13
5689.10(14)			RCR	2001	6
5687.7(3.0)	1300(100)	-3000(1200)	RCR	2002	4
5688.95(55)	1100(200)	-1400(400)	RCR	2002	5
5689.212(9)	1220(10)	-1978(33)	LVC	2004	16
5689.2671(52)	1178(50)	-2300(120)	CRASY	2018	2

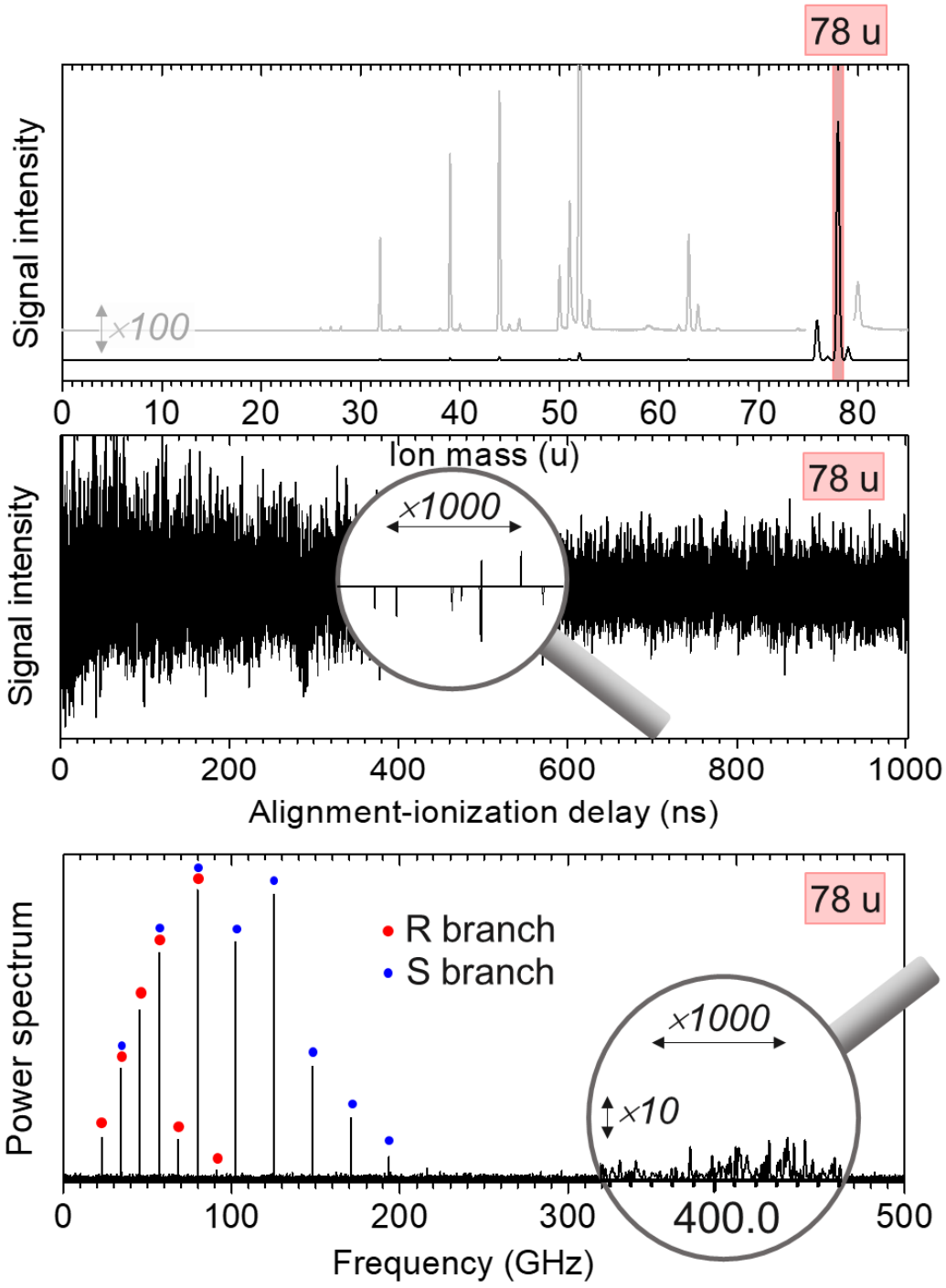

Figure 4.2. Data set of a mass-CRASY benzene measurement. **Top**. The mass spectrum resolved benzene (78 u), its fragments, and residual CS_2. **Middle**. The time trace of mass channel 78 u, recorded up to 1 μs time delay. The enlarged inset shows a 1000-times zoom into the x-axis and shows the sparse sampling. **Bottom**. The spectrum, after Fourier transformation, reveals the rotational bands of benzene. Red dots mark the R branch and blue dots mark the S branch.

CRASY is based on the same idea as RCS, both observe non-adiabatic alignment dynamics.[8,9] Benzene was the first symmetric top molecule that was measured with CRASY. Benzene has 13.3 kPa vapor pressure and the high vapor pressure makes it easy to find gas phase benzene signal. The 200 nm wavelength nicely ionizes benzene and we used the same beamline as for our CS_2 CRASY experiments. We used 800 nm, 100 μJ, ~1 ps alignment pulses, and 200 nm, 1 μJ, 45 fs probe pulses. The backing pressure behind the pulsed valve was 5 bar with benzene entrained in helium carrier gas and the source chamber pressure was 10^{-5} mbar to 10^{-6} mbar. The Even-Lavie valve opening time was 10.0 μs. In our highest-resolution measurement, the final time delay was 1 μs and the measurement sampled 20,000 mass spectra with a sparse 1 ps step size.

The data shown in Figure. 4.2 comes from our first-microsecond time delay measurement, resulting in a 1 MHz rotational resolution. The spectrum contained benzene and small amounts of carbon disulfide, which remained in the sample line from an earlier experiment. The mass spectrum, Fig. 4.2-Top, shows benzene and its fragments at masses 78 u, 63 u, 52 u, 39 u and weak CS_2 and corresponding fragment signals at 76 u, 44 u, and 33 u. Fig. 4.2.-Middle, shows the signal modulation of the parent ion signal at 78 u. The time trace was calculated from signal S(t), a reference signal R(t), and their respective averages S, R via: T(t) = S(t)/R(t) – average (S/R). The reference signal trace was generated with a 2000 points wide Hann window. An inset of Figure 4.2.-Middle shows the sparse scanning of the trace: data was only measured at 2% randomly selected points along a time axis spanning a 1 μs delay range with a nominal 1 ps step size. The unapodized resolution of a 1 μs time scan reaches 0.61 MHz FWHM.

Fourier transformation of each mass channel revealed frequencies and amplitudes of all Raman excited states in the rotational wave packet. Figure 4.2-Bottom shows the result of the parent ion signal (78 u). The rotational spectrum showed two progressions, one for the R-branch ($\Delta J = 1$) and one for the S-branch ($\Delta J = 2$). The highlighted inset reveals the elevated noise due to sparse sampling. A CS_2 spectrum was produced with the same procedure for the mass channel 76 u. 23 Benzene bands were assigned by comparison to oblate top term energies, using literature constants of B_0 = 5689.27809 MHz, $C = B/2$, D_J = -1242.8 Hz, and D_{JK} = -2059.1 Hz. We assumed a rotational temperature of 4 K by comparison of the experimental and the simulated spectrum envelope. A fit of the assigned bands with PGOPHER gave refined constants as summarized in Table 4.1. The fitted rotational constant B_0 agreed within 1σ accuracy with some references[4,5,10-12,21] but, not others.[6,7,13-20] In the same data set, we obtained a CS_2 spectrum and the fitted rotational constant was in reasonable agreement with literature values. Figure 4.3 shows a zoom into a few frequency regions. In these enlarged spectra, *K*-splitting is revealed as a broadening of the peaks, which increases with the *J*-state. The CS_2 spectrum shows no *K*-splitting.[2]

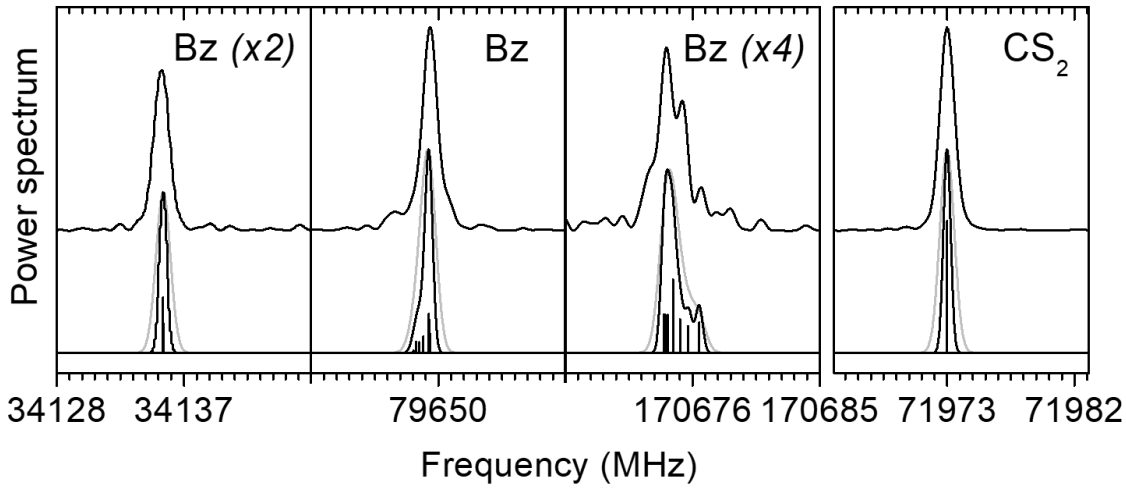

Figure 4.3. Selected regions of the benzene rotational spectrum (top traces). A PGOPHER simulated spectrum (bottom trace, folded with Gaussians of width 0, 0.61, and 1.2) shows the expected line-broadening due to K-splitting. The experimental resolution cannot distinguish individual lines. K-splitting is absent in the CS_2 spectrum.

The resolution of the spectrum is not enough to distinguish individual peaks for different *K*-states. This makes it harder to fit the benzene rotational constants. The shape of bands depends on the distortion constants and the temperature of the molecular ensemble. At higher *J*-state, *K*-splitting has a larger effect than for low *J* states. Our spectrum shows only relatively low *J* states, and this increases the uncertainty of the distortion constants. All high-resolution experiments for benzene are affected by the broadening and band shifts due to *K*-splitting. Resolving the *K*-structure will lead to more accurate rotational constants.

Figure 4.4 compares our result to literature values.[5-7,10,21] Early measurement had big errors compared to new experiments and significantly underestimated the rotational constant. The error for rotational constants may have occurred due to unresolved *K*-structure, uncertainties in the calibration standards, systematic errors, or perturbations from nearby states. Our data was measured with a frequency calibration based on the GPS stabilized clock and there is no danger of misassignment or perturbations in the pure rotational spectrum.

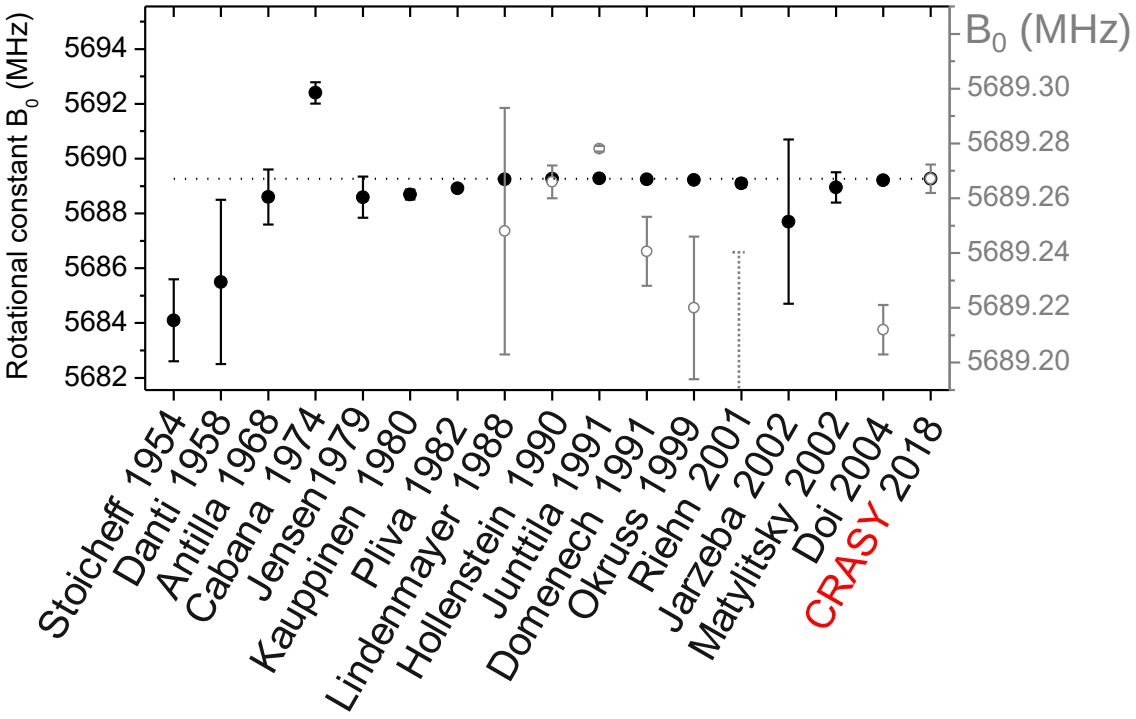

Figure 4.4. Comparison of B_0 and single sigma uncertainty from our measurement and in the literature. The right ordinate (data shown in grey and with open circles) is 100-fold enlarged as compared to the left ordinate (data shown in black and with full circles).

4.2.2 Benzene-d6

A second experiment on a symmetric top molecule was performed on deuterated benzene (benzene-d6). Benzene-d6 is fully substituted with deuterium. We used an isotopically enriched sample from Sigma Aldrich, with 99.6 atom % D. Benzene-d6 has similar thermodynamic properties as benzene, so the experimental conditions are the same as for benzene. We also experimented with a heterogeneous sample, with mixed benzene and benzene-d6 in a 50/50 ratio. The time delay of the measurement was 200 ns with 1 ps step-size, and 20,000 sampling points (20 % sparse sampling).

The first rotational characterization of benzene-d6 was performed by Danti et al., who measured parallel absorption bands with an infrared spectrometer.[14] J. Pliva et al. observed the vibrational bands of benzene-d6 in the 790-830 cm^{-1} region with high-resolution IR.[23] In 2003, Jarzeba et al. measured benzene-d6 with femtosecond degenerative four-wave mixing (fs DFWM) spectroscopy and they performed two different measurements, one using a gas cell and another using a supersonic jet.[5] Kunishige et al. resolved all deuterated isotopomers with microwave absorption spectroscopy.[24]

Fig. 4.5 shows the CRASY data for a 50/50 mixture of benzene and benzene-d6. The mass spectrum showed the expected benzene parent isotopologue signals at masses 78 u and 84 u with roughly equal signal size. ^{13}C isotopologue signals appeared at mass 79 u and 85 u. The dominant benzene fragments appeared at 66 u, 63 u (CD_3, CH_3 loss), 56 u, 52 u (C_2D_2, C_2H_2 loss), and 42 u, 39 u (C_3D_3, C_3H_3 loss). A signal at 76 u originated from residual CS_2 sample. The time trace for deuterated benzene showed the expected signal modulation for the complete scan range of 200 ns.

After Fourier transformation of this trace, the rotational-Raman spectrum for benzene-d6 was produced with a resolution of about 5 MHz. The experiment also resolved the rotational spectrum of benzene (78 u), $^{13}CC_5H_6$ (79 u), C_6D_5H (83 u), and $^{13}CC_5D_6$ (85 u). Table 4.2 shows the comparison of the rotational constants from CRASY and other recent measurements. The CRASY results are the best spectroscopic measurement to our knowledge.

Table 4.2. The rotational constants of benzene-d6, compared to recent literature values. Constants are given in MHz. Brackets denote a fixed value in the fit.

	CRASY	*W. Jarzeba*		*J. Pliva*	*S. Kunishige*
		Gas cell	*Supersonic jet*		
B	4707.3199(30)	4706.4(3)	4707.233(84)	4707.312(104)	4707.125(6)
D_J	0.785(13)e-3	0.41(4)e-3	[0.749e-3]	0.749(68)e-3	-
D_{JK}	-0.218(59)e-3	-0.22(30)e-3	[-1.251e-3]	-1.251(224)e-3	-

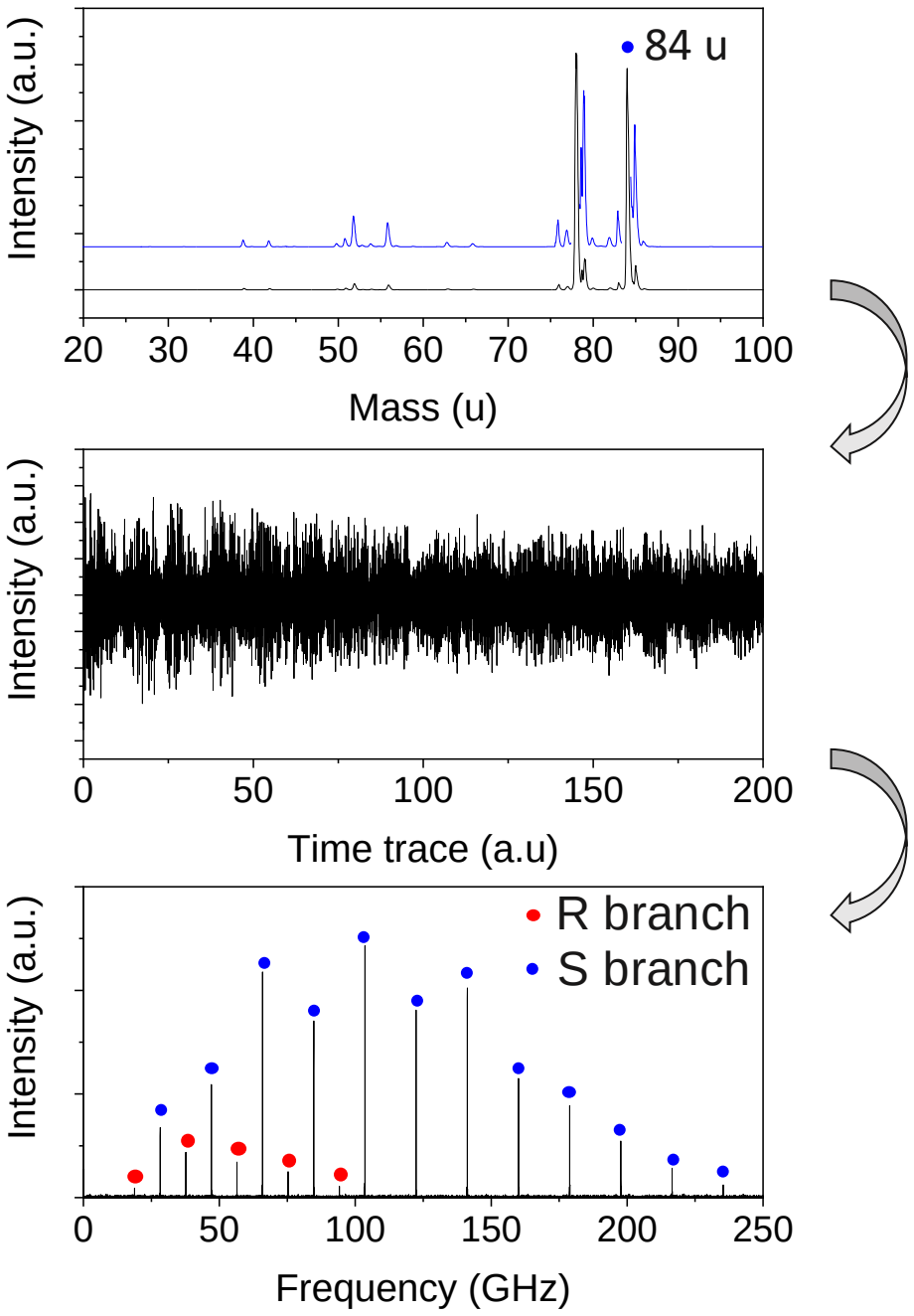

Figure 4.5. CRASY spectrum of an equal mixture of benzene-d6 and benzene. Top. Benzene (78 u) and benzene-d6 (84 u) isotopologue signals are of similar amplitude. Signals for heavy carbon isotopologues and fragments are weak. Middle. The time trace for mass channel 84 u. Bottom. The rotational Raman spectrum after Fourier transform of the time trace.

4.3 Discussion

Our results show that CRASY can successfully analyze the rotational structure of symmetric top molecules with high resolution. In the following discussion, we will compare the obtained resolution with that available from other spectroscopic experiments. Table 4.3. compares the resolution of different types of rotationally resolved spectroscopies. The experimental resolution presented here reached 1 MHz. This resolution is more than an order of magnitude better than that of any other high-resolution Raman spectroscopy (1.5 GHz grating-based spectroscopy, 300 MHz Raman FT spectrometers, and 30 MHz coherent anti-Stokes Raman scattering).[8, 11, 15, 16]

As mentioned earlier, the resolution of any Fourier transform technique is proportional to the observation time range. The best commercial Fourier-transform spectrometers are implemented with approximately 10 m long linear stages [11.7 m for the Bruker ETH-SLS 2009 FTIR spectrometer prototype at the Swiss Synchrotron Light Source[25]] and offer a non-apodized resolution down to approximately 24 MHz. However, such an installation is not realistic for a lab-sized experiment. Our data shown in Fig. 4.2 and 4.3 are based on a 1 μs scan, which is equivalent to a 300 m interferometer and offers order-of-magnitude better resolution than the best commercial interferometers. Our experiment therefore overcomes the fundamental limitations of traditional interferometers and offers greatly enhanced resolution in a lab-sized experiment.

High-resolution Fourier-transform microwave (FTMW) spectroscopy reaches few kilohertz resolution and accuracy with up to 10 GHz spectroscopic band range. In FTMW, Doppler broadening must be considered and is typically in the 100 kHz regime; Doppler broadening can be well-modeled but reduces the effective resolution. Still, the FTMW resolution is much higher than that of our novel high-resolution technique. To reach comparable resolution, our experiment needs to scan delays up to the 100 μs range, which is currently unfeasible because the molecular beam travels out of our interaction region. Future experiments will aim to address this issue by extending the region available for laser excitation and probing and by using slower molecular beams. Raman and microwave experiments are complementary methods and our experiments show that time-domain rotational Raman spectra can reach towards the high resolution regime of FTMW experiments.

The delay scanned for the benzene CRASY data set is the longest time delay that our group successfully scanned. Finally, the resolution of rotational Raman spectroscopy reached the 1 MHz resolution region.[2] In this experiment, we only measured 20,000 mass spectra which is just 2 % sampling of the whole-time delay range. With sparse sampling, our measurement time is the same as for scanning a 20 ns time delay with a continuous 1 ps step-size. Here we showed that 2 % sampling is enough to measure high resolution spectra and obtained accurate rotational constants.

The frequency counter with GPS-stabilized clock produced the accurate frequency calibration and this made it possible to get highly accurate rotational constants. High-resolution FTIR often obtains similar fit uncertainties to our CRASY results by fitting many lines in lower resolution spectra. But this only works if lines can be resolved and properly assigned, which can be a problem. CRASY has multiple advantages that amend those problems: we have higher resolution, less spectral congestions, colder molecules, and Raman selection rules (fewer lines). Also, FTIR needs to be calibrated whereas we have the best imaginable calibration, against a reference clock. So, the accuracy of CRASY should be more trustworthy, because there are less error sources in terms of calibration. Compared to FTMW, CRASY measures with skimmed molecular beams and this reduces Doppler broadening (skimmed-beam spectroscopy is also called 'Doppler-free spectroscopy').[28] Our calibration means that we can obtain fit accuracies that compete with FTMW results. Other Raman techniques require calibration and are far behind in attainable accuracy: Grating techniques are many orders-of-magnitudes worse in terms of resolution. Laser-based Raman experiments (CARS, etc.) have similar resolution to FTIR, but only for a tiny spectral range and the best RCS data has a resolution that is more than 2 orders of magnitude below that of our CRASY data.

Unfortunately, our experiment could not fully resolve the *K*-structure of benzene and we can only see the distorted band shapes of our R- and S-branch transition peaks. Comparison to a simulated spectrum shows that the broad peaks seem to be affected by *K*-splitting. I tried to perform a 2 μs measurement, but this also did not resolve the *K*-structure. Simulations indicate that ≤500 kHz resolution could be

Table 4.3. Resolution of rotationally resolved types of spectroscopy. Our rotational resolution exceeds that of any other rotational Raman spectroscopy.

Method	Resolution limit	Reference
Raman, Mercury lamp	12 GHz	[25]
Raman, single-mode laser	1.5 GHz	[25]
Raman, Fourier-transform IR	300 MHz	[25]
Raman, rotational coherence spectroscopy	>125 MHz	[25,26]
Coherent anti-Stokes Raman scattering	30 MHz	[25]
Rovibrational Fourier-transform Infrared	16 MHz	[26]
CRASY Raman spectra	1 MHz	[2]
Fourier-transform microwave spectroscopy	Single-kHz	[27]

required to resolve the *K*-structure. Our mirror size was not large enough for much longer scans because the alignment pulse must track the motion of the molecular beam. A 2.9 μs scan gave us 600 kHz resolution but the fitted rotational constants were worse than the ones presented here because the low sampling rate caused a worse signal-to-noise ratio. A new design for the laser beam focusing and a more efficient data collecting system could be required to succeed in this experiment. The benzene-d6 results showed again that our measurement is a robust tool to analyze symmetric top molecules and determined rotational constants with smaller uncertainties than literature values. The comparison between the rotational constants for benzene and benzene-d6 can be used to calculate the substitution structure of benzene.

4.4 Conclusion

In this section, we introduced the investigation of symmetric top molecules with high-resolution mass-CRASY. Our rotational spectra showed greatly enhanced resolution as compared to past Raman experiments, demonstrating the power of time-domain rotational Raman spectroscopy. Our new high-resolution method, with a real-time frequency monitoring system, has become an alternative technique for precise rotational measurements. To-date, our experiment is the only way to get pure rotational Raman spectra with high-resolution, down to the single-MHz regime.

The development of high-resolution rotational Raman spectroscopy advanced the analysis of symmetric top molecules. Through precise rotational constants, we can accurately determine molecular structures. The improvement of resolution can resolve hidden structure in a symmetric top rotational spectrum, such as the *K*-splitting. Further research with the symmetric top molecules will benefit from a planned enhancement of the data collecting system and from a revision of the optical mirror alignment. This will make it possible to resolve the *K*-structure in benzene and other symmetric top molecules.

4.5 References

1. Cloppenburg, B.; Manczak, K.; Prockl, H.; Schrötter, H.; Strey, G. Resolution of K-Splitting in the Rotation-Inversion Raman Spectrum of Ammonia NH3. *Zeitschrift für Naturforschung A*, **1979**, *34*(10), 1160-1163.

2. Lee, J. C.; Lee, D. E.; Schultz, T., High-resolution rotational Raman spectroscopy of benzene. *Physical Chemistry Chemical Physics* **2019,** *21* (6), 2857-2860.

3. Stoicheff, B., The Rotational Raman Spectrum of Benzene Vapor. *The Journal of Chemical Physics* **1953,** *21* (8), 1410-1411.

4. Jarzęba, W.; Matylitsky, V. V.; Weichert, A.; Riehn, C., Rotational coherence spectroscopy of benzene by femtosecond degenerate four-wave mixing. *Physical Chemistry Chemical Physics* **2002,** *4* (3), 451-454.

5. Matylitsky, V.; Jarzęba, W.; Riehn, C.; Brutschy, B., Femtosecond degenerate four-wave mixing study of benzene in the gas phase. *Journal of Raman Spectroscopy* **2002,** *33* (11-12), 877-883.

6. Riehn, C.; Weichert, A.; Brutschy, B., Probing benzene in a new way: high-resolution time-resolved rotational spectroscopy. *The Journal of Physical Chemistry A* **2001,** *105* (23), 5618-5621.

7. Stoicheff, B., High Resolution Raman Spectroscopy of Gases: I. Experimental Methods. *Canadian Journal of Physics* **1954,** *32* (5), 330-338.

8. Schröter, C.; Choi, C. M.; Schultz, T., CRASY: Correlated Rotational Alignment Spectroscopy Reveals Atomic Scrambling in Ionic States of Butadiene. *Journal of Physical Chemistry A* **2015,** *119* (8), 1309-1314.

9. Schröter, C.; Kosma, K.; Schultz, T., CRASY: mass-or electron-correlated rotational alignment spectroscopy. *Science* **2011,** *333* (6045), 1011-1015.

10. Anttila, R., Measurement of the Rotational Constant of the Benzene Molecule from the Structure of the $\nu_7 + \nu_{16}$ Near Infrared Vibration Band. *A: Phys. Sci.* **1968,** *23* (7), 1089-1089.

11. Jensen, H. B.; Brodersen, S., The totally symmetric rotation-vibrational Raman bands of benzene. *Journal of Raman Spectroscopy* **1979,** *8* (2), 103-110.

12. Lindenmayer, J.; Magg, U.; Jones, H., Diode laser spectroscopy of the ν4 band of benzene. *Journal of Molecular Spectroscopy* **1988,** *128* (1), 172-175.

13. Okruss, M.; Müller, R.; Hese, A., High-Resolution UV Laser Spectroscopy of Jet-Cooled Benzene Molecules: Complete Rotational Analysis of the $S_1 \leftarrow S_0 6_0^1$ (l=±1) Band. *Journal of molecular spectroscopy* **1999,** *193* (2), 293-305.

14. Cabana, A.; Bachand, J.; Giguere, J., The ν4 Vibration–Rotation Bands of C_6H_6 and C_6D_6: The Analysis of the Bands and the Determination of the Bond Lengths. *Canadian Journal of Physics* **1974,** *52* (20), 1949-1955.

15. Danti, A.; Lord, R., Rotational analysis and upper-stage transitions of parallel absorption bands in

benzene, sym-benzene-d3, benzene-d6 and pyridine. *Spectrochimica Acta* **1958,** *13* (3), 180-191.

16. Doi, A.; Kasahara, S.; Katô, H.; Baba, M., Sub-Doppler rotationally resolved spectroscopy of lower vibronic bands of benzene with Zeeman effects. *The Journal of chemical physics* **2004,** *120* (14), 6439-6448.

17. Domenech, J.; Junttila, M.; Pine, A., Molecular-beam spectrum of the 3.3-μm ν12 band of benzene. *Journal of Molecular Spectroscopy* **1991,** *149* (2), 391-398.

18. Junttila, M.; Domenech, J.; Fraser, G. T.; Pine, A., Molecular-beam optothermal spectroscopy of the 9.6-μm ν14 band of benzene. *Journal of Molecular Spectroscopy* **1991,** *147* (2), 513-520.

19. Kauppinen, J.; Jensen, P.; Brodersen, S., Determination of the B_0 constant of C_6H_6. *Journal of Molecular Spectroscopy* **1980,** *83* (1), 161-174.

20. Pliva, J.; Pine, A., The spectrum of benzene in the 3-μm region: The ν12 fundamental band. *Journal of Molecular Spectroscopy* **1982,** *93* (1), 209-236.

21. Hollenstein, H.; Piccirillo, S.; Quack, M.; Snels, M., High-resolution infrared spectrum and analysis of the ν 11, A2u (B2) fundamental band of $^{12}C_6H_6$ and $^{13}C^{12}C_5H_6$. *Molecular physics* **1990,** *71* (4), 759-768.

22. Plíva, J.; Valentin, A.; Chazelas, J.; Henry, L., High-resolution Fourier transform study of the ν14 band of benzene-d6. *Journal of Molecular Spectroscopy* **1989,** *134* (1), 220-226.

23. Kunishige, S.; Katori, T.; Baba, M.; Nakajima, M.; Endo, Y., Spectroscopic study on deuterated benzenes. I. Microwave spectra and molecular structure in the ground state. *The Journal of chemical physics* **2015,** *143* (24), 244302.

24. Frey, H.M. In Handbook of High-resolution Spectroscopy; Quack, M.; Merkt, F., Eds.; John Wiley & Sons, Ltd: Chichester, UK, **2011**; Vol. 2; Chapter High-resolution Rotational Raman Coherence Spectroscopy with Femtosecond Pulses, pp. 1237.

25. Weber, A. In *Handbook of High-resolution Spectroscopy*; Quack, M.; Merkt, F., Eds.; John Wiley & Sons, Ltd: Chichester, UK, **2011**; Vol. 2; Chapter High-resolution Raman Spectroscopy of Gases, pp. 1153.

26. Albert, S.; Keppler, K. A.; Quack M. In Handbook of High-resolution Spectroscopy; Quack, M.; Merkt, F., Eds.; John Wiley & Sons, Ltd: Chichester, UK, **2011**; Vol. 2; Chapter High-resolution Fourier Transform Infrared Spectroscopy, pp. 1153.

27. Weber, A. In *Handbook of High-resolution Spectroscopy*; Quack, M.; Merkt, F., Eds.; John Wiley & Sons, Ltd: Chichester, UK, **2011**; Vol. 2; Chapter New Techniques in Microwave Spectroscopy, pp. 801.

28. Demtroder, W., In *Handbook of High-resolution Spectroscopy*, Quack M.; Merkt, F., Eds.; John Wiley & Sons, Ltd, **2011**, vol. 3, pp. 1759–1779.

Chapter V. Asymmetric Top Molecules

5.1 Introduction

Unlike linear molecules and symmetric top molecules, asymmetric top molecules have a complicated rotational spectrum. So, the early stage of the CRASY focused on simple molecules like CS_2. In 2015, CRASY measured the butadiene rotational Raman spectrum with a 2 ns scan time delay and 500 MHz resolution. This experiment was the first study of an asymmetric top molecule by CRASY.[1]

In the past, the only way to get a high-resolution rotational spectrum of asymmetric top molecules was high-resolution FTMW. Previous rotational-Raman spectroscopy lacked the resolution to resolve complex spectra. Our works now gives us a single-MHz rotational spectra and improved accuracy, as compared to the old Raman techniques and the characterization of asymmetric top spectra should be feasible.[2]

CRASY can produce multidimensional spectroscopic information and resolve spectra in heterogeneous samples. Mass-correlated rotational spectra distinguished multiple CS_2 isotopologues with a single measurement. Likewise, mass-CRASY should be able to distinguish isotopologue structures like cytosine tautomers. The spectroscopic range of CRASY is broader than that of current microwave spectroscopy, which might help in such efforts. The rotational Raman spectrum from CRASY measurements typically produces data with 500 GHz, spectral range. Within this range, we can observe the full rotational spectrum of asymmetric top molecules.

In this chapter, I present results for pyridine, pyrazine, furan, thiophene, and butadiene, obtained with mass-correlated rotational Raman spectroscopy. Still, our resolving power is weaker than high-resolution FTMW. However, high-resolution CRASY can also observe non-dipolar molecules like pyrazine, which are not observed with FTMW. That is why our high-resolution Raman spectroscopy can be a complementary tool to high-resolution microwave spectroscopy for the analysis of asymmetric tops.

5.2 Experiment and Results

Asymmetric top molecules have three different rotational constants associated with their principal axes ($I_A \neq I_B \neq I_C$). To fully analyze an asymmetric top molecule, all rotational constants, A, B, C should be determined. As compared to asymmetric tops, the density of rotational states and the resulting number of spectroscopic lines increases a lot. In the rigid rotor approximation, the term energies are described as:

$$F(J) = A \cdot J_a^2 + B \cdot J_b^2 + C \cdot J_c^2$$

As I already mentioned in the symmetric top section, the asymmetry parameter can be used to classify the asymmetric top molecule. If κ is close to - 1, the structure is a near-prolate top and for κ close to +1, the molecule is a near-oblate top. This factor helps to choose the most intuitive reduction (*A* or *S*) and representation (I_r, II_r, III_r) of the molecule following Watson's reduced asymmetric top Hamiltonian for an non-rigid Hamiltonian. For the prolate top, we commonly use I_r and for the oblate top, we typically use III_r. When κ is at an intermediate value between – 1 and + 1, the molecule is often characterized in II_r.

5.2.1 Pyridine

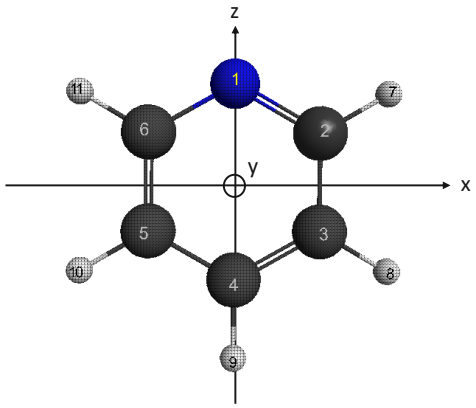

Figure 5.1. The molecular structure of pyridine and its principal axes.

Pyridine (C_5H_5N) is a six-membered ring heteroatomic molecule. Figure 5.1 shows an ab-initio calculated structure of pyridine. It has C2v symmetry and, following the lead of Ye et al.,[3] we use the III_r representation with Watson's A-reduced Hamiltonian for this near oblate top. Many biomolecules contain aromatic rings with nitrogen atoms and pyridine is a representative for a biorelevant molecule. Because of its relevance, pyridine was thoroughly studied with rotational, IR, Raman, and electronic spectroscopy. Past studies of the pyridine rotational spectrum were mainly performed with microwave spectroscopy and are discussed in further detail below. Our data present the first rotational Raman spectrum of pyridine, and our measurement gave us the first CRASY data for such a biologically relevant and relatively low vapor pressure molecule.

In 1953, Bak and Rastrup-Andersen published the first microwave spectroscopy results for pyridine in the frequency regime of 18 to 26 GHz.[4] Another spectroscopic analysis in the 22 to 28 GHz range was performed by McCulloh and Pollnow and disagreed with the initial band assignment of Bak et al.[5] Bak et al. revised the band assignment and improved the accuracy of rotational constants using Stark effect measurements at 20.4 GHz.[6] Sørensen resolved the ^{14}N quadrupole hyperfine structure and

measured distortion constants in the 8 to 27 GHz range.[7] In 1986, Heineking et al. measured a high-resolution spectrum, resolving the ^{14}N hyperfine structure, in the 5 to 26 GHz regime.[8, 9] Ye et al. characterized the ground and five vibrationally excited states in the 75 to 110 and 260 to 370 GHz frequency bands.[3]

Becucci and Melandri characterized pyridine noble gas cluster structures by Fourier-transform microwave spectroscopy.[10] Their research did not yield information about the pyridine-dimer. We speculate that the pyridine dimer is symmetric and lacks the dipole moment required for FTMW. There are several theoretical studies of the pyridine dimer, attempting to characterize relevant non-covalent π-electron interactions.

Piacenza and Grimme compared 7 pyridine dimer structures with DFT, MP2, and spin-corrected (SCS) MP2 calculations and described the most stable structures as H-bonded and T-shaped pyridine.[10] The most stable stacked structures were non-symmetric with a 160° angle between the axes through the nitrogen atoms and a lateral displacement of the rings into a staggered configuration. According to their simulation, the most stable pyridine-dimer structure should be accessible to FTMW spectroscopic studies.

Hohenstein and Sherrill compared the performance of high-level ab initio methods for the characterization of the pyridine dimer binding potential energy curves, using CCSD(T) calculations extrapolated to the complete basis set limit as reference method. They identified several cluster structures with very similar binding energies.[12] Zhang et al. enhanced the basis with bond functions to obtain interaction energies in stacked and T-shaped dimers.[13] Sieranski explored the binding potential energy surface of the dimer with dispersion-corrected DFT calculations.[14] Currently, there is no experimental data to validate the dimer calculations.

Experiment

In this experiment, we attempted to observe the rotational Raman spectrum for pyridine, as well as symmetric and non-dipolar dimers of pyridine. The signal contrast was insufficient to resolve dimer species. We can only present the rotational Raman spectrum of pyridine monomer and discuss ab-initio structures for the dimer.

It was challenging to get sufficient signal of pyridine because of its low vapor pressure (2.1 kPa), which is much lower than that of molecules that were measured earlier. At that time, our multichannel-plate detector had aged considerably, and we tuned the detector voltage from 2.3 kV to 3 kV to get decent signal counts. Pyridine was ionized with either 266 nm or 200 nm laser pulses. Although the ionization signal with 266 nm is higher than that with 200 nm, we obtained better results with 200 nm because the 266 nm beam induced too much fragmentation of pyridine.

The first measurements with pyridine used 5 bar or 10 bar backing pressure to generate a cold

molecular beam. This condition was our default for preceding experiments. However, with this condition, the measured rotational spectra showed bad S/N ratio. We decreased the backing pressure to 1~2 bar, and thereby reduced the amount of pyridine dimer signal and signal at mass 80 u. This increased the absolute signal for pyridine and improved the S/N ratio.

Figure 5.2 shows mass spectra obtained with 1 bar and 10 bar helium backing pressure. The ion signals revealed pyridine parent ions (79 u), dimers (158 u), and fragments (52 u, 39 u, 26 u). This measurement also found the residual CS_2 signal in the 76 u channel. In the 10 bar mass spectra, the signal in mass channels 158 u and 79 u was much higher than in the 1 bar spectra. The mass 80 u signal with 10 bar backing pressure was also of much higher intensity than with 1 bar. Considering the natural abundance of heavy atoms, that huge signal cannot be explained by the presence of heavy pyridine isotopologues. The correlation between the presence of a large amount of dimer signal and a large signal at mass 80 u indicated that the 80 u signal is formed by dimer fragmentation.

We analyzed the rotational spectra for the pyridine mass channel in both data sets. The accuracy of rotational constants fitted for pyridine at 1 bar was about 10 times better than that obtained at 10 bar, with otherwise identical conditions. Possible fragmentation products of the dimer could appear as protonated monomer (80 u) but also as pyridine cation, superimposed on the parent ion signal in the

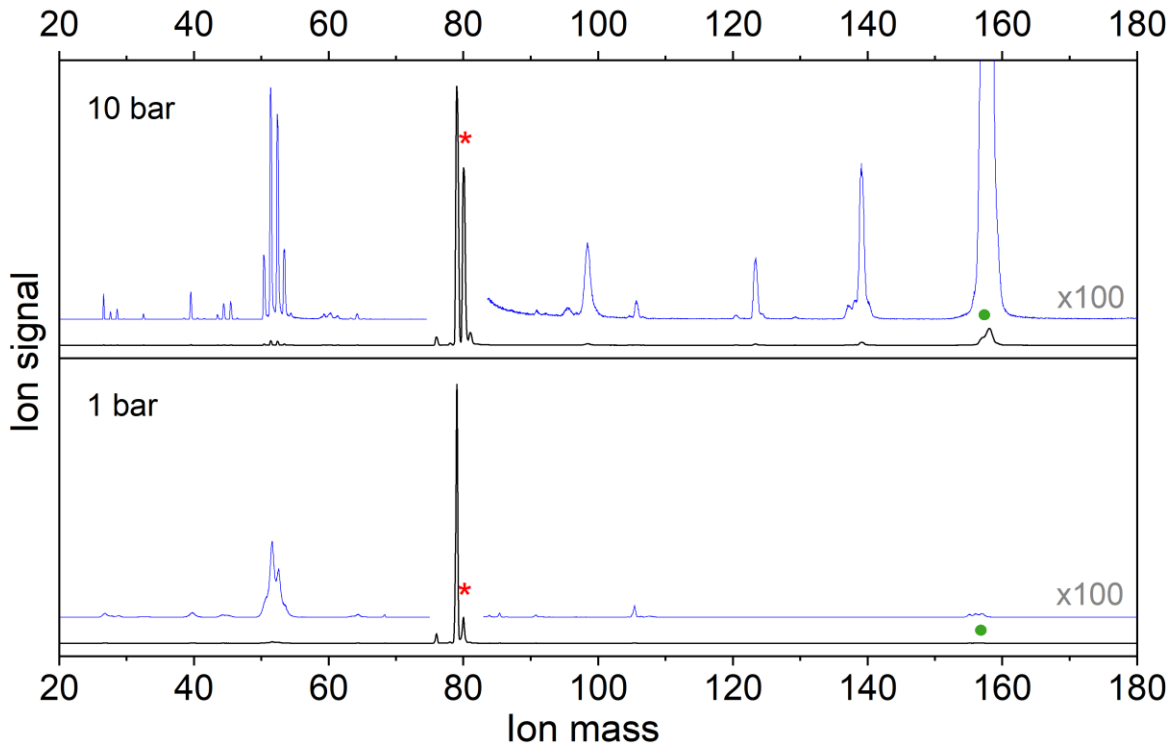

Figure 5.2. Comparison of mass spectra with different backing pressure (1 bar vs 10 bar). At 10 bar, clustering is stronger and the signal intensity of the pyridine dimer (158 u) is much higher. The peak at 80 u is also higher than in the lower pressure spectrum. We guess that the molecule at 80 u came from fragmentation of the pyridine dimer.

mass channel 79 u. If this is the case, then the rotational wave packet for 79 u is the sum of that expected for the monomer and the dimer. This clearly would reduce the quality of the monomer rotational spectrum. We guess that this is the reason for the bad S/N ratio in the 10 bar data.

In Figure 5.3, I show data for pyridine with 1 bar helium backing pressure, measured over three different time delays of 20 ns, 100 ns, and 500 ns.[14] In all measurements, the step-size was 1 ps. Only the 20 ns scan was a continuous scan and the other scans used sparse sampling with 20,000 mass spectra acquired for random positions along the delay axis. All measurements required the same measurement time but the obtained resolution increased from 50 MHz in the continuous to 10 MHz and 2 MHz in the sparse scans.

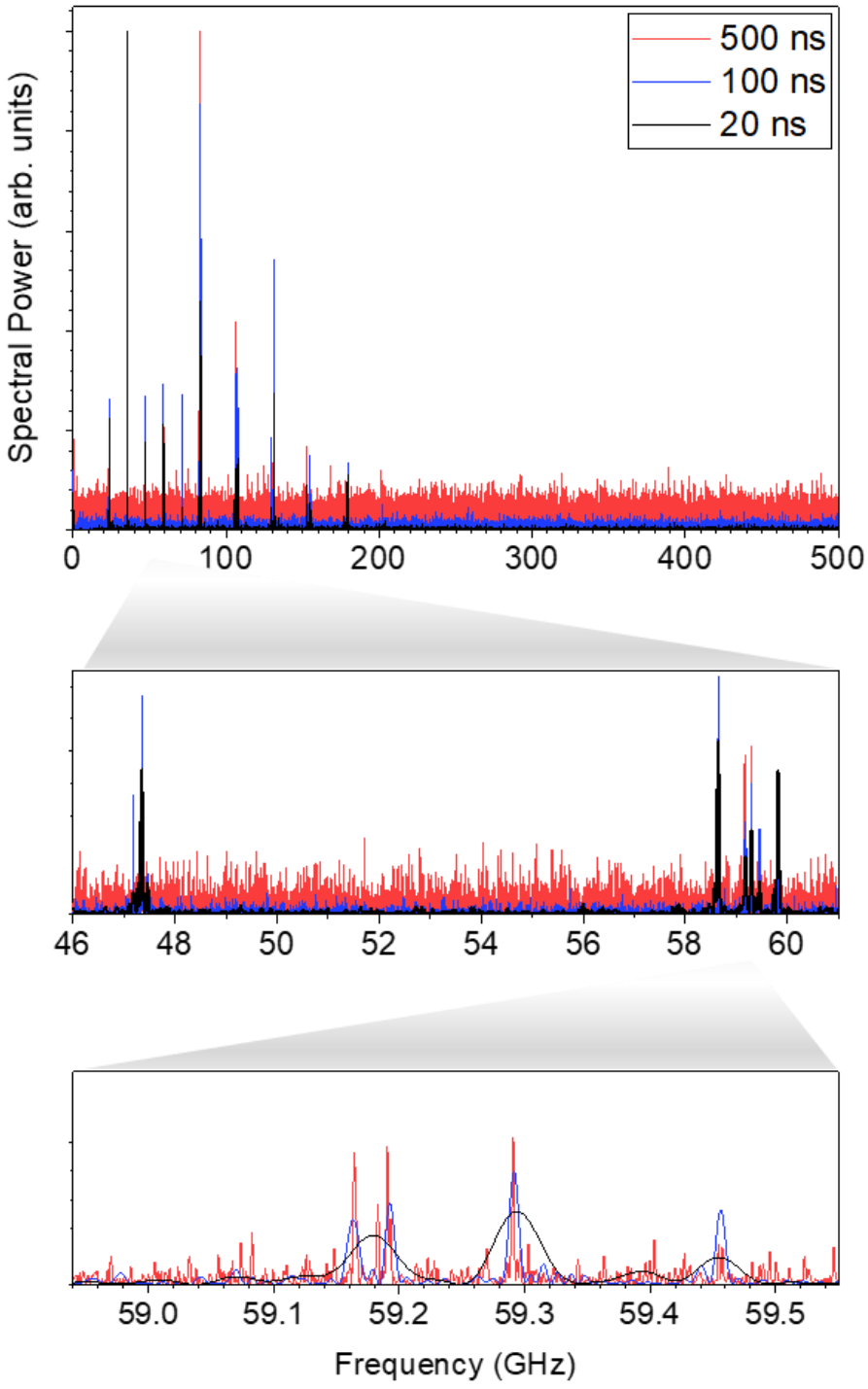

Figure 5.3. Rotational Raman spectra for mass channel 79 u from 20 ns, 100 ns, and 500 ns scans. The ordinates are normalized. The enlarged spectra show the improvement of resolution with the increase of the scan range. However, a decrease in signal-to-noise ratio is the trade-off for the sparse scanning.

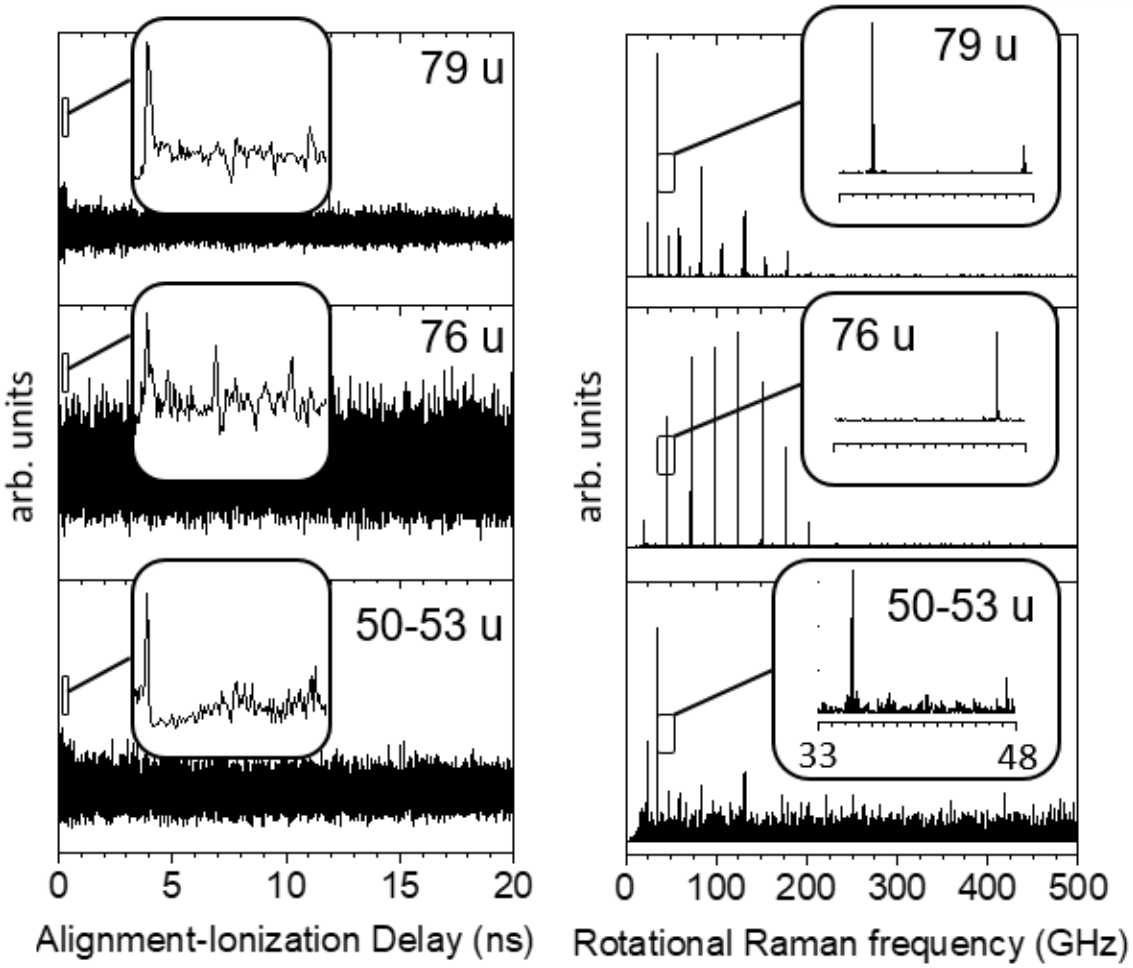

Figure 5.4. Results from the 20 ns linear scan. Left. Traces of the mass channel 79 u (Pyridine), 76 u (CS_2), and 50 – 53 u (Fragments from pyridine). Enlarged insets show a 100 ps range of the trace and show the temporal laser pulse overlap and some revival structure in each trace. Right. Rotational spectra are obtained after Fourier transformation of the traces.

Pyridine is an asymmetric top molecule, so the time-domain revival signal is not as clear as in linear and symmetric top molecules. However, as seen in Figure 5.4, a 20 ns continuous scan still showed some revival signal in the early part of the time trace. In sparsely sampled data, it was not possible to see revival signals.

In the 20 ns linear scan, our mass-correlated rotational Raman spectrum resolved rotational lines also in the fragment mass channels. Comparison between the parent ion (79 u) and fragment ion (53 u) FFT spectra showed that both had identical frequency peaks. This proves that this fragment came from the pyridine parent ion. At mass channel 76 u, CS_2 was observed and we observed a nice revival signal and rotational spectrum.[1, 15]

Fitted rotational constants for the pyridine parent ion mass channel are summarized in Table 5.1. The uncertainties of fitted rotational constants decreased with the increase of resolution in the sparse scans. This illustrates the relationship between longer time delay scans and higher measurement accuracy. We

assigned lines in all three spectra with the PGOPHER program and fitted rotational constants. The 20 ns and 100 ns scans did not have enough resolution to fit the distortion constant D_J, so we fixed D_J to the literature value. However, the 500 ns scan can determine the distortion constant D_J. The enlarged traces in Figure 5.4 show that the longer time delay scan resolve more lines and the assignment of these lines directly improve the accuracy of the fitted rotational constants. All values are in reasonable agreement with literature results based on Fourier-Transform microwave spectroscopy (Table 5.1.). Note: The pyridine results were calibrated using the CS2 measurements in the same data set. This was necessary because of a connection between frequency counter and GPS clock.

Table 5.1. Fitted pyridine spectroscopic constants (in MHz) and comparison results from literature. Square brackets indicate that the parameter was fixed to corresponding literature values.

	20 ns	*100 ns*	*500 ns*	McCulloh	Sorensen	Enyi Ye
A	6039.32(17)	6039.240(29)	6039.185(23)	6037.91	6039.290	6039.24428(28)
B	5804.80(19)	5804.879(32)	5804.903(30)	5803.55	5804.947	5804.91381(26)
C	2980(14)	2959.0(2.7)	2961.3(1.6)	2958.65	2959.230	2959.21006(24)
D_J	[0.00138966]	[0.00138966]	1.44(33)e-3			0.00138966(21)
D_K	[0.0012218]	[0.0012218]	[0.0012218]			0.00122178(30)
D_{JK}	[-0.002498]	[-0.002498]	[-0.002498]			-0.00249843(38)
δ_K	[-0.002074]	[-0.002074]	[-0.002074]			-0.0020740(27)
δ_J	[-7.04e-6]	[-7.04e-6]	[-7.04e-6]			-7.043(84)e-6
J_{Max}	6	7	5	19	43	
$K_{c,max}$	2	5	3		8	
# lines	36	40	26	35	52	1185
κ^f	0.8467	0.8478	0.8478	0.8478	0.8478	0.8478

Ab-initio Calculations

To explain the presence of a large signal in mass channel 80 u, we performed ab-initio calculations for pyridine and its dimer. All ab-initio calculations were computed with the OCRA quantum chemistry package.[16,17] We hypothesized that the 80 u signal stems from protonated monomer and is due to asymmetric dimer fragmentation. We used the dispersion corrected density functional method PBEh-3c, which is described in the literature as a suitable method to describe intermolecular dispersive interactions, free of basis-set superposition errors (BSSE).[18]

We also performed second-order Moller-Plesset perturbation theory calculations with aug-cc-pVTZ basis set. The PBEh-3c calculation gave us reasonable ionization energies as compared to the literature values, but initial MP2 values deviated significantly. Energies for adiabatic ionization potentials and vertical ionization potentials at the optimized geometries are given in Table. 5.2.

The hydrogen bond lengths for the hydrogen-bonded (H-bonded) dimer slightly differ for the two methods, but both describe a near symmetric H-bonded structure. The PBEh-3c calculation gave a

longer bond length of 2.52 Å as compared to an MP2 result of 2.40 Å. The dissociation energy of the dimer was 19.1 kJ/mol at the PBEh-3c and 21.2 kJ/mol at the MP2 level. In the case of PBEh-3c, the H-bonded structure of the dimer cation resembled that of the neutral, but with significantly shorter H-bonds of 1.94 Å. The structure of this dimer cation was unstable at the MP2 level and converged to a proton transferred structure with perpendicular pyridine ring orientations. The latter structure was also the lowest energy structure at the PBEh-3c level.

Dissociation of the dimer cation occurs into (1) the radical cation and a neutral, or (2) the closed-shell protonated cation, and a neutral ortho-, meta-, or para-pyridyl radical. We calculated dissociation energies of (1) 163 kJ/mol and (2) 99 kJ/mol, 126 kJ/mol, and 120 kJ/mol for the ortho-, meta-, or para-pyridyl fragmentation channels. As opposed to PBEh-3c values, MP2 dissociation energies are not free of BSSE errors and are therefore not given here. Based on our calculated dissociation energies, we can assume that the asymmetric fragmentation and the formation of protonated monomers is the expected fragmentation channel for the cationic dimer.

The calculations explained the large 80 u mass signal as a product from the asymmetric fragmentation of the cationic pyridine dimer. They did not directly explain why we could not resolve the corresponding rotational Raman spectrum of pyridine dimer in the protonated monomers mass channel, even though the signal strength of the protonated pyridine was strong. The existence of multiple stable pyridine dimer structures offers a possible explanation: If many dimer structures co-exist, then the signal for each dimer species may be too small to produce a recognizable spectrum.

Table 5.2. Calculated ionization potentials and binding energies for pyridine (Py) and the H-bonded pyridine dimer (Py_2). All values in eV.

	PBEh-3c	MP2-accpVTZ
IP_{vert}(Py)	9.67	9.91
IP_{ad}(Py)	9.18	9.62
IP_{vert} (Py_2)	9.22	9.39
IP_{ad} (Py_2)	7.68	8.05
$Py_2 \rightarrow Py, Py$	0.198	
$Py_2^{\bullet+} \rightarrow Py^{\bullet+} + Py$	1.70	
$Py_2^{\bullet+} \rightarrow PH^+ + o\text{-pyridyl}^\bullet$	1.03	
$Py_2^{\bullet+} \rightarrow PH^+ + m\text{-pyridyl}^\bullet$	1.31	
$Py_2^{\bullet+} \rightarrow PH^+ + p\text{-pyridyl}^\bullet$	1.24	

5.2.2 Pyrazine

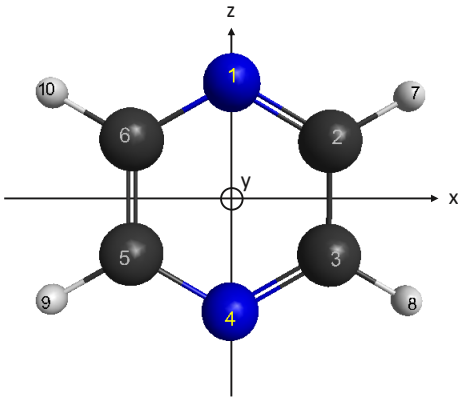

Figure 5.5. The molecular structure of pyrazine.

Pyrazine ($C_4H_4N_2$) is a heterocyclic aromatic molecule and its structure is shown in Figure 5.5. Pyrazine is a symmetric molecule with the symmetry point group, D_{2h}. Pyrazine has no dipole moment and it cannot be measured with microwave spectroscopy. The rotational spectrum of pyrazine was previously discussed in the literature. In 1957, Lord et al. first presented infra-red and Raman spectroscopy of pyrazine, pyrimidine, and pyridazine.[19] Califano et al. measured infrared spectra for the isotopologues pyridine-D_0, cis pyrazine-D_2 and pyrazine-D_4 between 400-4000 cm^{-1}.[20] Billes et al. measured a vibrational spectrum of pyrazine and performed ab initio quantum chemical calculations in 1998.[21] Breda et al. measured vibrational spectra of pyrazine in solid argon.[22] In 2009, Schmitt et al presented a FTIR spectrum of pyrazine in the gas phase and calculated rotational constants with MP2.[23]

There was also an experiment to observe the nonadiabatic alignment of pyrazine. Masaaki et al. analyzed time-dependent molecular alignment by observing photoelectron angular distribution (PAD) data.[24] They observed the first full revival signal of pyrazine at 82 ps using ultrashort laser pulses. However, they did not obtain a rotational spectrum of pyrazine.

The vapor pressure of pyrazine is 1.4 kPa at room temperature, and this is the first solid-state molecule that we investigated with CRASY. Pyrazine was hard to ionize with a 200 nm beam because the UV absorption dramatically decreases below 250 nm wavelength. When we consider the NIST UV/Visible spectrum,[25] the best wavelength for excitation is 250 ~ 270 nm, so we changed to a 266 nm beamline to increase the ionization signal. This wavelength is the third harmonic of the 800 nm Ti: Sapphire laser and we generated 5 μJ of 266 nm light in BBO crystals. The 800 nm, 1 ps alignment pulse energy was 100 μJ in this experiment. The experimental results from a 20 ns continuous scan with 1 ps step-size is shown in Figure 5.6.

Figure 5.7 compares the mass spectra obtained with 200 nm and 266 nm photoionization. Pyrazine

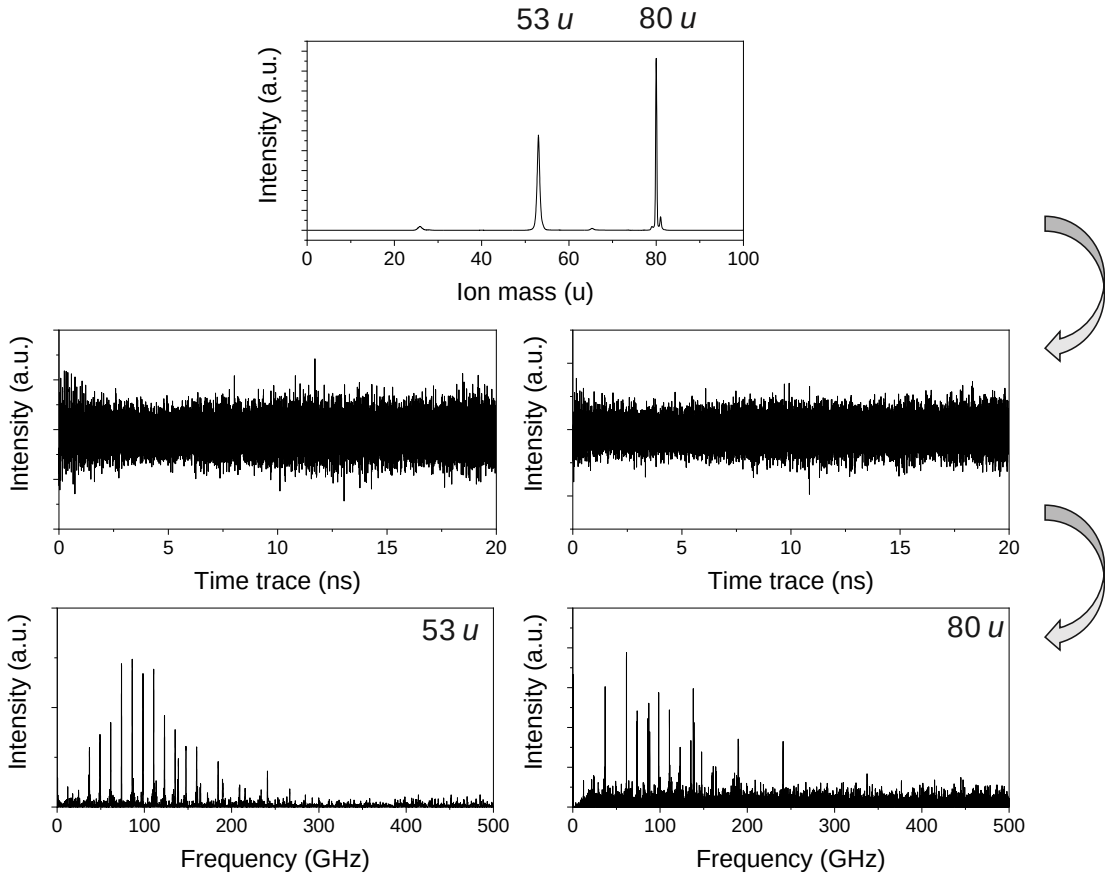

Figure 5.6. CRASY data for pyrazine. Top. The TOF-mass spectrum of pyrazine. Middle. The time trace of mass channels 53 u and 80 u. Bottom. The rotational spectrum after Fourier-transform of the traces.

appears at mass 80 u and heavy carbon isotopologues appear with expected amplitude at mass 81 u. Signal for CS_2 (76 u) is observed with 200 nm ionization but not with 266 nm ionization. Strong fragmentation signal, with a dominant fragment at 53 u, is observed with 266 nm photoionization but not with 200 nm ionization. Compared to other investigated molecules, pyrazine showed a much larger fragmentation signal when ionized with 266 nm pulses. The adiabatic ionization potential of pyrazine is 9.3 eV, just barely below the two photon energy of 266 nm (9.32 eV). We therefore assume that above-threshold, 3-photon ionization with the 266 nm beam generated the strong fragment signals. With the 200 nm beam, ionization occurred with a two-photon processes and we observed significantly less fragmentation.

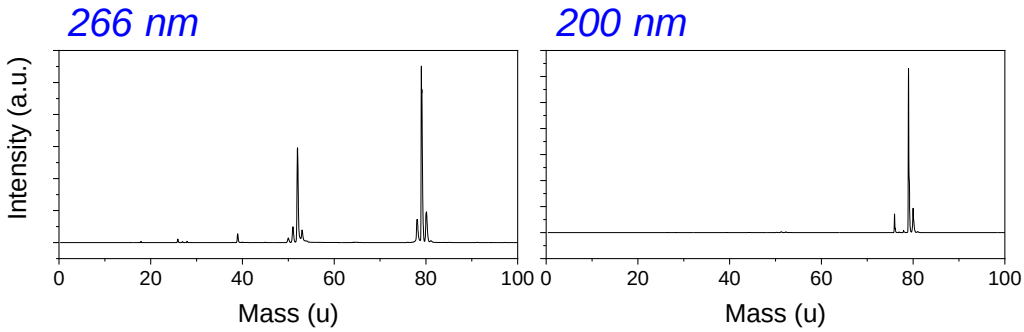

Figure 5.7. The mass spectrum of pyridine for different ionization wavelengths. Ionization with 266 nm generates more fragments.

In the pyrazine measurement, the strongest fragmentation channel showed nicer revival contrast than the parent ion channel, as shown in Figure 5.8. When we analyzed the corresponding rotational spectra, the rotational constants from the fragments channel gave us smaller uncertainties. In the 20 ns linear scan, I was able to assign more lines in the fragment mass channel.

Figure 5.9 shows the rotational spectra of pyrazine from a 100 ns sparse scan. The 100 ns scan of

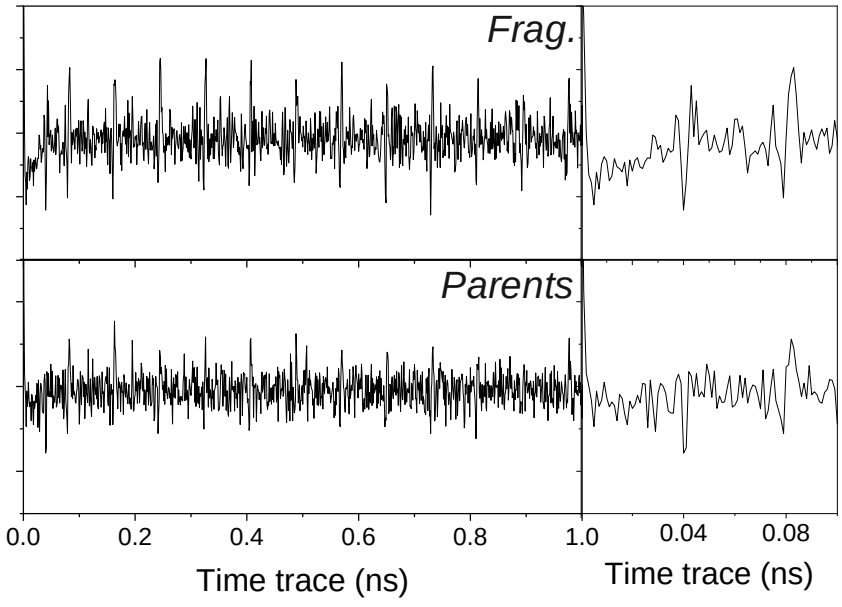

Figure 5.8. The comparison between time traces for pyrazine parent and fragment ions. The revival signal in the fragmentation channel is clearer than in the parent ion. Enlarged trace shows clearly the position of revival signal at 82 ps.

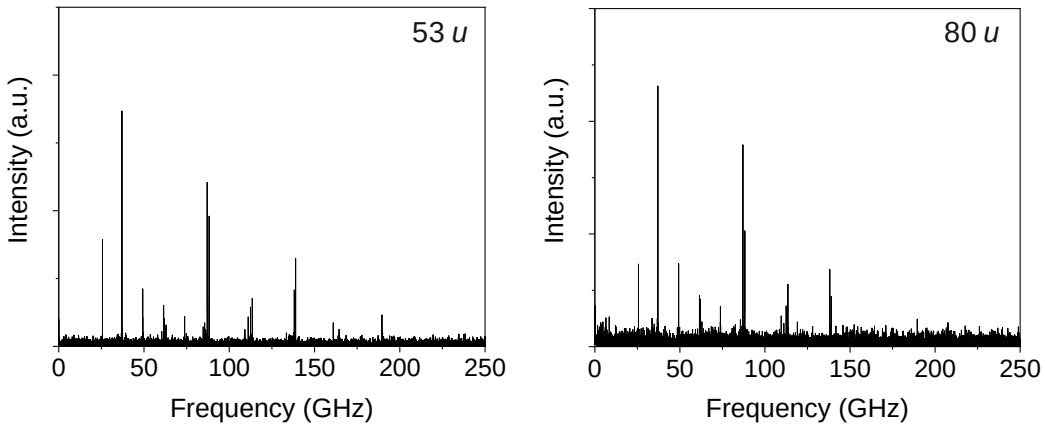

Figure 5.9. The rotational Raman spectrum for pyrazine with 100 ns, 20 % sparse scanning. At the 53 u fragmentation channel, the signal to noise ratio is better than the main isotopologue channel.

pyrazine gave us more accurate rotational constants than our 20 ns scan data and the accuracies were similar for the fragmentation channel and the main isotopologue channel. Table 5.3 lists the number of assigned lines in parent and fragment channel and compares fitted rotational constants with literature values. Comparing to Schmitt's results,[23] our constant agreed well results from their FTIR measurement but are slightly different from their MP2 calculation. Our measurement provided rotational constants with 10 times better accuracy than the best literature values.

Table 5.3. Fitted rotational constants (in MHz) for pyrazine from CRASY experiments and the literature. CRASY results were obtained from a 20 ns linear scan and a 100 ns sparse scan.

	20 ns		*100 ns*		*M. Schmitt*	
	53 u	*80 u*	*53 u*	*80 u*	*FTIR*	*MP2*
A	6410.410(89)	6411.07(17)	6410.435(17)	6410.382(24)	6410.40(36)	6414.389
B	5915.41(27)	5912.00(83)	5915.335(30)	5915.325(61)	5915.15(39)	5851.604
C	3075.817(59)	3076.012(74)	3075.796(28)	3075.895(27)	3076.20(33)	3060.042
D_J	-	-	[0.00078]	[0.00078]	0.0015(21)	0.00078
D_K	-	-	[0.00150]	[0.00150]	0.0006(51)	0.00150
D_{JK}	-	-	[-0.00075]	[-0.00075]	-0.0013(6)	-0.00075
δ_K	-	-	[0.00051]	[0.00051]	0.0005(19)	0.00051
δ_J	-	-	[0.00033]	[0.00033]	0.0002(12)	0.00033
lines			27	17	17	

5.2.3 Furan

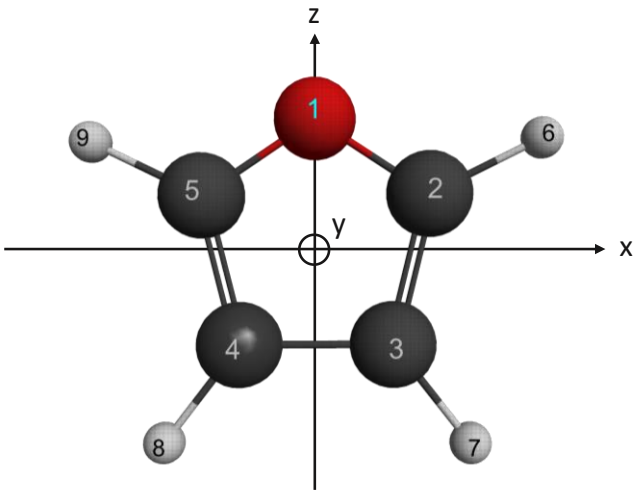

Figure 5.10. The structure of furan and the orientation of its principal axes.

Furan (C_4H_4O) is a heterocyclic aromatic molecule that includes an oxygen atom. The lone pair of electrons on the oxygen atom is coupled to the aromatic system. Furan is a near-oblate top rotor with the molecular symmetry C_{2v}. Figure 5.10 illustrates the molecular structure of furan. The nuclear spin statics of furan is 10 for even K_a (ee, eo) and 6 for odd K_c (oo, oe) states.

Previous rotational spectra of furan were measured with microwave spectroscopy. Bak et al. identified all bond lengths and bond angles of furan by investigating heavy isotope enriched furan samples containing ^{13}C and ^{18}O in 1962.[26] Mata et al. first performed microwave spectroscopic analysis of furan with consideration of centrifugal distortion effects.[27] Wlodarczak et al. assigned 212 lines for the main isotopologue and observed transitions up to Jmax = 54.[28] In 1989, Liescheski identified the furan structure with various analytic tools: Gas-phase electron diffraction, rotational spectroscopy, and liquid crystal NMR spectroscopy.[29] High-resolution IR characterized the rotational structure in several frequency bands. In 1965, the first pure rotational Raman spectrum of furan was obtained.[30] There was no further investigation of the rotational Raman spectrum. The work presented here represents the first furan data from high-resolution rotational Raman spectroscopy.

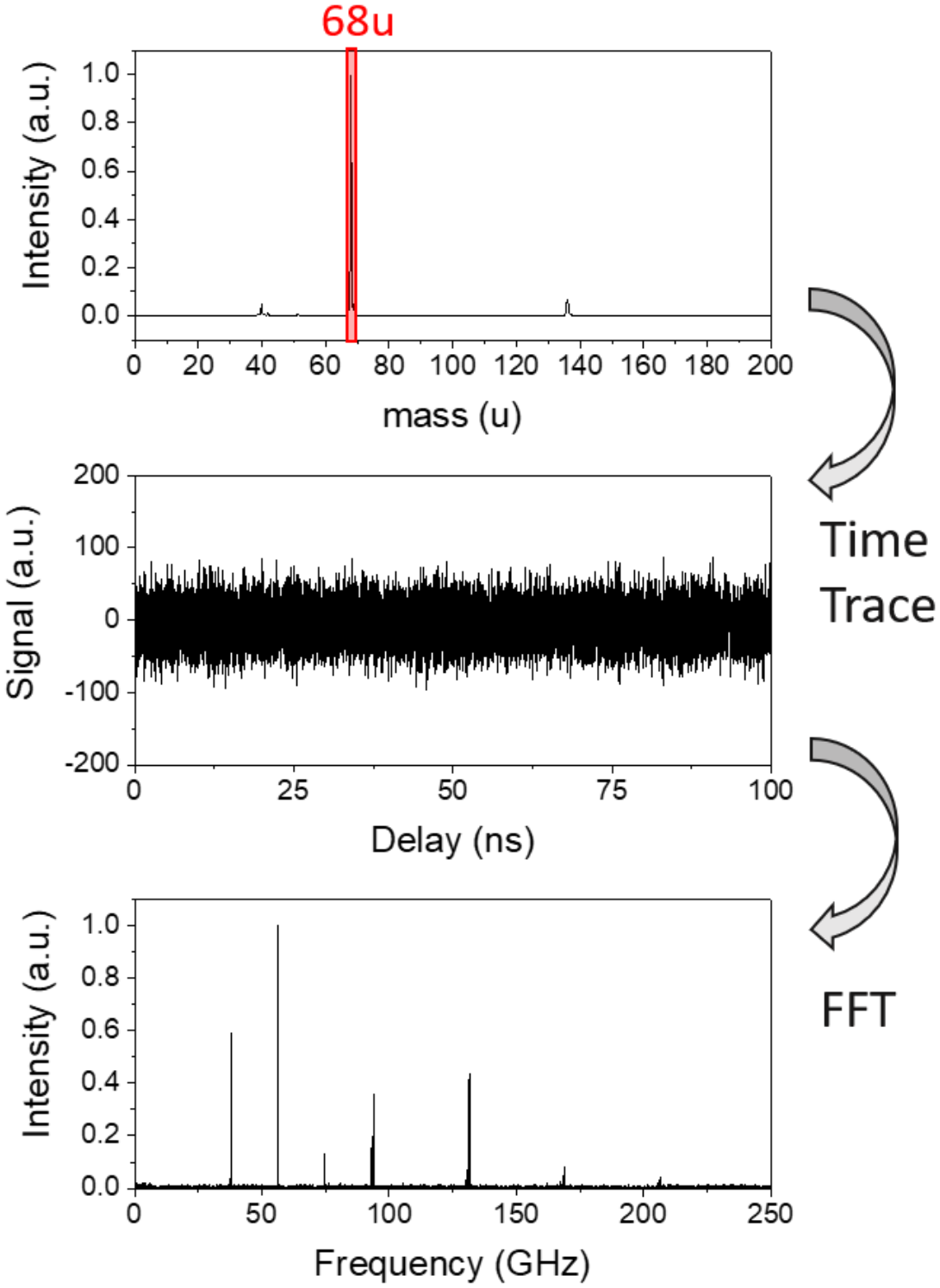

Figure 5.11. CRASY data analysis for furan. Top. Mass spectrum of furan. The furan mass signal at mass 68 u is marked in red. Middle. Time trace for the mass channel 68 u, measured over a time delay of 100 ns with 20 % sparse sampling. Bottom. The rotational spectrum of furan is obtained by Fourier transformation of the time trace.

The measurement conditions for furan used 1~2 bar helium backing pressure and the vapor pressure of furan is 65.7 kPa at room temperature. With this large vapor pressure, it was easy to find the signal with 200 nm, 50 fs ionization laser pulses. We scanned a time delay of 20 ns in a continuous scan and of 100 ns in a sparse scan, both based on 20,000 measured mass spectra. Due to a limited signal to noise ratio, heavy ^{13}C isotopologues were only analyzed for the 20 ns linear scan measurement.

Figure 5.11 shows the mass spectrum, delay trace, and Fourier transform spectrum for furan. The mass spectrum showed a strong signal for furan at mass 68 u and a small fragment signal at 40 u. A dimer signal was observed at 136 u. The time trace for the 68 u signal showed very regular modulation. The Fourier-transform spectrum showed only a few lines, indicating a quite cold molecular beam. In the fit of our spectrum with PGOPHER, we used distortion constants from the literature because our spectrum only contained transitions from low *J*-states and the number of spectral lines was not enough to resolve all distortion constants. Figure 5.12 shows that our spectrum was well reproduced by the fit. The fitted rotational constants and literature values are summarized in Table 5.5. Heavy isotopologue transitions were assigned and fitted in the spectrum correlated to the 69 u parent ion signal in the lower resolution 20 ns scan. The resolution of our spectrum was better than 10 MHz and the accuracy of the fitted rotational constants is in the kHz region. As shown in Figure 5.13, fragment mass channels 40 u and 42

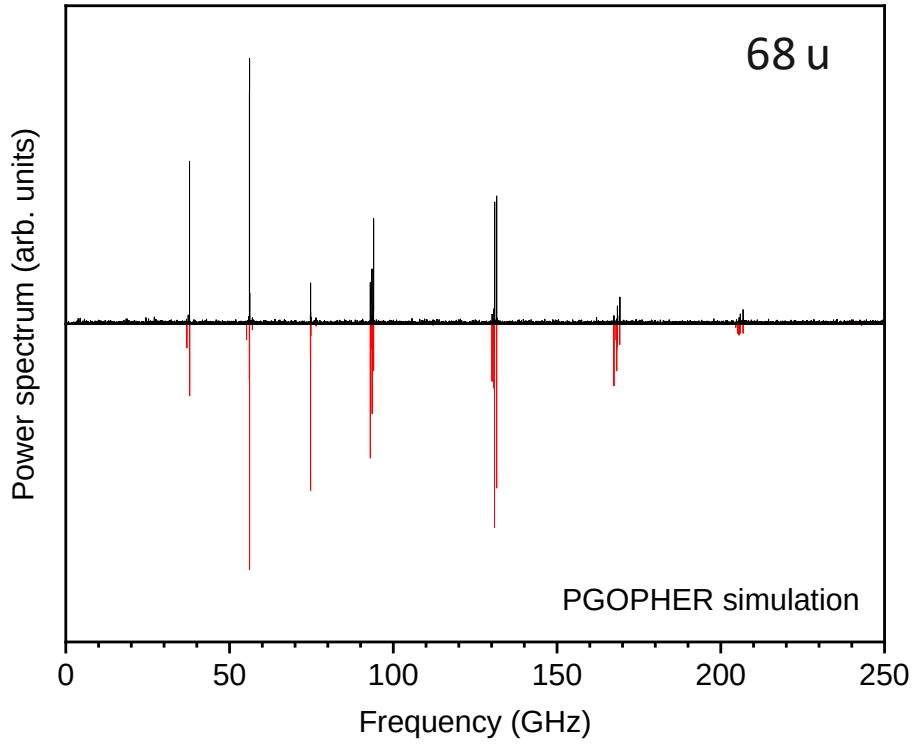

Figure 5.12. Comparison between measured spectrum and fit for furan. The fit was computed with PGOPHER and our spectrum was well reproduced by the fit.

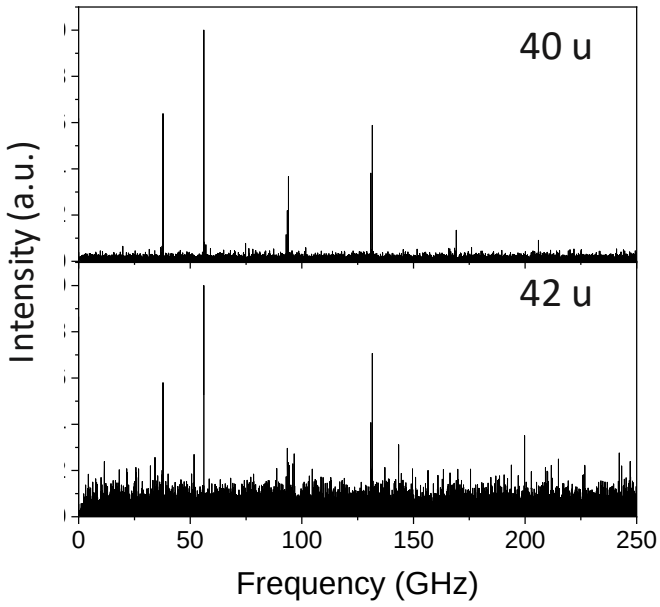

Figure 5.13. The spectrum of furan fragments at mass 42 u and 40 u. Both spectra are identical to the furan parent ion spectrum.

u showed the same spectrum as the furan parent, confirming that these species are formed by fragmentation of furan.

Table 5.4. Fitted rotational constants (MHz) for furan from our measurement and from the literature. The centrifugal distortion constants are given in kHz. Fixed values are expressed with square brackets.

	Furan		2-^{13}C-Furan		3-^{13}C-Furan	
	CRASY	*Wlodarczak*	*CRASY*	*Bak*	*CRASY*	*Bak*
A	9447.06(31)	9447.12360(32)	9295.5(1.1)	9295.41	9405.5(1.5)	9403.73
B	9246.60(40)	9246.74437(31)	9177.0(1.5)	9178.23	9039.8(3.3)	9043.68
C	4683(80)	4670.82458(40)	[4616.25]	4616.25	[4608.15]	4608.15
Δ_J	[3.332739]	3.33431(40)				
Δ_K	[-5.26388]	-5.26547(64)				
Δ_{JK}	[2.2837]	2.28375(81)				
δ_K	[-0.052425]	0.05191(23)				
δ_J	[0.04317]	0.042605(187)				
κ^d	0.915827	0.916094	0.9493354	0.949914	0.847550	0.849841
J_{Max}	6	54	4	9	4	12
$K_{c,max}$	3	37	2	3	2	4
# lines	19	212	10	27	6	31

5.2.4 Thiophene

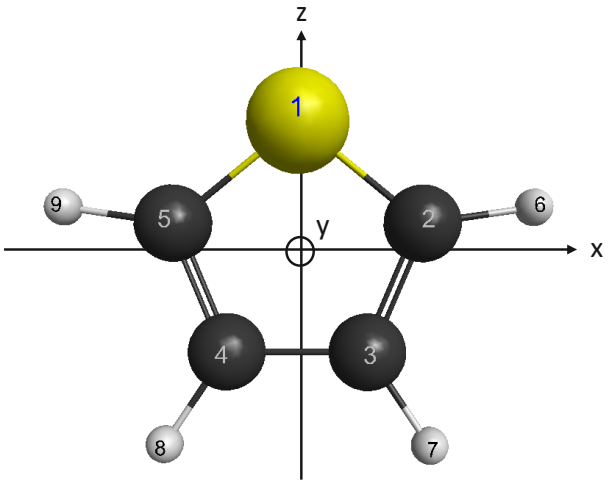

Figure 5.14. The molecular structure of thiophene.

Thiophene (C_4H_4S) is a planar five-membered heterocyclic molecule with point group C_{2v}. Figure 5.14 depicts the molecular structure. Thiophene was identified as organic matter on the red planet in the Mars Science Laboratory (MSL).[31] The first rational spectrum of thiophene was analyzed by Bak et al. in 1956.[32] A few years later, they resolved thiophene isotopomers with microwave spectroscopy and identified the structure of thiophene.[33] In 2001, Kochnikov et al. combined microwave spectroscopy, electron diffraction and calculation, and determined the rotational structure. From infrared and Raman spectroscopy, Klots et al. assigned vibrational bands of thiophene in 1994.[34] Pankoke et al. published the first high resolution data for thiophene and measured the vibrational bands at 712.1 cm^{-1}.[35] Hegelund et al. investigated thiophene with Fourier transform infrared spectroscopy and got a high resolution (0.0030 cm^{-1}) spectrum in the 600-1200 cm^{-1} region.[36] To our knowledge, our data is the first high-resolution Raman spectrum of thiophene.

When we tried to measure thiophene, we found that the signal was very low. The thiophene vapor pressure is 13.3 kPa and this value is reasonable to obtain good molecular beams with He carrier gas. However, its UV spectrum shows that the absorbance value is highest at 237 nm wavelength.[37] Our current beamline only has 200 nm and 266 nm available. This experiment motivated us to install an optical parametric amplifier (OPA), which allows to tune the wavelength. But the OPA is not yet operational and we instead managed to obtain a decent rotational Raman spectrum of thiophene with small ion signals using the 200 nm probe beam.

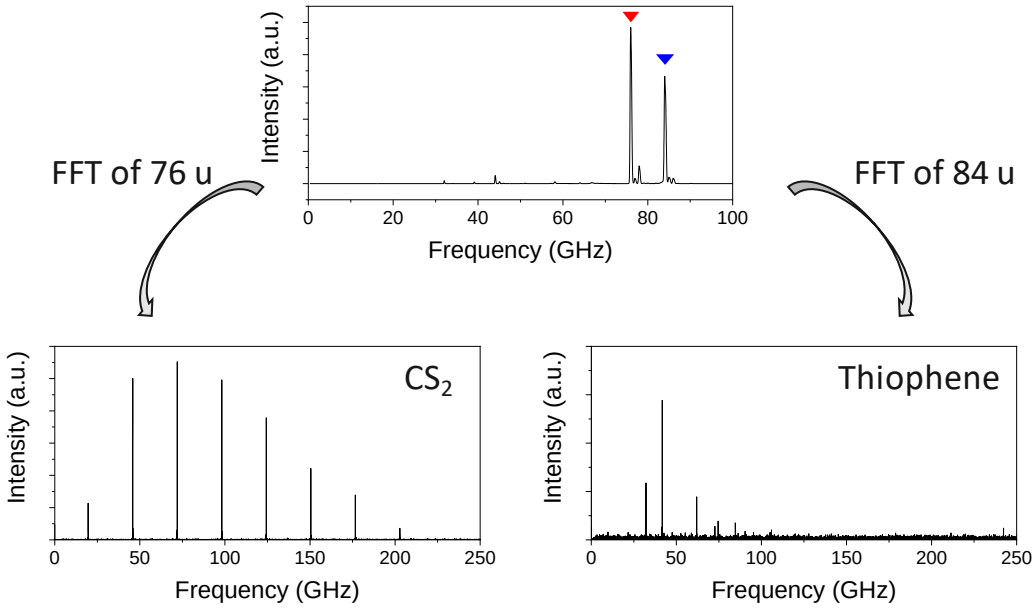

Figure 5.15. Mass spectrum and rotational Raman spectrum of thiophene (mass 84 u), obtained with a 100 ns, sparse scan with 20% sampling. Signal for residual CS_2 (mass 76 u) was also observed and gave a nice rotational spectrum.

We could only resolve 11 lines in the thiophene rotational spectrum. Our spectrum had fewer lines than the literature data from high-resolution FTIR.[36] We therefore could not properly fit molecular distortion constants and held them at literature values (see Table 5.6). The fitted constants were in reasonable agreement with literature values. The small amplitude of ion signals for thiophene in the mass spectrum (Figure 5.15, top), as compared to signals from trace amounts of CS_2, show that thiophene photoionization is very inefficient at 200 nm. A more detailed analysis of the thiophene spectrum in the future will rely on an OPA to tune the ionization beam wavelength to the absorption maximum of thiophene.

Table 5.5. Fitted rotational constants and centrifugal distortion constants (MHz) for thiophene from our measurement and literature. Fixed values are marked by square brackets.

	CRASY	*Hegelund*
A	8041.38(20)	8041.643(11)
B	5418.63(20)	5418.201(11)
C	3238.2(17)	3235.775(75)
Δ_J	[0.0021698]	0.0021698(14)
Δ_{JK}	[-0.00427]	-0.00427(7)
Δ_K	[0.0023162]	0.0023162(54)
δ_K	[-0.001405]	-0.001405(60)
δ_J	[0.0003475]	0.0003475(8)

5.2.5 Butadiene

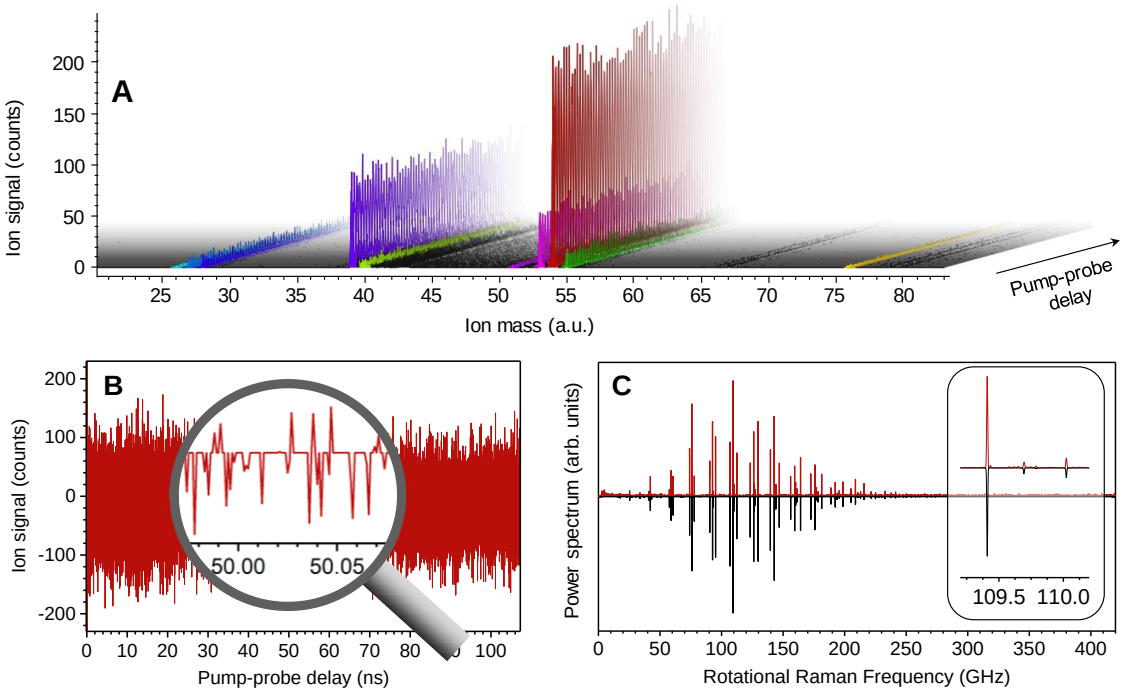

Figure 5.16. CRASY experimental data for butadiene. (A) Mass spectrum of butadiene and its fragments as a function of the pump-probe delay. The butadiene parent ion is marked red, and its cationic fragments are marked pink to blue. Green color (40 u and 55 u) marks heavy carbon (^{13}C) isotopologues. Yellow marks the signal from residual CS_2. (B) Time trace of the butadiene signal at mass 54 u. The enlarged inset shows the sparse sampling of delays. (C) The rotational spectrum of butadiene is obtained by FFT of the time trace. The black trace shows a calculated spectrum (inverted), based on our fitted rotational constants.

Butadiene (C_4H_6) is the smallest closed-shell hydrocarbon molecule with delocalized π electron system. We investigated the structure of trans-1,3-butadiene, which is the lowest energy conformer. Trans-1,3-butadiene has C_{2h} symmetry and is a near-prolate asymmetric top molecule. To describe amplitudes in the rotational spectrum, we must account for the Fermi statistics of 28:36 for ee,oe:eo,oo states. The rotational analysis is commonly performed using the I_r representation.

Butadiene was mainly analyzed by infrared and Raman spectroscopy.[38-42] In 2004, Halonen et al. measured rovibrational transitions near 3100 cm^{-1} with 50 MHz resolution by IR spectroscopy.[43] Craig et al. resolved vibrational bands of butadiene and its isotopologues with FTIR and analyzed also quartic and sextic distortion constants.[44]

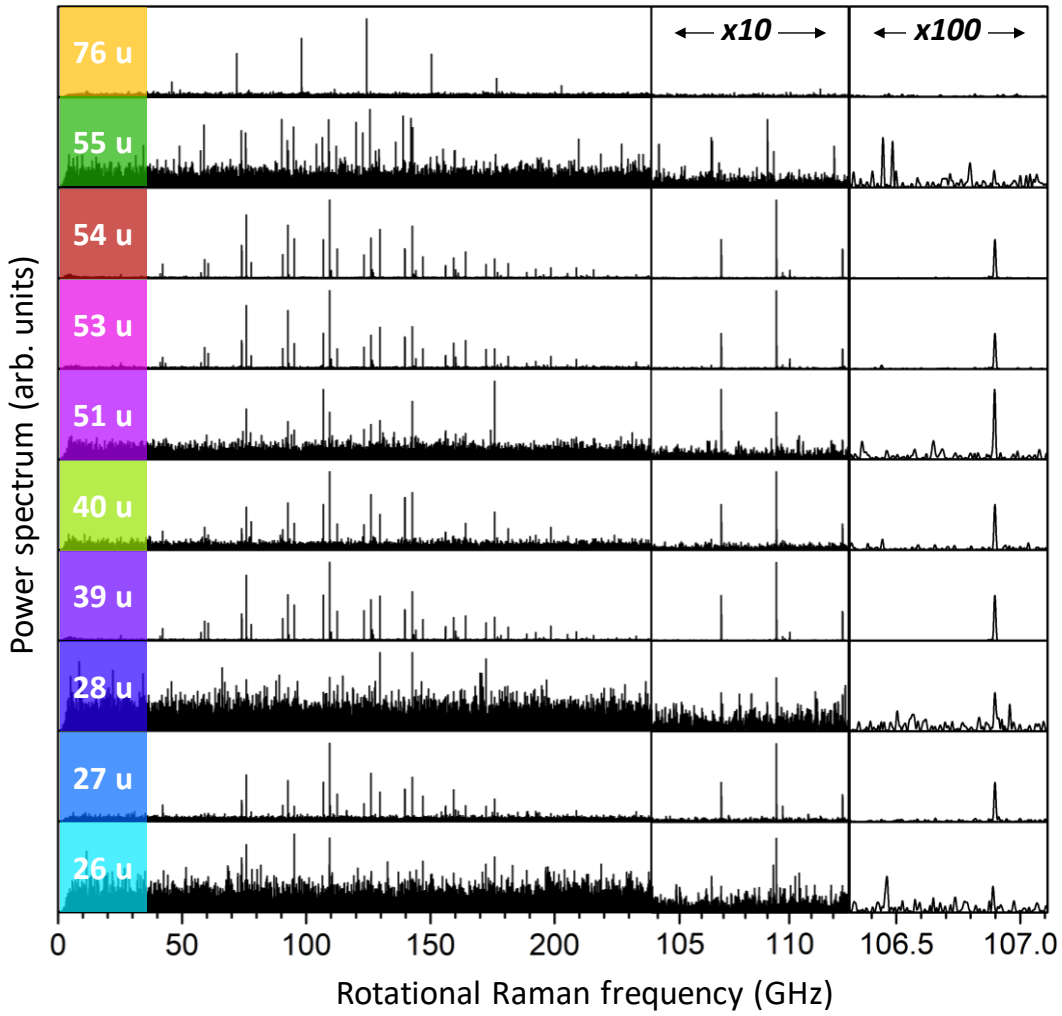

Figure 5.17. Rotational spectra obtained from a single measurement for butadiene, its isotopologues and fragments, and CS_2 in this experiment. We obtained the rotational spectrum in 7 different fragment channels of butadiene.

The Kraitchman method allows the determination of atomic positions through isotopic substitution.[45] Camininati et al. synthesized 1,1-D_2-butadiene and analyzed its rotational structure by FTMW.[46] The Craig group synthesized isotope enriched butadienes (1-^{13}C butadiene,[47] 2,3-^{13}C-butadiene,[48] 1,1-D_2-butadiene,[47] and 2,3-D_2-butadiene[44]) and studied all isomers by FTIR. Craig obtained a complete set of bond lengths and angles from isotope moments of inertia.

Butadiene is a gas at room temperature, and we prepared a sample cylinder containing 20 bars of butadiene and helium in a ratio of 1:100. The stagnation pressure was set to 10 bar. The beamlines were adjusted to deliver 100 μJ of 1 ps alignment pulses and 0.5 μJ of 200 nm, 45 fs probe pulses. The time delay between the two beams was scanned over a 107.392 ns scan range, using sparse sampling and recording a total of 28086 mass spectra. The resolution of the resulting rotational spectrum was in the

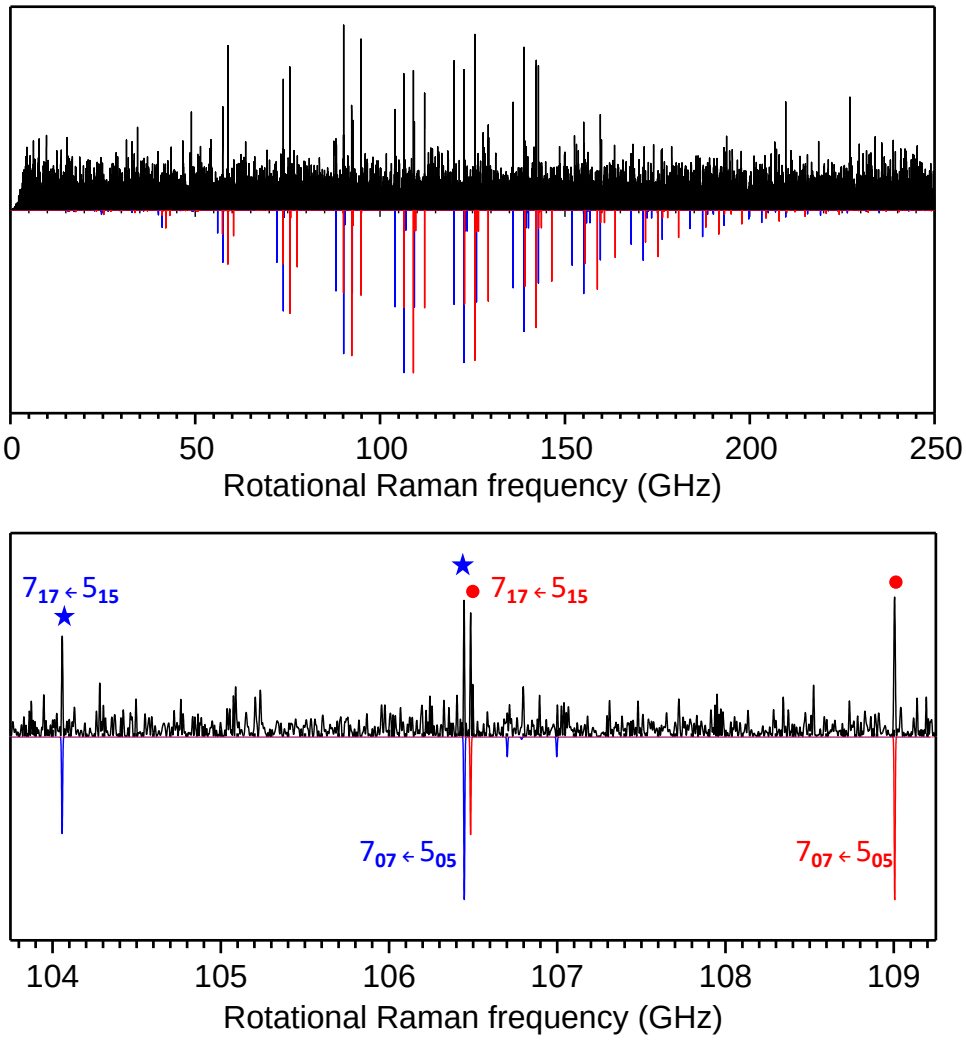

Figure 5.18. Rotational spectrum of ^{13}C-butadiene at 55 u (black) compared to fitted spectra for 1-^{13}C-butadiene (blue) and 2-^{13}C-butadiene (red). The enlarged inset shows J = 7 ← 5 transitions near 110 GHz.

range of 7.5-10 MHz.

In this experiment, we tried to resolve the rotational spectrum of butadiene and its fragments and assign the butadiene structure with the Kraitchman method.[49] Figure 5.16-c shows the comparison between the measured spectrum for the parent ion mass and a calculated spectrum. Butadiene is a near-prolate top molecule, and only transitions with $\Delta K_a = 0$ are allowed. Due to this selection rule, the uncertainties in constant A were large and distortion constants ΔK and δK could not be fit. We fixed these constants to literature values to fit the complete spectrum (see Table 5.7).

Butadiene fragments appeared at 26 u ($C_2H_2^+$), 27 u ($C_2H_3^+$), 28 u ($C_2H_4^+$), 39 u ($C_3H_3^+$), 51 u ($C_4H_3^+$), and, 53 u ($C_4H_5^+$). The parent ion and its ^{13}C isotopologues appeared at 54 u and, 55 u, and we observed

Table 5.6. Fitted rotational constants (in MHz) from our measurement and from literature for butadiene and its heavy carbon isotopomers. The centrifugal distortion constants are given in kHz. Fixed values are expressed in square brackets.

	^{12}C			1-^{13}C		2-^{13}C
	CRASY	Craig, 2006	Craig, 2008	CRASY	Craig, 2005	CRASY
A	41685(11)	41682.658(21)	41682.454(30)	41606(57)	41634.934(17)	41018(38)
B	4433.506(35)	4433.5047(30)	4433.532(15)	4306.763(84)	4307.0672(90)	4419.823(70)
C	4008.035(30)	4008.0423(60)	4008.0453(60)	3904.308(91)	3904.0502(90)	3991.283(50)
Δ_J	0.000891(44)	0.000876(12)	0.000872(12)	0.00107(25)	0.0008118(24)	0.00013(25)
Δ_K	[0.219388]	0.219388(90)	0.21846(12)	[0.2177]	0.2177(3)	[0.218]
Δ_{JK}	-0.0049(30)	-0007324(15)	-0.007195(30)	[-0.006928]	-0.006928(15)	[-0.007]
δ_K	[0.004017]	0.004017(60)	0.00444(96)	[0.0045]	0.0045(6)	[0.004]
δ_J	0.000133(57)	0.0001075(27)	0.0001145(36)	0.00083(34)	0.0000923(21)	0.00125(29)
κ^d	–0.977415	–0.977414	–0.977412	–0.978650	–0.978637	–0.977176
J_{Max}	15	66	53	9	67	9
$K_{a,max}$	3	21	17	1	23	1
# lines	61	1571	2990	12	2181	13

signal from residual CS_2 at 76 u. The Fourier transformation of time traces for each of these masses gave us their rotational Raman spectra. Figure 5.17 shows the rotational Raman spectrum for each mass channel marked in color in Fig. 5.16-a. The spectra for mass 54 u, 53 u, 51 u, 40 u, 39 u, 28 u, 27 u, and 26 u showed identical line positions. This proves that all these fragments stem from the same butadiene parent species. The signal at 55 u stems from two ^{13}C isotopologues and shows shifted band positions.

In the 55 u mass channel, we identified 12 bands for the 1-^{13}C-butadiene and 13 bands for the 2-^{13}C-butadiene isotopologues. In Figure 5.18, our measurement of 55 u is compared to a PGOPHER simulation based on our fitted rotational constants. All observed bands were well reproduced with the simulated spectrum. However, low signal intensities (this measurement was performed with a natural butadiene sample and not an isotopically enriched sample) reduced the signal-to-noise ratio and we assigned fewer lines than for the parent ion.

Table 5.7. Calculated bond lengths (Å) and bond angle (°) from a Kraitchman analysis of our isotopologue results.

	CRASY	Craig		Kveseth
	r_s	r_s	r_0	r_0
r(C-C)	1.466(7)	1.451(4)	1.458(3)	1.468
r(C=C)	1.342(14)	1.344(6)	1.346(3)	1.348
α(C=C-C)	123.1(1.4)	123.6(6)	123.4(1)	124.3

Using our heavy isotopologue spectrum, we identified the structure of the carbon backbone of butadiene with a Kraitchman analysis. In table 5.8, our substitution structure parameters r_s are compared to those reported by Craig et al.[47] based on high-resolution IR spectroscopy, and those from Kveseth et

al., based on electron diffraction data. The r_0 structure from electron-diffraction data agreed well with our r_s values, within Costain errors.[50] Compared to literature data, our structure values were reasonable, but the error bounds were a factor 2 worse than those given by Craig. This is due to the small isotopologue signals from our natural sample, which led to a decrease of the signal-to-noise ratio and restricted our ability to determine accurate bond lengths and angles.

5.3 Discussion

In this work, we measured the first CRASY spectra for asymmetric top molecules and biorelevant molecules. It was harder to perform experiments on an asymmetric top molecule, as compared to a linear or symmetric top molecule. The three different rotational constants and relaxed selection rules generate many rotational transitions and this leads to complex rotational spectra. Also, the revival peaks in the time domain are less sharp and of lower size. Fourier transformation of the time trace gave us rotational spectra, but the signal-to-noise ratio was worse than that obtained for symmetric top molecules. However, rotational constants for all asymmetric top molecules were determined, and were in good agreement with values from microwave spectroscopy, rovibrational spectroscopy, and rotational coherence spectroscopy. Our rotational resolution was worse than that of FTMW but, already exceeds that of IR and RCS experiments by a large margin. All results confirm that CRASY produces reliable rotational constants for asymmetric top molecules and our spectroscopic tool will be a complementary method to determine the structure of complex molecules.

CRASY experiments can contribute to the understanding of fragmentation mechanism for molecules and molecular dimers. The correlation of mass and rotational spectroscopy creates the unique ability to analyze the fragmentation mechanism for individual parent structures. In the case of pyridine dimer, the limited signal-to-noise ratio made it impossible to assign a rotational spectrum. Nevertheless, the investigation, combined with theory, gave us insights into an asymmetric dissociation process. A complete description of the asymmetric fragmentation of pyridine dimer will require more calculations and experiments.

Analysis of isotope spectra allows to pinpoint the position of a substituted atom in the molecular frame and thereby to calculate the structure of molecules. Compared to other experiments that require isotopically enriched samples, mass-CRASY can collect the required data without isotopically enriched samples. We demonstrated this capability with our work on butadiene, which represents the first-ever structure determination from a single rotational Raman data-set. Previous experiments relied on molecules that were synthesized with selected heavy isotope markers. In the past, only the high-resolution FTMW method was capable to resolve heavy isotopologue signals in natural samples. We can therefore claim that our spectroscopy can be a new tool for the determination of molecular structure at natural isotopic abundance.

Unfortunately, the current experimental setup has a limitation in terms of the signal-to-noise ratio. Late in 2020, a new detector increased the absolute amount of signal and we hope to resolve this problem in the near future. We also plan to correlate additional spectroscopic information (i.e. electron spectra) to investigate additional molecular properties.

5.4 Conclusion

The experiments presented in this chapter established that CRASY can measure mass-correlated rotational Raman spectra for asymmetric top molecules. All measured rotational constants are in good agreement with spectroscopic results (i.e. FTMW and FTIR data). Time delays in the range of hundreds of nanoseconds proved enough to resolve rotational transitions of asymmetric top molecules. A current limitation of our measurement is that we cannot fit accurate distortion constants for all axes due to the lack of high J-state transitions. An increase in the signal-to-noise ratio will help to resolve more lines and resolve this issue. With CRASY, it is also possible to assign spectra for multiple isotopologues and fragments based on the mass correlation, which is a novel capability, absent in FTMW and FTIR data.

The ultimate purpose of CRASY is to correlate information from multiple spectroscopies and identify molecular properties in heterogeneous sample. Our current system only correlated two types of spectroscopy, molecular mass and rotational structures. However, the data presented in this thesis already proved the power of correlation spectroscopy with combined mass, and rotational information. We easily distinguished signals from different molecules in our samples (e.g., butadiene and CS_2, or pyridine and pyridine dimer). We unambiguously assigned fragment species to their parent molecules. These are unique capabilities of CRASY that go beyond those of traditional spectroscopic techniques. The asymmetric top results presented here are the first step towards the spectroscopic analysis of DNA bases, where tautomer and rotamer structure may affect molecular properties. Future work will attempt to reveal the mechanisms protecting of DNA against photochemical damage and to observe unidentified molecular species that correspond to astrophysical molecules.

5.5 Reference

1. Schröter, C.; Choi, C. M.; Schultz, T., CRASY: Correlated Rotational Alignment Spectroscopy Reveals Atomic Scrambling in Ionic States of Butadiene. *Journal of Physical Chemistry A* **2015,** *119* (8), 1309-1314.

2. Weber, A. In *Handbook of High-resolution Spectroscopy*; Quack, M.; Merkt, F., Eds.; John Wiley & Sons, Ltd: Chichester, UK, **2011**; Vol. 2; Chapter High-resolution Raman Spectroscopy of Gases, pp. 1153.

3. Ye, E.; Bettens, R. P.; De Lucia, F. C.; Petkie, D. T.; Albert, S., Millimeter and submillimeter wave rotational spectrum of pyridine in the ground and excited vibrational states. *Journal of Molecular Spectroscopy* **2005,** *232* (1), 61-65.

4. Bak, B.; Rastrup-Andersen, J., Microwave Investigation of Pyridine. *The Journal of Chemical Physics* **1953,** *21* (7), 1305-1306.

5. McCulloh, K. E.; Pollnow, G. F., An Investigation of the Microwave Spectrum of Pyridine. *The Journal of Chemical Physics*, **1954**, *22(4)*, 681-682.

6. Bak, B.; Hansen, L.; Rastrup-Anderson, J., Microwave Spectrum of Pyridine. *The Journal of Chemical Physics,* **1954***, 22*, 565.

7. Sørensen, G. O., Centrifugal Distortion Analysis of Microwave Spectra of Asymmetric Top Molecules. The Microwave Spectrum of Pyridine. *Journal of Molecular Spectroscopy,* **1967***, 22*, 325-346.

8. Heineking, N.; Dreizler, H.; Schwarz, R.; Nitrogen and Deuterium Hyperfine Structure in the Rotational Spectra of Pyridine and 4-D Pyridine. *Zeitschrift fur Naturforschung A*, **1986**, Vol. 41, pp 1210-1213.

9. Sørensen, G. O.; Mahler, L.; Rastrup-Andersen, N., Microwave spectra of 15N and 13C pyridines, quadrupole coupling constants, dipole moment and molecular structure of pyridine. *Journal of Molecular Structure,* **1974***, 20*, 119-126.

10. Becucci, M.; Melandri, S., High-Resolution Spectroscopic Studies of Complexes Formed by Medium-Size Organic Molecules. *Chemical Reviews,* **2016***, 116*, 5014-5037.

11. Piacenza, M.; Grimme, S., Van der Waals interactions in aromatic systems: Structure and energetics of dimers and trimers of pyridine. *Chemphyschem,* **2005***, 6*, 1554-1558.

12. Hohenstein, E. G.; Sherrill, C. D., Effects of Heteroatoms on Aromatic pi-pi Interactions: Benzene-Pyridine and Pyridine Dimer. *Journal of Physical Chemistry A,* **2009***, 113*, 878-886.

13. Zhang, J.; Gao, Y.; Yao, W.; Li, S.; Tao, F.-M., Ab initio study of the pi-pi interaction in the pyridine dimer: Effects of bond functions. *Computational and Theoretical Chemistry,* **2014***, 1049*, 82- 89.

14. Sierański, T., Discovering the stacking landscape of a pyridine-pyridine system. *Journal of Molecular Modeling* **2017,** *23* (12), 338.

15. Schröter, C.; Lee, J. C.; Schultz, T., Mass-correlated rotational Raman spectra with high resolution, broad bandwidth, and absolute frequency accuracy. *Proc. Natl. Acad. Sci. USA,* **2018,** *115*, 5072-5076.

16. Neese, F. The ORCA program system. *Wiley Interdisciplinary Reviews: Computational Molecular Science*, **2012**, *2*(1), 73-78.

17. Neese, F. Software update: the ORCA program system, version 4.0. *Wiley Interdisciplinary Reviews: Computational Molecular Science*, **2018**, *8*(1), e1327.

18. Grimme, S.; Brandenburg, J. G.; Bannwarth, C.; Hansen, A., Consistent structures and interactions by density functional theory with small atomic orbital basis sets. *The Journal of Chemical Physics,* **2015**, *143*, 054107.

19. Lord, R.; Marston, A.; Miller, F. A., Infra-red and Raman spectra ot the diazines. *Spectrochimica Acta* **1957,** *9* (2), 113-125.

20. Califano, S.; Adembri, G.; Sbrana, G., Vapour and crystal spectra in polarized light of pyrazine-d0, cis pyrazine-d2 and pyrazine-d4. *Spectrochimica Acta* **1964,** *20* (3), 385-396.

21. Billes, F.; Mikosch, H.; Holly, S., A comparative study on the vibrational spectroscopy of pyridazine, pyrimidine and pyrazine. *Journal of Molecular Structure: THEOCHEM,* **1998,** *423* (3), 225-234.

22. Breda, S.; Reva, I.; Lapinski, L.; Nowak, M.; Fausto, R., Infrared spectra of pyrazine, pyrimidine and pyridazine in solid argon. *Journal of Molecular Structure* **2006,** *786* (2-3), 193-206.

23. Schmitt, M.; Biemann, L.; Meerts, W. L.; Kleinermanns, K., Analysis of the FTIR spectrum of pyrazine using evolutionary algorithms. *Journal of Molecular Spectroscopy* **2009,** *257* (1), 74-81.

24. Tsubouchi, M.; Whitaker, B. J.; Wang, L.; Kohguchi, H.; Suzuki, T., Photoelectron imaging on time-dependent molecular alignment created by a femtosecond laser pulse. *Physical Review Letters* **2001,** *86* (20), 4500.

25. Halverson, F.; Hirt, R. C. Near ultraviolet solution spectra of the diazines. *The Journal of Chemical Physics*, **1951**, *19* (6), 711-718.

26. Bak, B.; Christensen, D.; Dixon, W. B.; Hansen-Nygaard, L.; Andersen, J. R.; Schottländer, M., The complete structure of furan. *Journal of Molecular Spectroscopy* **1962,** *9*, 124-129.

27. Mata, F.; Martin, M. C.; Sørensen, G. O., Microwave spectra of deuterated furans. Revised molecular structure of furan. *Journal of Molecular Structure* **1978,** *48* (2), 157-163.

28. Wlodarczak, G.; Martinache, L.; Demaison, J.; Van Eijck, B. P., The millimeter-wave spectra of furan, pyrrole, and pyridine: Experimental and theoretical determination of the quartic centrifugal distortion constants. *Journal of Molecular Spectroscopy,* **1988***, 127*, 200-208.

29. Liescheski, P. B.; Rankin, D. W., Molecular structure of furan, determined by combined analyses of data obtained by electron diffraction, rotational spectroscopy and liquid crystal NMR spectroscopy. *Journal of Molecular Structure* **1989,** *196*, 1-19.

30. Monostori, B. J.; Weber, A., The pure rotational Raman spectra of furan and cyclopentene. *Journal of Molecular Spectroscopy* **1965,** *15* (2), 158-167.

31. Eigenbrode, J. L.; Summons, R. E.; Steele, A.; Freissinet, C.; Millan, M.; Navarro-González, R.; Sutter, B.; McAdam, A. C.; Franz, H. B.; Glavin, D. P., Organic matter preserved in 3-billion-year-old mudstones at Gale crater, Mars. *Science* **2018,** *360* (6393), 1096-1101.

32. Bak, B.; Christensen, D.; Rastrup-Andersen, J.; Tannenbaum, E., Microwave Spectra of Thiophene, 2-and 3-Monodeutero, 3, 3′-Dideutero, and Tetradeuterothiophene. Structure of the Thiophene Molecule. *The Journal of Chemical Physics* **1956,** *25* (5), 892-896.

33. Bak, B.; Christensen, D.; Hansen-Nygaard, L.; Rastrup-Andersen, J., The structure of thiophene. *Journal of Molecular Spectroscopy* **1961,** *7* (1-6), 58-63.

34. Klots, T.; Chirico, R.; Steele, W., Complete vapor phase assignment for the fundamental vibrations of furan, pyrrole and thiophene. *Spectrochimica Acta Part A: Molecular Spectroscopy* **1994,** *50* (4), 765-795.

35. Pankoke, B.; Yamada, K.; Winnewisser, G., High resolution IR-spectra of furane and thiophene. *Zeitschrift für Naturforschung A* **1993,** *48* (12), 1193-1202.

36. Hegelund, F.; Larsen, R. W.; Palmer, M., The high-resolution infrared spectrum of thiophene between 600 and 1200 cm− 1: A spectroscopic and theoretical study of the fundamental bands ν6, ν7, ν13, and the c-Coriolis interacting dyad ν5, ν19. *Journal of Molecular Spectroscopy* **2008,** *247* (1), 100-114.

37. Mehri, F.; Sauter, W.; Schröder, U.; Rowshanzamir, S. (2019). Possibilities and constraints of the electrochemical treatment of thiophene on low and high oxidation power electrodes. *Energy & Fuels*, **2019**, *33*(3), 1901-1909.

38. Marais, D.; Sheppard, N.; Stoicheff, B., An investigation of the structure of butadiene by high resolution infra-red and raman spectroscopy. *Tetrahedron* **1962,** *17* (3-4), 163-169.

39. Cole, A.; Mohay, G.; Osborne, G., Rotational fine structure of an infra-red of butadiene and the length of the central C C bond. *Spectrochimica Acta Part A: Molecular Spectroscopy* **1967,** *23* (4), 909-920.

40. Ogilvie, J.; Cole, K., Vibration-rotational bands of butadiene-1, 3: Evidence for Coriolis coupling. *Journal of Molecular Spectroscopy* **1970,** *35* (2), 332-334.

41. Hills, G.; Jones, W. J., Raman spectra of asymmetric top molecules. Part 2.—ΔK=±2 transitions in the rotational spectrum of butadiene. *Journal of the Chemical Society, Faraday Transactions 2: Molecular and Chemical Physics* **1975,** *71*, 827-834.

42. Hills, G.; Jones, W. J., Raman spectra of asymmetric top molecules. Part 3.—Intensity beats in the Raman spectra of near prolate tops. *Journal of the Chemical Society, Faraday Transactions 2: Molecular and Chemical Physics* **1975,** *71*, 835-842.

43. Halonen, M.; Halonen, L.; Nesbitt, D. J., Structural issues in conjugated hydrocarbons: High-resolution infrared slit-jet spectroscopy of trans-1, 3-butadiene. *The Journal of Physical Chemistry A* **2004,** *108* (16), 3367-3372.

44. Craig, N. C.; Davis, J. L.; Hanson, K. A.; Moore, M. C.; Weidenbaum, K. J.; Lock, M., Analysis of the rotational structure in bands in the high-resolution infrared spectra of butadiene and butadiene-2, 3-d2: refinement in assignments of fundamentals. *Journal of Molecular Structure* **2004,** *695*, 59-69.

45. Kraitchman, J., Determination of molecular structure from microwave spectroscopic data. *American Journal of Physics* **1953,** *21* (1), 17-24.

46. Caminati, W.; Grassi, G.; Bauder, A., Microwave Fourier transform spectrum of s-trans-1, 3-butadiene-1, 1-d2. *Chemical Physics Letters* **1988,** *148* (1), 13-16.

47. Craig, N. C.; Groner, P.; McKean, D. C., Equilibrium structures for butadiene and ethylene: compelling evidence for π-electron delocalization in butadiene. *The Journal of Physical Chemistry A* **2006,** *110* (23), 7461-7469.

48. Craig, N. C.; Moore, M. C.; Patchen, A. K.; Sams, R. L., Analysis of rotational structure in the high-resolution infrared spectrum and assignment of vibrational fundamentals of butadiene-2, 3-$^{13}C_2$. *Journal of Molecular Spectroscopy* **2006,** *235* (2), 181-189.

49. Özer, B. R.; Heo, I.; Lee, J. C.; Schröter, C.; Schultz, T., De novo structure determination of butadiene by isotope-resolved rotational Raman spectroscopy. *Physical Chemistry Chemical Physics* **2020,** *22* (16), 8933-8939.

50. Costain, C., Determination of molecular structures from ground state rotational constants. *The Journal of Chemical Physics* **1958,** *29* (4), 864-874.

Supporting Information

1. Line List

In this thesis, we determined rotational constants of symmetric top and asymmetric top molecules, using the PGOPHER program. The assignment of observed rotational bands was performed by comparison to calculated line positions, based on literature constants. To fit a rotational spectrum, the molecular symmetry determined the point group. The representation of molecules was followed by Watson A-reduced Hamiltonian. The rotational temperature was governed by the Boltzman distribution.

Table S1. Assigned lines for the benzene-d6 and PGOHPER fit results with 200 ns sparse scan.

Observed	Calculated	Obs.-Cal.	Upper			Lower		
(MHz)	(MHz)		J	S	#	J	S	#
18829.72	18829.2554	0.4646	2	E1g	1	1	E1g	1
28244.06	28243.8400	0.2200	3	E2g	1	2	E2g	1
37658.58	37658.3741	0.2059	4	B+g	1	3	B-g	1
	37658.3741	0.2059	4	B-g	1	3	B+g	1
	37658.3654	0.2146	4	E2g	2	3	E2g	1
47073.07	47072.8416	0.2284	5	E2g	1	4	E2g	1
	47072.8264	0.2436	5	B-g	1	4	B+g	1
	47072.8264	0.2436	5	B+g	1	4	B-g	1
	47073.0893	-0.0193	3	A+g	1	1	A+g	1
	47073.0915	-0.0215	3	E1g	1	1	E1g	1
56487.74	56487.2263	0.5137	6	E1g	1	5	E1g	1
	56487.2028	0.5372	6	E2g	1	5	E2g	1
	56487.1845	0.5555	6	B-g	1	5	B+g	1
	56487.1845	0.5555	6	B+g	1	5	B-g	1
65902.08	65902.1932	-0.1132	4	A+g	1	2	A+g	1
	65902.1962	-0.1162	4	E1g	1	2	E1g	1
	65901.4783	0.6017	7	E1g	2	6	E1g	1
	65901.5118	0.5682	7	A+g	1	6	A-g	1
	65901.5118	0.5682	7	A-g	1	6	A+g	1
75315.85	75315.6369	0.2131	8	A+g	1	7	A-g	1
	75315.6369	0.2131	8	A-g	1	7	A+g	1
	75315.6821	0.1679	8	E1g	1	7	E1g	1
	75315.5986	0.2514	8	E1g	2	7	E1g	2
	75315.5672	0.2828	8	E2g	2	7	E2g	1
84731.24	84731.1652	0.0748	5	A+g	1	3	A+g	1
	84731.1691	0.0709	5	E1g	2	3	E1g	1
	84731.1809	0.0591	5	E2g	2	3	E2g	1
94144.06	94143.5379	0.5221	10	E2g	2	9	E2g	1
	94143.6119	0.4481	10	B+g	1	9	B-g	1
	94143.6119	0.4481	10	B-g	1	9	B+g	1
	94143.4726	0.5874	10	E1g	1	9	E1g	1
	94143.4161	0.6439	10	A-g	1	9	A+g	1
	94143.4161	0.6439	10	A+g	1	9	A-g	1
103560.12	103559.9678	0.1522	6	A+g	2	4	A+g	1
	103559.9726	0.1474	6	E1g	2	4	E1g	1
	103559.9869	0.1331	6	E2g	2	4	E2g	2
	103560.0109	0.1091	6	B-g	1	4	B-g	1
	103560.0109	0.1091	6	B+g	1	4	B+g	1
	122388.5632	0.0568	7	A+g	2	5	A+g	1
	122388.5688	0.0512	7	E1g	3	5	E1g	2
	122388.5858	0.0342	7	E2g	2	5	E2g	2
	122388.6141	0.0059	7	B-g	1	5	B-g	1
	122388.6141	0.0059	7	B+g	1	5	B+g	1

141216.95	141216.9137	0.0363	8	A+g	2	6	A+g	2
	141216.9202	0.0298	8	E1g	3	6	E1g	2
	141216.9398	0.0102	8	E2g	3	6	E2g	2
	141216.9725	-0.0225	8	B+g	1	6	B+g	1
	141216.9725	-0.0225	8	B-g	1	6	B-g	1
	141217.0182	-0.0682	8	E2g	2	6	E2g	1
160044.81	160044.9818	-0.1718	9	A+g	2	7	A+g	2
	160044.9892	-0.1792	9	E1g	3	7	E1g	3
	160045.0114	-0.2014	9	E2g	3	7	E2g	2
	160045.0484	-0.2384	9	B+g	2	7	B+g	1
	160045.0484	-0.2384	9	B-g	2	7	B-g	1
	160045.1001	-0.2901	9	E2g	2	7	E2g	1
	160045.1667	-0.3567	9	E1g	2	7	E1g	2
178872.51	178872.7297	-0.2197	10	A+g	2	8	A+g	2
	178872.7379	-0.2279	10	E1g	3	8	E1g	3
	178872.7627	-0.2527	10	E2g	4	8	E2g	3
	178872.8041	-0.2941	10	B+g	2	8	B+g	1
	178872.8041	-0.2941	10	B-g	2	8	B-g	1
	178872.8619	-0.3519	10	E2g	3	8	E2g	2
	178872.9364	-0.4264	10	E1g	2	8	E1g	2
197700.17	197700.1197	0.0503	11	A+g	2	9	A+g	2
	197700.1289	0.0411	11	E1g	4	9	E1g	3
	197700.1563	0.0137	11	E2g	4	9	E2g	3
	197700.2020	-0.0320	11	B-g	2	9	B-g	2
	197700.2020	-0.0320	11	B+g	2	9	B+g	2
	197700.2659	-0.0959	11	E2g	3	9	E2g	2
	197700.3482	-0.1782	11	E1g	3	9	E1g	2
	197700.4487	-0.2787	11	A+g	1	9	A+g	1
	197700.4487	-0.2787	11	A-g	1	9	A-g	1
	197700.5675	-0.3975	11	E1g	2	9	E1g	1
216527.01	216527.2744	-0.2644	12	E2g	3	10	E2g	3
	216527.3645	-0.3545	12	E1g	3	10	E1g	2
	216527.2044	-0.1944	12	B-g	2	10	B-g	2
	216527.2044	-0.1944	12	B+g	2	10	B+g	2
	216527.1543	-0.1443	12	E2g	4	10	E2g	4
	216527.1243	-0.1143	12	E1g	4	10	E1g	3
	216527.1143	-0.1043	12	A+g	3	10	A+g	2
	216527.4746	-0.4646	12	A-g	2	10	A-g	1
	216527.4746	-0.4646	12	A+g	2	10	A+g	1
	216527.6047	-0.5947	12	E1g	2	10	E1g	1
235354.25	235354.2087	0.0413	13	E1g	3	11	E1g	2
	235354.0673	0.1827	13	A-g	2	11	A-g	1
	235354.0673	0.1827	13	A+g	2	11	A+g	1
	235353.9477	0.3023	13	E1g	4	11	E1g	3
	235354.3719	-0.1219	13	E2g	2	11	E2g	2
	235353.8498	0.4002	13	E2g	3	11	E2g	3
	235353.7736	0.4764	13	B+g	2	11	B+g	2

235353.7736	0.4764	13	B-g	2	11	B-g	2
235353.7192	0.5308	13	E2g	4	11	E2g	4
235353.6866	0.5634	13	E1g	5	11	E1g	4

Table S2. Assigned lines for the pyridine and PGOHPER fit results with 20 ns continuous scan.

Observed	Calculated	Obs.-Calc.	Upper			Lower		
(MHz)	(MHz)		J	K_a	K_c	J	K_a	K_c
23210.1	23219.6039	-9.5039	2	1	1	1	1	1
24154.6	24156.9595	-2.3595	2	2	1	1	0	1
35545.3	35546.2696	-0.9696	3	2	2	2	0	2
	35546.3097	-1.0097	2	2	0	0	0	0
47343	47350.6766	-7.6766	4	2	3	3	0	3
47455.6	47456.2783	-0.6783	4	3	2	3	1	2
58644	58643.7256	0.2744	3	2	1	1	0	1
59179.2	59189.6458	-10.4458	5	2	4	4	0	4
	59163.4315	15.7685	5	2	3	4	2	3
	59189.4873	-10.2873	5	1	4	4	1	4
	59181.3801	-2.1801	5	3	3	4	1	3
59293.9	59289.7022	4.1978	3	3	0	1	1	0
59818.3	59814.906	3.394	3	3	1	1	1	1
71022.2	71029.6911	-7.4911	6	2	5	5	0	5
	71016.4721	5.7279	6	2	4	5	2	4
	71029.6858	-7.4858	6	1	5	5	1	5
	71017.3263	4.8737	6	3	4	5	1	4
	71015.6639	6.5361	6	4	3	5	2	3
82121.9	82126.7808	-4.8808	4	3	1	2	1	1
82722.8	82728.3382	-5.5382	4	2	2	2	0	2
83101.4	83099.8346	1.5654	4	4	0	2	2	0
83766.7	83763.5565	3.1435	4	4	1	2	2	1
105642.1	105637:6088	4.4912	5	4	1	3	2	1
106522.2	106514:1081	8.0919	5	2	3	3	0	3
	106527.9405	-5.7405	5	3	3	3	1	3
106642.8	106638.2330	4.567	5	4	2	3	2	2
106999.5	106996.4894	3.0106	5	5	0	3	3	0
107737.8	107732.8355	4.9645	5	5	1	3	3	1
129191.9	129187.2860	4.614	6	5	1	4	3	1
130991.4	130988.0111	3.3889	6	6	0	4	4	0
131730.9	131725.8729	5.0271	6	6	1	4	4	1
152794.5	152789.0459	5.4541	7	6	1	5	4	1
155079	155067.0729	11.9271	7	7	0	5	5	0
179218.9	179212.3686	6.5314	8	8	0	6	6	0
179793.8	179787.1428	6.6572	8	8	1	1	1	1

Table S3. Assigned lines for the pyridine and PGOHPER fit results with 100 ns sparse scan.

Observed	Calculated	Obs.-Calc.	Upper			Lower		
(MHz)	(MHz)		J	K_a	K_c	J	K_a	K_c
23218.7	23219.96	-1.25	2	1	1	1	1	1
24157.98	24157.54	0.43	2	2	1	1	0	1
35462.52	35463.95	-1.43	3	1	2	2	1	2
35546.74	35546.98	-0.24	3	2	2	2	0	2
	35547.02	-0.28	2	2	0	0	0	0
47183.74	47182.93	0.8	4	2	2	3	2	2
47349.38	47351.61	-2.22	4	2	3	3	0	3
	47457.25	-0.54	4	3	2	3	1	2
58644.96	58644.77	0.46	3	2	1	1	0	1
59192.67	59190.81	1.85	5	2	4	4	0	4
59192.67	59190.65	2.01	5	1	4	4	1	4
59291.85	59290.90	0.94	3	3	0	1	1	0
59456.48	59457.43	-0.95	5	4	2	4	2	2
59815.12	59816.22	-1.1	3	3	1	1	1	1
71018.32	71017.06	1.25	6	4	3	5	2	3
	71017.86	0.45	6	2	4	5	2	4
	71018.72	-0.4	6	3	4	5	1	4
71031.4	71031.09	0.3	6	2	5	5	0	5
	71031.08	0.31	6	1	5	5	1	5
82128.83	82128.25	0.57	4	3	1	2	1	1
82728.21	82729.92	-1.71	4	2	2	2	0	2
82920.87	82921:21	-0.34	4	3	2	2	1	2
83101.55	83101.55	0	4	4	0	2	2	0
83764.34	83765.41	-1.07	4	4	1	2	2	1
105639.38	105639.52	-0.14	5	4	1	3	2	1
106640.84	106640.37	0.46	5	4	2	3	2	2
107735	107735.24	-0.24	5	5	1	3	3	1
129189.5	129189.65	-0.16	6	5	1	4	3	1'
130181.8	130181.65	0.1	6	4	3	4	2	3
130380.2	130379.92	0.23	6	5	2	4	3	2
130990.5	130990.86	-0.37	6	6	0	4	4	0
131728.3	131728.83	-0.53	6	6	1	4	4	1
152790.3	152791.89	-1.62	7	6	1	5	4	1
154145.3	154144.12	1.18	7	6	2	5	4	2
155070.3	155070.52	-0.18	7	7	0	5	5	0
155746.8	155747.59	-0.84	7	7	1	5	5	1
179217.2	179216.42	0.75	8	8	0	6	6	0
179791.5	179791.23	0.29	8	8	1	6	6	1
201762.6	201761.46	1.08	9	8	2	7	6	2

Table S4. Assigned lines for the pyridine and PGOHPER fit results with 500 ns sparse scan.

Observed	Calculated	Obs.-Calc.	Upper			Lower		
(MHz)	(MHz)		J	K_a	K_c	J	K_a	K_c
23219.672249	23220.140390	-0.463	2	1	1	1	1	1
24156.006611	24157.318029	-1.313	2	2	1	1	0	1
35546.654952	35546.940899	-0.286	3	2	2	2	0	2
	35546.982774	-0.329	2	2	0	0	0	0
47182.595479	47182.939891	-0.295	4	2	2	3	2	2
47351.550089	47351.564697	-0.002	4	2	3	3	0	3
59164.064502	59164.531029	-0.438	5	2	3	4	2	3
59190.328753	59190.750875	-0.402	5	2	4	4	0	4
	59190.592262	-0.243	5	1	4	4	1	4
59290.875705	59290.826671	0.037	3	3	0	1	1	0
59815.982510	59815.912885	0.067	3	3	1	1	1	1
71017.518068	71017.790182	-0.239	6	2	4	5	2	4
	71018.644990	-1.094	6	3	4	5	1	4
82128.356163	82128.501258	-0.138	4	3	1	2	1	1
83101.567468	83101.413226	0.122	4	4	0	2	2	0
83765.292466	83764.964041	0.324	4	4	1	2	2	1
105639.971560	105639.820074	0.155	5	4	1	3	2	1
106240.545489	106240.227992	0.411	5	3	2	3	1	2
106640.426557	106640.236063	0.2	5	4	2	3	2	2
106998.731629	106998.521663	0.145	5	5	0	3	3	0
107735.103697	107734.640703	0.457	5	5	1	3	3	1
129676.510457	129676.223069	0.437	6	4	2	4	2	2
130379.600009	130379.738856	-0.124	6	5	2	4	3	2
130990.619203	130990.487375	0.03	6	6	0	4	4	0
131728.022739	131728.071147	-0.053	6	6	1	4	4	1
152792.403529	152792.244134	0.139	7	6	1	5	4	1

Table S5. Assigned lines for the most dominant fragmentation (53 u) of pyrazine and PGOHPER fit results with 100 ns sparse scan.

Observed	Calculated	Obs.-Calc.	Upper			Lower		
(MHz)	(MHz)		J	K_a	K_c	J	K_a	K_c
25641.08	25641.7370	-0.6570	2	2	1	1	0	1
37036.92	37036.5348	0.3852	3	2	2	2	0	2
	37036.5730	0.3470	2	2	0	0	0	0
49248.61	49247.5842	1.0258	4	0	4	2	0	2
61520.31	61521.1138	-0.8038	5	0	5	3	0	3
62901.01	62901.6445	-0.6345	3	3	1	1	1	1
73820.67	3820.7909	-0.1209	6	0	6	4	0	4
	73820.5119	0.1581	6	1	6	4	1	4
84720.18	84719.7890	0.3910	4	3	1	2	1	1
85549.39	85547.3128	2.0772	4	2	2	2	0	2
87060.68	87059.7243	0.9557	4	4	0	2	2	0
88155.16	88154.5537	0.6063	4	4	1	2	2	1
109144.76	109144.6933	0.0667	5	4	1	3	2	1
109571.02	109570.9273	0.0927	5	3	2	3	1	2
111110.79	111109.5443	1.2457	5	4	2	3	2	2
112473.63	112472.7174	0.9126	5	5	0	3	3	0
113483.39	113483.0649	0.3251	5	5	1	3	3	1
133481.61	133482.3725	-0.7625	6	4	2	4	2	2
134879.90	134880.6134	-0.7134	6	3	3	4	1	3
135978.05	135978.8057	-0.7557	6	5	2	4	3	2
138091.98	138091.4206	0.5594	6	6	0	4	4	0
138888.75	138888.5721	0.1779	6	6	1	4	4	1
160946.77	160948.6880	-1.9180	7	6	2	5	4	2
163809.27	163809.5003	-0.2303	7	7	0	5	5	0
164364.86	164363.4838	1.3762	7	7	1	5	5	1
189542.95	189544.7013	-1.7513	8	8	0	6	6	0
189894.83	189894.6514	0.1786	8	8	1	6	6	1

Table S6. Assigned lines for the main isotopologue (80 u) of pyrazine and PGOHPER fit results with 100 ns sparse scan.

Observed	Calculated	Obs.-Calc.	Upper			Lower		
(MHz)	(MHz)		J	K_a	K_c	J	K_a	K_c
25640.82	25641.5218	0.7018	2	2	1	1	0	1
37036.24	37036.3362	-0.0962	3	2	2	2	0	2
	37036.3744	-0.1344	2	2	0	0	0	0
49249.20	49248.7039	0.4961	4	0	4	2	0	2
61519.27	61518.1743	1.0957	5	1	5	3	1	3
62902.53	62901.2120	1.3180	3	3	1	1	1	1
73821.97	73822.7049	-0.7349	6	0	6	4	0	4
	73822.4260	-0.4560	6	1	6	4	1	4
87059.75	87059.1784	0.5716	4	4	0	2	2	0
88155.38	88153.9363	1.4437	4	4	1	2	2	1
109569.81	109570.5222	-0.7122	5	3	2	3	1	2
111109.10	111108.9484	0.1516	5	4	2	3	2	2
112472.86	112471.9543	0.9057	5	5	0	3	3	0
113481.53	113482.2535	-0.7235	5	5	1	3	3	1
138091.46	138090.4278	1.0322	6	6	0	4	4	0
138887.33	138887.5582	-0.2282	6	6	1	4	4	1
189541.64	189543.2584	-1.6184	8	8	0	6	6	0

Table S7. Assigned lines for the main isotopologue of furan and PGOHPER fit results with 100 ns sparse scan.

Observed	Calculated	Obs.-Calc.	Upper			Lower		
(MHz)	(MHz)		J	K_a	K_c	J	K_a	K_c
37789.37	37789.1189	0.2511	2	2	1	1	0	1
56088.56	56089.4324	-0.8724	3	2	2	2	0	2
	56089.5522	-0.9922	2	2	0	0	0	0
74764.59	74765.0034	-0.4134	4	2	3	3	0	3
	74763.9894	0.6006	4	1	3	3	1	3
76390.29	76390.5091	-0.2191	4	4	1	3	2	1
92973.91	92975.3772	-1.4672	3	2	1	1	0	1
93502.66	93503.5285	-0.8685	3	3	0	1	1	0
93975.44	93976.0907	-0.6507	3	3	1	1	1	1
130175.32	130176.4957	-1.1757	4	3	1	2	1	1
130772.95	130771.3166	1.6334	4	2	2	2	0	2
130947.94	130948.6184	-0.6784	4	4	0	2	2	0
131576.39	131576.7674	-0.3774	4	4	1	2	2	1
168436.31	168436.1630	0.1470	5	5	0	3	3	0
169186.42	169187.1595	-0.7395	5	5	1	3	3	1
205977.07	205975.3401	1.7299	6	6	0	4	4	0
206809.23	206809.3010	-0.0710	6	6	1	4	4	1

Table S8. Assigned lines for the main isotopologue of thiophene and PGOHPER fit results with 100 ns sparse scan.

Observed (MHz)	Calculated (MHz)	Obs.-Calc.	Upper			Lower		
			J	K_a	K_c	J	K_a	K_c
21677.86	21674.4648	3.3952	2	1	1	1	1	1
32165.30	32165.4782	-0.1782	2	2	1	1	0	1
41727.84	41727.4623	0.3777	2	2	0	0	0	0
	41727.4085	0.4315	3	2	2	2	0	2
61953.92	61955.2563	-1.3363	3	2	1	1	0	1
72644.92	72643.1049	1.8151	3	3	0	1	1	0
74566.78	74563.2129	3.5671	3	3	1	1	1	1
84670.16	84670.4134	-0.2534	4	2	2	2	0	2
90405.40	90406.6887	-1.2887	4	3	1	2	1	1
105045.96	105043.6678	2.2922	4	4	0	2	2	0
105882.53	105887.4359	-4.9059	4	4	1	2	2	1

Table S1 Assigned lines for the main isotopologue of butadiene and PGOHPER fit results with 100 ns sparse scan.

Observed	Calculated	Obs.-Calc.	Upper			Lower		
(MHz)	(MHz)		J	K_a	K_c	J	K_a	K_c
33746.81	33745.16	1.65	4	2	3	3	2	1
41142.29	41141.76	0.53	3	1	3	1	1	1
42189.24	42189.47	-0.23	3	0	3	1	0	1
42329.82	42326.12	3.7	5	2	3	4	2	3
43270.28	43268.98	1.3	3	1	2	1	1	0
57592.63	57592.05	0.58	4	1	4	2	1	2
59039.76	59039.76	0	4	0	4	2	0	2
60569.69	60570	-0.31	4	1	3	2	1	1
74035.81	74036.01	-0.2	5	1	5	3	1	3
75864.8	75864.6	0.2	5	0	5	3	0	3
75966.13	75962.69	3.44	5	2	4	3	2	2
76071.22	76071.29	-0.07	5	2	3	3	2	1
77863.82	77864.38	-0.56	5	1	4	3	1	2
90471.89	90471.94	-0.05	6	1	6	4	1	4
92656.59	92656.85	-0.26	6	0	6	4	0	4
92832.28	92831.83	0.45	6	2	5	4	2	3
93030.53	93030.72	-0.19	6	2	4	4	2	2
95150.08	95150.1	-0.02	6	1	5	4	1	3
106898.27	106898.24	0.03	7	1	7	5	1	5
109409.15	109409.52	-0.37	7	0	7	5	0	5
109694.76	109694.1	0.66	7	2	6	5	2	4
109788.47	109787.51	0.96	7	3	4	5	3	2
	109791.01	-2.54	7	3	5	5	3	3
110022.73	110022.62	0.11	7	2	5	5	2	3
112424.66	112425.05	-0.39	7	1	6	5	1	4
123313.66	123313.39	0.27	8	1	8	6	1	6
126115.78	126115.96	-0.18	8	0	8	6	0	6
126547.2	126548.27	-1.07	8	2	7	6	2	5
127051.79	127052.34	-0.55	8	2	6	6	2	4
129687.1	129687.03	0.07	8	1	7	6	1	5
139715.58	139716.02	-0.44	9	1	9	7	1	7
142769.53	142769.97	-0.44	9	0	9	7	0	7
143392.98	143393.08	-0.1	9	2	8	7	2	6
144125.04	144124.79	0.25	9	2	7	7	2	5
146933.92	146933.69	0.23	9	1	8	7	1	6
156104.56	156104.87	-0.31	10	1	10	8	1	8
159365.95	159366.09	-0.14	10	0	10	8	0	8
160226.85	160227.31	-0.46	10	2	9	8	2	7
161245.9	161244.13	1.77	10	2	8	8	2	6
164162.44	164162.56	-0.12	10	1	9	8	1	7
172478.16	172478.83	-0.67	11	1	11	9	1	9

175899.39	175899.81	-0.42	11	0	11	9	0	9
177049.63	177049.75	-0.12	11	2	10	9	2	8
178413.94	178413.57	0.37	11	2	9	9	2	7
181370.68	181370.96	-0.28	11	1	10	9	1	8
188837.91	188836.95	0.97	12	1	12	10	1	10
192366.89	192367.84	-0.95	12	0	12	10	0	10
193859.72	193859.19	0.53	12	2	11	10	2	9
195633.32	195635.06	-1.74	12	2	10	10	2	8
198555.26	198556.07	-0.81	12	1	11	10	1	9
205179.24	205178.44	0.8	13	1	13	11	1	11
208767.58	208768.41	-0.83	13	0	13	11	0	11
212908.63	212909.08	-0.45	13	2	11	11	2	9
215716.85	215714.84	2.01	13	1	12	11	1	10
221502.34	221502.71	-0.37	14	1	14	12	1	12
225101.63	225101.4	0.23	14	0	14	12	0	12
232844	232843.99	0.01	14	1	13	12	1	11
241369.1	241368.49	0.61	15	0	15	13	0	13

Acknowledgment

I appreciate the support and guidance of my advisor, Prof. Dr. Thomas Schultz. Thanks to his guidance, I was able to grow into an independent researcher. I learned much scientific knowledge and attitude of the scientist from him. I want to take after his positive attitude. I want to thank all committee members, Prof. Dr. Yung Sam Kim, Prof. Dr. Oh Hoon Kwon, Prof. Dr. Bum Suk Zhao, and Dr. Chang Min Choi for participating in my defense and advising my doctoral thesis.

I want to thank our group members, In Heo and Begum Rukiye Özer. I enjoy working together in graduate school. I sincerely support their remaining degree programs. I especially thank a former member, Dr. Christian Schröter. He teaches me how to perform experiments logically. It is impossible to do CRASY experiments without his knowledge. I also want to thank other former members Kyeong Hyeon Nam, and Dong Eun Lee. I want to thank Lee Young Kim. I enjoy discussing the scientific issue with her, and without her support, it is hard to finish my thesis.

I want to thank my parents. If it weren't for my parents' dedicated support, I wouldn't have finished this process. I want to take this opportunity to say that I genuinely respect and love them. Lastly, I have received great help from many people during the combined MS-Ph.D. program. I sincerely thank everyone who supports my research. I can’t rest on my laurels and live as a sincere researcher.